Experimental and Economic Assessment of Temperature Swing Adsorption Systems for the purpose of Claus Tail Gas Clean Up

A THESIS SUBMITTED TO THE FACULTY

OF THE UNIVERSITY OF MINNESOTA

BY

Yasser F. Al Wahedi

In partial fulfillment of the requirements

for the degree of

Doctoral of Philosophy

Under the supervision of: Prof. Michael Tsapatsis

January 2015

ACKNOWLEDGMENT

Many people have contributed to my growth during my wonderful research life in the University of Minnesota. Among them, I would like to express my deepest appreciation firstly to my advisor professor Michael Tsapatsis who had the patience and the wisdom to guide me through this journey. I would like also to express my sincere gratitude to professor Prodromos Daoutidis who provided the fatherly advice and guidance which were instrumental in my success. I would like to sincerely thank Dr. Ana Torres for her continuous advice and help in the optimization and to my dear friend Dr. Dimitrios Giorgies for dedicating his valuable time in teaching me. I will never forgot the help and support I got from my dear friend Dr. V. V. Balu in guiding me through the experimental work, and to soon to be Dr. Abdulla Malek for his limitless help. In the petroleum Institute, I would like to also express my appreciation to Mr. Samuel Stephan for his continuous help, to Mrs. Anjana Thralekshmi for her help in the characterization side, to Dr. Saeed Alhassan for his valuable advice and encouragement and finally and most importantly to my dear friend Dr. Marios Katsiotis who had in him the patience and passion in teaching me practical electron microscopy. I would like to also thank my mentor in life Dr. Saleh Al Hashimi. Finally, I would like to thank my wife Arwa Ali Aidarous Al Wahedi who expressed the relentless patience during my PhD journey, to my daughters the spice of my life, and most importantly to my father and mother for their dedicated efforts and patience during the course of my life.

TABLE OF CONTENTS

LIST OF TABLES

LIST OF FIGURES

LIST OF ABBREVIATIONS & SYMBOLS

Δ_{max}	Maximum allowable pressure drop (Pa)
Δt	Temporal grid spacing in the finite differences method
ΔT_{LM}	Log mean temperature difference between the cooling fluid and the feed gas
Δx	Spatial grid spacing in finite differences method
ε_b	Bulk phase porosity
ε_p	Binder phase porosity
ζ_{ads}	Efficiency factor accounting for mass transfer effects during adsorption
ζ_{reg}	Efficiency factor accounting for mass transfer effects during regeneration
η	Adiabatic efficiency of the blower
η_i	Fitting parameter taking care of similar molecule interaction
μ	Feed gas viscosity (Pa·s)
ρ_c	Solid density of the sorbent ($kg \cdot m^{-3}$)
ρ_{cat}	Hydrogenation catalyst density ($kg \cdot m^{-3}$)
ρ_f	Density of the bulk phase ($kg \cdot m^{-3}$)
ρ_P	Density of the binder phase
ρ_S	Density of the sorbent crystallite without the binder
ρ_v	Steel density ($kg \cdot m^{-3}$)
τ	Binder tortosity
$a_{b/P}$	Surface area of the bulk-binder interface per unit volume
A_c	Area of water cooled heat exchange (m^2)
a_k	The preceding coefficient of the chosen function in equation 3.32
ALMO EDA	Absolutely Localized Molecular Orbital Energy Decomposition Analysis
a_o	Specific surface area used in equation 5.1
$a_{P/S}$	Interfacial surface area per volume of the binder-sorbent interface

B	Conversion factor used in electrical power of blower
b	Stoichiometric coefficient used in equation 5.1
BED	Net present worth of bed replacement costs
b_i	Equilibrium constant on pressure basis
Bi_i	Species i Biot number defined in equation 3.38 e
BTEX	Benzene, Toluene, Ethylbenzene, and Xylenes
C_b	Constant pressure heat capacity of the bulk phase
CBA	Cold Bed Adsorption
C_c	Heat capacity temperature function of the sorbent in ($J \cdot kg^{-1} \cdot {}^oC^{-1}$)
CD	Complete discretization
CEPCI	Chemical engineering plant cost index
$C_{F,P}$	Heat capacity function for the feed gas ($J \cdot mol^{-1} \cdot K^{-1}$)
C_i	Species i concentration in the bulk phase
$C_{i,ini}$	Initial concentration of species i within the bed's bulk phase
$C_{i,ini}^P$	Initial concentration of species i within the pellet
$C_{i,o}$	Feed concentration of species i
C_i^F	molar concentration of species i in feed gas ($mole \cdot m^{-3}$)
C_i^P	Concentration of species i within the binder phase
$\overline{C}_i^P$	Average concentration of the species i within the binder phase,
COVPs	Complementary Occupied-Virtual Orbitals Pairs
C_P	Heat capacity of the binder phase
$C_{p,v}$	Heat capacity of the vessel
$C_{regG,P}$	Constant pressure heat capacity of the regeneration gas ($J \cdot K^{-1} \cdot mol^{-1}$)
$C_{regG,V}$	Constant volume heat capacity of the regeneration gas ($J \cdot K^{-1} \cdot mol^{-1}$)
C_S	Heat capacity of the sorbent
CSS	Cyclic steady state
C_v	Heat capacity temperature function of the vessel in ($J \cdot kg^{-1} \cdot {}^oC^{-1}$)

D	Bed Diameter (m)
DIPA	Diisopropanolamine
$D_{k,i}$	Knudsen diffusion coefficient in cm^2/s
$D_{m,i}$	Bulk phase molecular diffusion coefficient for species i
$D_{P,i}$	Macroporous diffusion coefficient of species i
DS	the dusty gas model
$D_{S,i}$	Micropore diffusion coefficient of species i
$D_{z,i}$	Dispersion coefficient of species i
EDS	Electron Dispersion Spectroscopy
EELS	Electron Energy Loss Spectroscopy
ELSE	Extremely Low Sulfur Emission
f	Forcing function usually nonlinear in equation 3.30
F	Molar flow of feed gas in each vessel ($kmole \cdot h^{-1}$)
FE-SEM	Field Emission-Scanning Electron Microscopy imaging
F_k	A chosen function used in equation 3.31
F_o	Initial boundary condition in equation 3.31
H_1	Parameter in Rosen's model defined by equations 3.26
H_1*	Parameter in Rosen's model defined by equations 3.26
H_2	Parameter in Rosen's model defined by equations 3.26
H_2*	Parameter in Rosen's model defined by equations 3.26
$H_{ads,i}$	Heat of adsorption of species i ($J \cdot mole^{-1}$)
$H_{ads,i}$	Species i adsorption enthalpy
h_b	Coefficient describing heat transfer across the bulk-binder interface
HDR	Heating duty of the regeneration gas fired heater (W)
H_i	Henry's constant
h_P	Heat transfer coefficient describing heat exchange across binder-sorbent interface

HR-TEM	High Resolution-Transmission Electron Microscopy
IAS	Ideal adsorption solution theory
$k_{H,P}$	Thermal conductivity of the binder
$k_{H,S}$	Thermal conductivity of the sorbent
K_i	Equilibrium constant towards species i
$K_{i,ads}$	Adsorption equilibrium constant for species i in ($m^3 \cdot mole^{-1}$)
$K_{i,reg}$	Adsorption equilibrium constant for species i ($m^3 \cdot mole^{-1}$)
$k_{m,b}$	Mass transfer constant describing the mass transfer rates across the bulk-binder interface
L	Bed Length (m)
L	Bed length
L	Differential operator acting on a set of dependent variables (y), a set of independent variables (x), and a set of constants (c) in equation 3.30
LDF	Linear driving force model
LDF1	LDF assuming negligible accumulation within the intraparticle
LDF2	LDF assuming instantaneous equilibrium between the gas phases residing within interparticle and intraparticle
LDF3	Linear driving force dusty gas model
LF	Langmuir-Freundlich
L_{hyd}	Hydrogenation reactor bed length (m)
L_{int}	Allocated length for bed internals (m)
M	Species molecular weight
MDEA	Methyl diethanol amine
MEC	Major equipment cost
MFC	Mass Flow Controllers
m_o	Initial weight of the adsorbent used in equation 5.1
MO	Metal oxide used in equation 5.1
MOST	Mobil Oil SO_x Treatment

MOST	Mobil Oil SO_x Treatment
MS	Metal sulfide used in equation 5.1
m_v	Mass of each vessel in (kg)
MW	Molecular weight of the adsorbent in oxide form or sulfide form used in equation 5.1
N	Number of Vessels an integer variable
N1	Molar flow of regeneration gas ($kmol \cdot h^{-1}$)
n_i	Fitting parameter takes care of surface heterogeneity
NPW	Net present worth of all costs ensued by the plant during its 30 years life time
NPWC	Summation of MEC, OPEX, and BED
OC	Orthogonal Collocation
OCFE	Orthogonal collocation over finite elements methods
OPEX	Net present worth of operating costs
P_2	Outlet pressure of the regeneration gas (Pa)
P_{ads}	Current price of the sorbent in ($\$ \cdot kg^{-1}$)
P_{bed}	total cost of all sorbent beds ($)
P_{CB}	Cost of the centrifugal blower ($)
PDE	Partial Differential Equation
PDE	Partial differential equation model
P_{envi}	Inlet pressure of the regeneration gas (Pa)
P_{EP}	Electrical power cost in ($\$ \cdot kWh^{-1}$)
P_{FH}	Current cost of the fired gas heaters ($)
Pr	Prandtle number
PSA	Pressure swing adsorption
P_v	Total current cost of all vessels ($)
P_W	Electrical power cost in ($\$ \cdot yr^{-1}$)

Q_{cool}	Volumetric flow rate of cooling water ($m^3 \cdot h^{-1}$) required to achieve the targeted temperature of the feed gas T_{outg}
Q_F	Feed gas volumetric flow rate ($m^3 \cdot s^{-1}$)
q_i	Adsorbed phase concentration
$\overline{q}_i$	Average concentration of the adsorbed species within the sorbent phase
q_i*	Equilibrium adsorbed state concentration of species i
$q_{i,ini}$	Initial adsorbate concentration
q_i^{sat}	Saturation capacity of the adsorbent towards species i
Q_{reg}	Volumetric flow rate of regeneration gas in ($m^3 \cdot s^{-1}$)
q_{si}	Saturation capacity of species i ($mole \cdot kg^{-1}$)
q_{si}	Saturation capacity of species i ($mole \cdot kg^{-1}$)
q_{si}	Saturation capacity
R	The residue function in the finite elements method
r	Radial spatial dimension within the sorbent crystallite assuming spherical sorbents
R	Radial spatial dimension within the binder phase assuming spherical pellets
Re	Bulk phase Reynolds number
Re_p	Particle based Reynolds number
R_p	Adsorbent pellet radius (m)
r_{pore}	Pore radius measured in cm
r_s	Radius of the sorbent particle
r-SQP	reduced space Successive Quadratic Programming
Sc	Schmidt number for limiting species
SC	Sulfur Conversion
SCD	Sulfur Chemiluminescence Detector
Sc_i	Schmidt number of species i
SCOT	Shell Claus Off Tail gas
SD	Single dimension discretization

SQP	Sequential Quadratic Programming
SRU	Sulfur Recovery Unit
St_i	Species i Stanton number defined in equation 3.38 d
SV	Space velocity (h^{-1})
t	Time
T	Temperature within the bulk phase
T_2	Outlet temperature from the centrifugal blower
t_{ads}	Adsorption cycle time (h)
$t_{ads,max}$	Maximum allowed time for the adsorption step (h)
$t_{br,i}$	Breakthrough time species i
TCI	Total capital investment
T_{envi}	Centrifugal blower regeneration gas inlet temperature (K)
TGTU	Tail Gas Treatment Unit
th	Vessel thickness (m)
T_{hyd}	Hydrogenation reactor temperature (^oC)
T_{ini}	Initial temperature of the bed's bulk phase
T_{ini}^P	Initial pellet temperature
T_{ini}^S	Initial temperature within the crystals
T_o	Temperature of feed
T_{outg}	Outlet temperature of effluent gas from water cooled heat exchanger (^oC)
T^P	Temperature within the binder phase
t_{reg}	Allocated time for regeneration (h)
$T_{reg,G}$	Regeneration gas temperature (^oC)
$t_{reg,min}$	Minimum required regeneration time (h)
$T_{reg,out}$	Outlet temperature of the regeneration gas during the cooling step and the heating step (^oC)
T_{regG}	Temperature of regeneration gas (^oC)

$\overline{T}^S$	Average temperature within the sorbent phase
T_s	Temperature of the vessel
TSA	Temperature Swing Adsorption
U	Overall heat transfer coefficient
u	Interstitial velocity of bulk phase
u_c	Velocity of the concentration front
U_f	Feed gas superficial velocity ($m \cdot s^{-1}$)
u_o	The entrance fluid velocity in Kaczmarski algorithm
U_{reg}	Regeneration gas velocity ($m \cdot s^{-1}$)
VPIE	Vapor phase ion exchange method
W	Weighing function in finite element method
W	Weight of the adsorbent used in equation 5.1
X_1	Fitting parameter in expression 4.26
X_2	Fitting parameter in expression 4.26
X_3	Fitting parameter in expression 4.26
X_4	Fitting parameter in expression 4.26
X_5	Fitting parameter in expression 4.26
X_6	Fitting parameter in expression 4.26
XRD	X-ray Diffraction
y_i	Mole fraction of species i in the feed gas
z	Axial dimension for bulk phase
z_B	Length at which the boundary condition holds

CHAPTER 1: INTRODUCTION

1.1 MOTIVATION

The growth of world gas demand coupled with dwindling reserves of sweet easy-to-access gas have forced many nations to tap into natural gas reservoirs rich in acid gases (H_2S and CO_2) [1]. Direct combustion of raw reservoir effluents causes the release of significant quantities of SO_x species, a major cause of acid rain, material corrosion and respiratory health problems [2-4]. Thus, removal of acid gases from raw natural gas is necessitated by environmental considerations and sales gas specifications. This is conventionally achieved via selective capture through membrane, solvent or adsorption based technologies, followed by sulfur recovery [5]. The conventional method of sulfur recovery is the Claus process, which can achieve a Sulfur Conversion (SC) up to 98%. In 2001, the European Union commission established the legislative limits of SO_x emissions for gaseous fuels at 35 $mg \cdot Nm^{-3}$ [6]. When reflected at Sulfur Recovery Units (SRUs), this policy enforced recoveries in excess of 99.9% [7]. This recovery is commercially attained via addition of a Tail Gas Treatment Unit (TGTU), which supplements the conventional Claus process [5].

TGTU technologies capable of achieving the targeted sulfur conversions can be classified in regenerative solvent based technologies, non-regenerative solvent based technologies and adsorption based technologies [5, 8].

Regenerative based technologies rely on the use of a selective solvent capable of preferential absorption of sulfur species from the Claus tail-gas stream. The Lo-Cat II™ process, licensed by Merichem©, utilizes iron chelated complex in solution, which

dissolves and oxidizes the H_2S directly to sulfur. The precipitation of the sulfur during the reaction shifts the equilibrium favorably to higher conversions. During that process, the iron in the active ingredient is reduced from the +3 state to the +2 state. Regeneration of the iron complex is performed via oxidation with air. [5]. In the SCOT™ and the Clintox™ processes, licensed by Shell© and Linde© respectively, the solvent is regenerated at higher temperatures to release a concentrated stream of sulfur contaminants. The stream is then recycled back to the entrance of the SRU. Non-regenerative based processes rely on the selective capture of sulfur species from Claus tail gas into an inexpensive aqueous solvent, which chemically binds to the contaminants, thus forming sulfur based metallic salts dissolved into an aqueous solution. The solution is subsequently discarded. An example commercial realization of non-regenerative based processes is the DynaWave™ technology licensed by MERCS© [7].

Economic studies on commercially implemented TGTU technologies are limited. The Gas Technology Institute published a report, which studied the operating and capital costs of 14 TGTU options including SCOT, Clintox, and Lo-CAT II for low capacity SRUs (< 100 long ton·day^{-1}) [9]. Among the TGTU technologies that achieve 99.9% recovery, the operating and capital costs contribution of the TGTU to total SRU amounts to 50% approximately for an SRU processing 76 long ton·day^{-1}. Another study assessed the capital and operating cost implications of the SCOT and the Dynawave technologies for a 140 metric ton·day^{-1} plant [7]. The capital cost contribution of both technologies to total SRU was found to range from 29% to 45% dedicated only for increasing the SC from 98% (Conventional Claus) to 99.9% [7]. Furthermore, both technologies add an additional ~20$ per ton of processed sulfur to the operating cost of the SRU [7]. These studies show that

implementing the mentioned TGTU technologies in order to increase SC by 1.9% (from 98% to 99.9%) is 25 to 50 times more expensive on a cost per percent recovery basis. Clearly, this provides an opportunity for alternative technologies.

Adsorption based processes are known to be better suited for the removal of low concentration contaminants [10]. Two process technologies relying on adsorption capable of achieving the SC target are described in open literature [5, 11, 12]. The Extremely Low Sulfur Emission (ELSE) process developed by AMOCO relies on the use of ZnO for the selective capture of H_2S from the tail gas at temperatures in excess of 650^oC [5]. Subsequent regeneration of the sorbent is done via oxidation using a diluted stream of air. In the Mobil Off-gas Sulfur Treatment process (MOST) sulfur species are first oxidized to SO_2. Then, SO_2 is adsorbed on a proprietary sorbent (V-Ce-$Mg_2Al_2O_5$) at temperatures above 700^oC [12]. Regeneration is achieved via a reducing gas (e.g. H_2). In both processes, the regeneration gas effluent is recycled back to the Claus unit. To our knowledge, none of the aforementioned processes achieved commercial status yet, probably due to the high operating temperatures (requiring prohibitively expensive materials of construction) and limited regenerability.

The challenge in developing a successful adsorption based process lies in the development of a regenerable sorbent capable of selective removal of sulfur species among a swarm of competing contaminants (for instance, H_2O, CO_2, CO, and H_2) at temperatures sufficiently low to allow for the use of carbon steel.

Several novel materials have been investigated for low temperature removal of H_2S in the past decade. Multi-walled carbon nanotubes grafted with amine functions were found to

achieve H_2S adsorption saturation capacities in the range of 1.6 to 1.8 mmol·g^{-1} at 20^{o}C and atmospheric pressure [13]. Crespo et al. studied copper exchanged Faujasite (Cu(I)-Y) prepared via a vapor phase exchange method and compared it to solution exchanged (Cu(II)-Y) [14]. At room temperature, Cu(I)-Y adsorbent has exhibited higher stable saturation capacities in the order of 7 mmol·g^{-1}. Kumar et al. studied several metal exchanged Faujasite structures including Ag, Cu, Ni, and Na obtaining saturation capacities in the following order AgY>CuX>NiX>>NaX [15]. At 100^{o}C the highest capacities attained for CuX and AgY were 1.2 and 2.1 mmol·g^{-1} respectively. Higher capacities were reported for mixed metal oxides in coal gas desulfurization ranging between 2 to 8 mmol·g^{-1} within a temperature range of 200 to 600^{o}C [16-19]. For H_2S removal from Claus Tail gas, Elyassi and co-workers reported an SBA-15 supported Copper-Zinc mixed oxide sorbent with a stable regenerable capacity of ~ 2 mmol·g^{-1} at 150^{o}C [20] While mixed metal oxides exhibit the highest capacities among all H_2S sorbents, their high prices and regeneration requirement limits their applicability. Among the sorbents studied in the literature, copper exchanged zeolite Y prepared via the vapor phase exchange method combines the benefits of good adsorption properties and low price [14, 15]**.** Assessment of those adsorbents in real industrial case is hence desired.

1.2 THESIS OBJECTIVES & APPROACH

Considering the plethora of the newly emerging materials which possess selective adsorption affinity towards H_2S, it is arguable that an adsorption based process holds the most potential. In that context, the premise of this thesis is to develop the computational tools that provide an optimized industrially applicable adsorption system and implement

those on a real industrial case using experimentally determined properties of a selected adsorbent. The objectives pursued are as follows:

1) To propose a process concept of an adsorption based system that utilizes resources available within the sulfur recovery unit.
2) To screen reported adsorbents and arrive at a short list of the most promising ones.
3) To generate the necessary kinetic and thermodynamic properties of a selected adsorbent in case such properties are not reported.
4) To provide an efficient algorithm for the fast design and optimization of adsorbent-based technologies.
5) To implement the developed framework on the selected adsorbent given an industrial feed as to arrive at an economical assessment of the technology.

Since the available pressure in a Claus unit is low (1-2 bar), application of pressure swing processes is not feasible. Hence, the thesis scope is limited to Temperature Swing Adsorption (TSA) systems.

The proposed optimization algorithm herein is novel in the way it bypasses the complex nature of the adsorption problem. The complexity of optimizing adsorption systems stems from the necessary coupling between simultaneous solution of sets of Partial Differential Equations (PDEs) and the optimization algorithm [21]. In reported literature, this problem was attempted through three different approaches: the black box approach, the equation-oriented approach and the simultaneous tailoring approach [22]. In the black box approach, a series of simulations are conducted spanning the space of the decision variables. The results of the simulations are then regressed into an analytical model which is then used by

the optimization algorithm as the basis model. The results of the optimizer are then fed back to the simulation model where the constraints are revaluated. If all the constraints are met, then the solution is declared optimal. if not, then the result of the simulations are incorporated into the data basis of the regressed analytical model thus enhancing its accuracy in the vicinity of the previously identified optimal solution. The analytical model is used again in the optimization algorithm. The cycle continues until an optimal solution is arrived at which meet all the specified constraints. This approach is termed the black box approach since the optimization engine treats the PDE solver as a black box.

Considering the number of simulations that are required to be performed while achieving cyclic steady state condition (the latter being the most computationally demanding) in order to arrive at a predictive analytical model, the computational expense of this approach renders it applicable only to small-scale optimization problems [22].

The second approach utilizes discretization techniques such as finite differences, or orthogonal collocations to reduce the PDEs into sets of algebraic equations or differential equations, which are compiled with the rest of the elements of the optimization problem and are solved simultaneously [23-27]. Moreover, the boundary conditions are incorporated as constraints within the optimization program. This approach allows considering an expanded space of decision variables. Still, the computational expense is also high. For instance, Sankararao et al. considered a multi-objective functions optimization of a Pressure Swing Adsorption (PSA) system and reported a computational time of 720 hrs using a Pentium 4 2.99 GHz CPU [28]. Furthermore**,** the approach is limited to reduced complexity kinetic models due to the numerical instabilities that arise from modeling steep front profiles [22].

The simultaneous tailoring approach attempts a middle ground methodology. The achievement of the cyclic steady state condition is incorporated as constraint within the optimization engine while in similar fashion to the black box approach the bed simulations are performed separately [22]. This approach allows higher complexity bed models to be employed. However, the computational expense of this approach is also high.

For illustration, a single objective function optimization of a PSA system considering 7 decision variables took 122 hours on a 2.4 GHz CPU machine for complete convergence [22]. Regardless of the approach employed, the computational expense of conducting optimization and simulation of adsorption systems seems to be a major hurdle in considering comprehensive optimization problems. Furthermore, the problem can be exacerbated by the nature of the objective function. Objective functions tackled in the literature include product recovery maximization [28], power consumption minimization [26], and cost minimization [29]. To the best of the author's knowledge none of the literature studies have considered the Net Present Worth of all costs ensued (NPW) as the objective function. This could be due to the fact that the NPW function is highly nonlinear and may contain discontinuities.

The algorithm proposed herein decouples them by employing a hierarchical approach, based on firstly recasting the full scale PDE model into an analytical non-linear form that tackles the optimization problem at a simplified level of model complexity. Unlike the black box approach were the choice of the model structure is arbitrary, herein we utilize the analytical solutions obtained from equilibrium adsorption theory [30] as the skeleton of the analytical model and incorporate mass transfer effects via a correction factor introduced to the model. By use of the corrected equilibrium adsorption based model, a

reference optimum point is obtained which is then utilized to limit in its vicinity the search region explored for further optimization by incorporating mass transfer.

The reference optimal solution is then used as an initial guess for a full scale optimization. Now the computationally expensive kinetic models can now be used in a full scale optimization engine since a sound initial guess is available. This approach is advantageous since it greatly expands the number and range of possible variables or objective functions that can be included into the optimization problem since those can be tackled in the first stage of optimization. Moreover, financially relevant objective functions such as the NPW for the TSA project over the course of the plant life of the project can now be considered as the objective function. Additionally, multi-start based optimization methods can be employed in arriving at the reference solution since all the equations considered in the first step are analytical. To the best of the author's knowledge, applying this approach to the design of adsorption systems contains a high degree of novelty.

1.3 THESIS STRUCTURE

The thesis is comprised of seven chapters. Chapter 2 begins with basic background information on the Claus process. In addition, technical aspects of pilot tested and commercially implemented TGCU technologies are reviewed. Following, reported economic studies on the TGTU technologies are presented. The review is followed by a techno-economical comparison of the TGTU technologies wherein the merits of the adsorption based approach over other technologies are stated. Following, a process description of the proposed TGTU system and operation philosophy are laid. The chapter

ends with a simulation study attempting at assessing the ultimate expected recovery attainable via an adsorption based process.

Chapter 3 contains the fully detailed kinetic model of the adsorption process. A review is presented of the available analytical and numerical solution approaches to the model. The selected model and its merits are presented afterwards. The chapter ends with presenting simulation results of the selected model, the preferred solution approach and a discussion of its properties.

Chapter 4 addresses the details of the proposed optimization algorithm. The chapter starts with a review of adsorption swing optimization studies. Following, the proposed optimization algorithm is discussed. The full-scale optimization problem is then presented. The chapter ends with presenting the results of the solution of the optimization problem for two hypothetical cases which attempts at understanding the topology of the solution space of the objective function.

Chapter 5 presents a literature survey of H_2S adsorbent classes. Examples from the presented classes are reported along with their advantages and limitations. An adsorbent is selected among the reviewed materials. The results of a thorough experimental assessment of the selected adsorbent from a structural perspective is then presented. The chapter ends with the results of breakthrough and regenerability tests of the selected adsorbent accompanied with regression of the obtained experimental data using the selected model in Chapter 3. Kinetic and thermodynamic properties of the selected adsorbent necessary for the optimization are obtained from the regressed model. Chapter 6 presents a real case study in which the experimentally determined properties of the selected adsorbent are

implemented on a real industrial feed. The optimization algorithm described in Chapter 4 is then implemented in order to arrive at a realistic estimate of the economics of the proposed TGTU system. The economics of the optimized system are then compared to reported figures for some of the commercial technologies. The final chapter presents the conclusions accompanied with the suggested future work.

CHAPTER 2: CLAUS TAIL GAS CLEAN UP PROCESSES

2.1 INTRODUCTION

Since the birth of the natural gas processing industry, the Claus process has been an integral part of the processing plant as the reliable mean for recovering sulfur from acid gases [31]. Sulfur purity and price were the main drivers for the early commercial application of the Claus technology [5]. For that purpose, the conventional Claus unit achievable sulfur recovery of 97% was deemed adequate [5]. With increasing stringency in environmental regulations, the driving force for higher recoveries became predominantly environmental. Current regulations enforce achieving recoveries in excess of 99.9% [3]. Equilibrium limitations impede the conventional Claus process from achieving recoveries beyond 98% [5]. An extra unit is commonly added to the Claus unit in order to push the achieved recovery up to the target value. This unit is termed the Tail Gas Clean up Unit (TGCU). This chapter presents a general background on the Claus process and the relevant reactions. Following, a review of commercialized and pilot tested TGCU technologies is presented. Afterwards, an economical assessment and a technical comparison of the reviewed TGCU is presented where the implementation of the Temperature Swing Adsorption (TSA) unit is argued. The sections also includes the results of Promax™ simulations aimed at assessing the potential of the TSA unit in achieving the target recovery. The chapter ends with presenting the proposed TSA unit location and expected utility requirements.

2.2 THE CLAUS PROCESS

2.2.1 PROCESS DESCRIPTION OF THE CLAUS TECHNOLOGY

As shown in Figure 2.1 [32], two reaction stages comprises the Claus process: i) the thermal stage and ii) the catalytic stage. In the thermal stage, 1/3 of the inlet H_2S stream is combusted with sufficient oxygen to produce SO_2. Preheated ambient air is commonly used as the oxidizing reagent. Oxygen enriched stream are used in cases where capacity increases in existing plants are pursued [33, 34]. In conventional Claus units it is critical to maintain a ratio of 2:1 between H_2S and SO_2 as it greatly determines the final sulfur recovery [35]. Temperatures of exhaust gasses from the combustion stage usually lie within the range 930-1200^oC. At such temperatures the endothermic formation of the diatomic sulfur (S_2) is favored. Figure 2.2 summarizes the main reactions that exist within the Claus unit [5, 36]. Figure 2.3 depicts the temperature recovery profile of the Claus unit [36]. Several studies were reported on the kinetics of the H_2S-SO_2 reaction [37]. Hawboldt et al. studied the reaction kinetics at conditions which assures the validity of the plug flow reactor model. Results of the study suggest first order dependency of the global forward reaction rate on H_2S concentration and ½ order dependency on SO_2 concentration in agreement with the reaction stoichiometry. The reverse reaction rate dependencies are also in agreement with the reaction stoichiometry (i.e. reaction between S_2 and H_2O).

Activation energies of the forward and backward reactions were 49.9 and 44.9 kcal·mol^{-1} respectively. In addition to the H_2S-SO_2 reaction, direct H_2S thermal splitting occurs at the Claus furnace conditions. Several kinetic studies were reported for the H_2S splitting and subsequent recombination at the Claus furnace conditions. Kaloidas and Papayannakos observed first order dependency of the splitting rate on H_2S concentration [38]. The proposed mechanism suggest a multistep free radical pathway

in which the rate limiting step is the H_2S partial splitting to HS and S radicals. The reported activation energy of the reaction is 46.8 kcal·mol^{-1}. Roth and Barner study confirms the first order dependency of the reaction rate even at temperatures beyond the Claus furnace limits [39]. For the recombination reaction, Dowling and co-workers have studied its kinetics and suggested a first order dependency of the rate on H_2 and S_2 concentrations [40]. They also reported decomposition reaction activation energy of 48 kcal·mol^{-1} in close agreement to Kaloidas et al. results. The recent kinetic data published by Hawboldt and co-workers further confirms the reported activation energy [41]. The thermal stage of the Claus unit is responsible for achieving two thirds of the total SRU recovery.

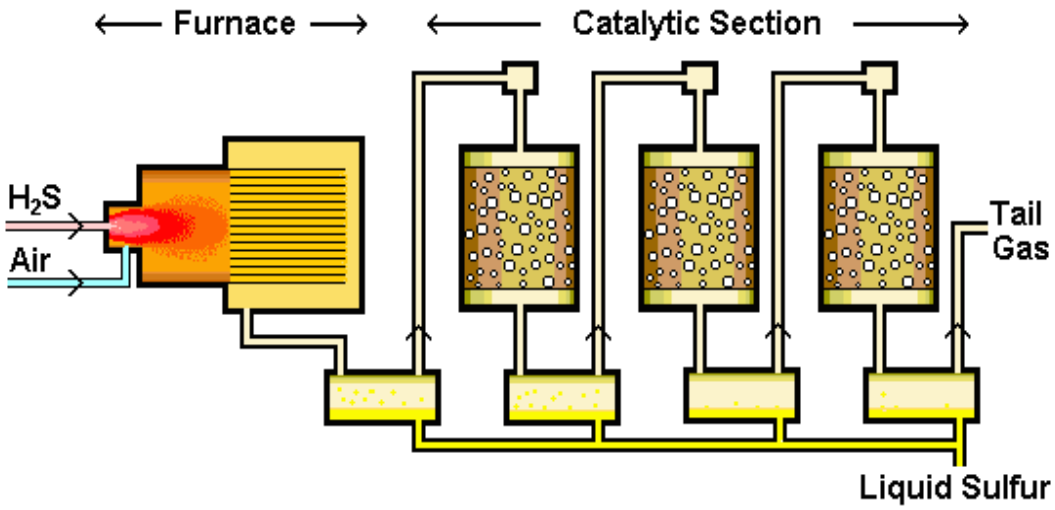

Figure 2.1/P-13 Schematic of the Claus process [32]

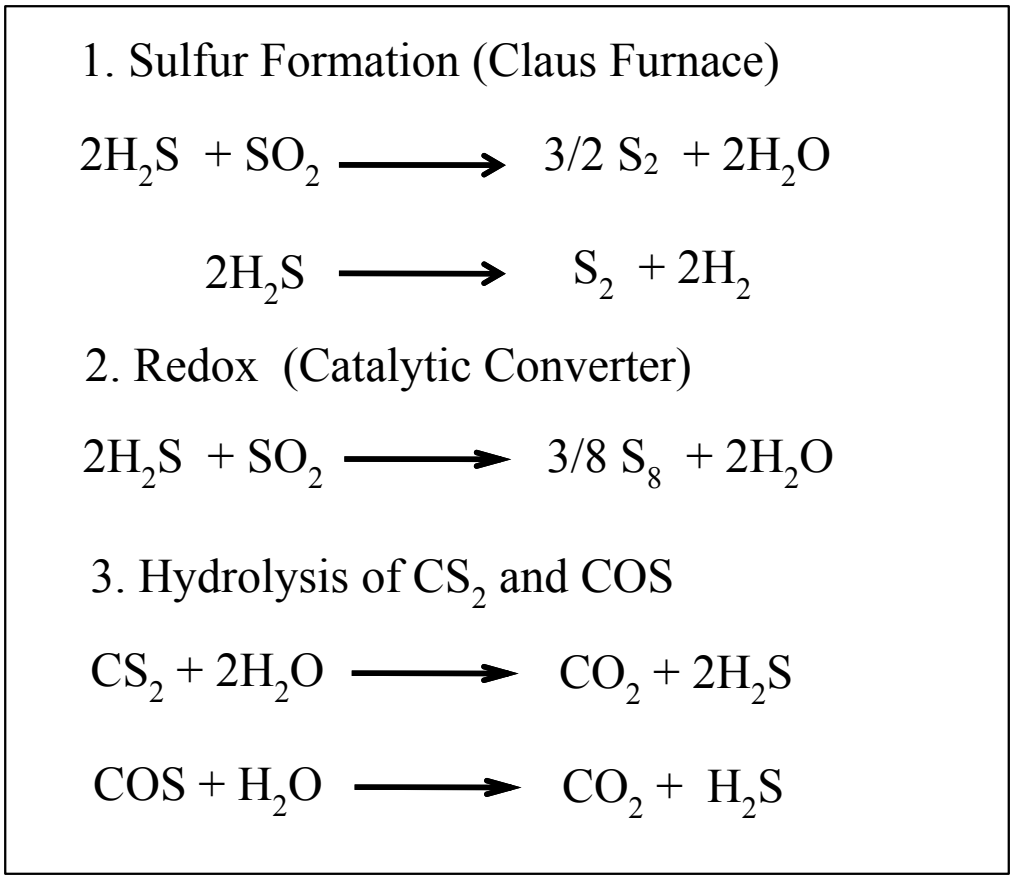

Figure 2.2/P-14 Major Reactions in Modified Claus Process [36]

In addition to H_2S combustion and sulfur formation, the Claus furnace is also designed to promote complete destruction of catalyst detrimental contaminants such as NH_3 and BTEX (Benzene, Toluene, Ethylbenzene, and Xylenes). Furthermore, the furnace is also responsible for the formation of undesired products such as CO, COS, and CS_2 [5]. Clark and co-workers studied the pathways of the COS and CS_2 formation within the Claus furnace [42]. They concluded that the pathways leading to the formation of COS and CS_2 are very complex. Other kinetic studies reported rate expression for specific pathways of the mechanism. Karan et al. studied COS formation via the reaction between CO and S_2 [43]. The global reaction rate exhibited first order dependencies on CO and S_2 concentrations with an activation energy of 43.0 kcal·mol^{-1}. In another study by Karan and Behie, the CS_2 formation reaction rate via methane-sulfur route was

reported to exhibit first order dependency on the reactants with an activation energy of 38.2 kcal·mol^{-1} [44]. Both COS and CS_2 have detrimental impact on the ultimate achievable recovery, and hence are usually destroyed by hydrolysis reactions during the catalytic stage [45].

Following the furnace, a waste heat boiler is added to recover the excess heat from the furnace effluent via the generation of high pressure steam. The waste heat boiler is typically designed as a multi-pass shell and tube heat exchanger. Furnace effluents occupy the tube side while the shell side is occupied by high pressure boiler feed water. Several reactions occur in the waste heat boiler including H_2-S_2 recombination and COS formation via the CO-S_2 routes [46].

The latter contributes the majority of the COS formed [46] . In order to minimize the formation of COS and sulfur loss, waste heat boiler designs which achieve rapid quenching are desired. In a study done by Nasato et al., reduction of the tube diameter from 2'' to 1'' achieved 21% increase in H_2 effluent concentration [46]. Furthermore, increasing the heat transfer area, led to similar increases in the H_2 concentration.

Effluent gas stream from the waste heat boiler is introduced to a sulfur condenser in order to liquefy the sulfur from the gas phase before introducing the gas to the catalytic stage. The catalytic stage is comprised of a series of gas reheaters, catalytic reactors and sulfur condensers. In each stage, effluent gas is re-heated to a specific temperature and introduced into a catalytic reactor utilizing activated γ-alumina as the catalyst with the exception of the first reactor which also contains a TiO_2 catalyst for the purpose of COS and CS_2 destruction. Although γ-alumina can catalyze the conversion of COS and CS_2, TiO_2 exhibits higher activity due to its ability in promoting CS_2 and COS reaction with SO_2 [47]. Clark and co-workers attributed the higher catalytic activity of titania in

COS and CS_2 hydrolysis to its ability in promoting CS_2 oxidation with SO_2 [47]. Due to the exothermic nature of H_2S-SO_2 reaction, the reaction equilibrium is favored at lower temperatures. However, fast catalyst deactivation due to sulfur deposition prevents lowering the gas temperature beyond the sulfur dew point [5]. Catalytic converters are operated in adiabatic conditions at the temperatures shown in Figure 2.3 [36]. Effluents from the catalytic stage are sent for further processing in the TGCU.

Kinetics of the H_2S-SO_2 catalytic reaction and the hydrolysis of COS and CS_2 over γ-alumina and Titania were reported in several studies. For the H_2S-SO_2 reaction, Mendioroz and co-workers proposed the following Langmuir like rate expression [48]:

$$-r_{H2S} = \frac{kK_{H2S}K_{SO2}C_{H2S}C_{SO2}}{\left(1+2\sqrt{K_{H2S}C_{H2S}}+K_{SO2}C_{SO2}\right)^2} \qquad (2.1)$$

where, k is the reaction rate constant, K is the equilibrium constant of adsorption, and C is the concentration in the gas phase. The expression suggests dissociative adsorption of H_2S and the rate limiting step being the surface reaction of the adsorbed species.

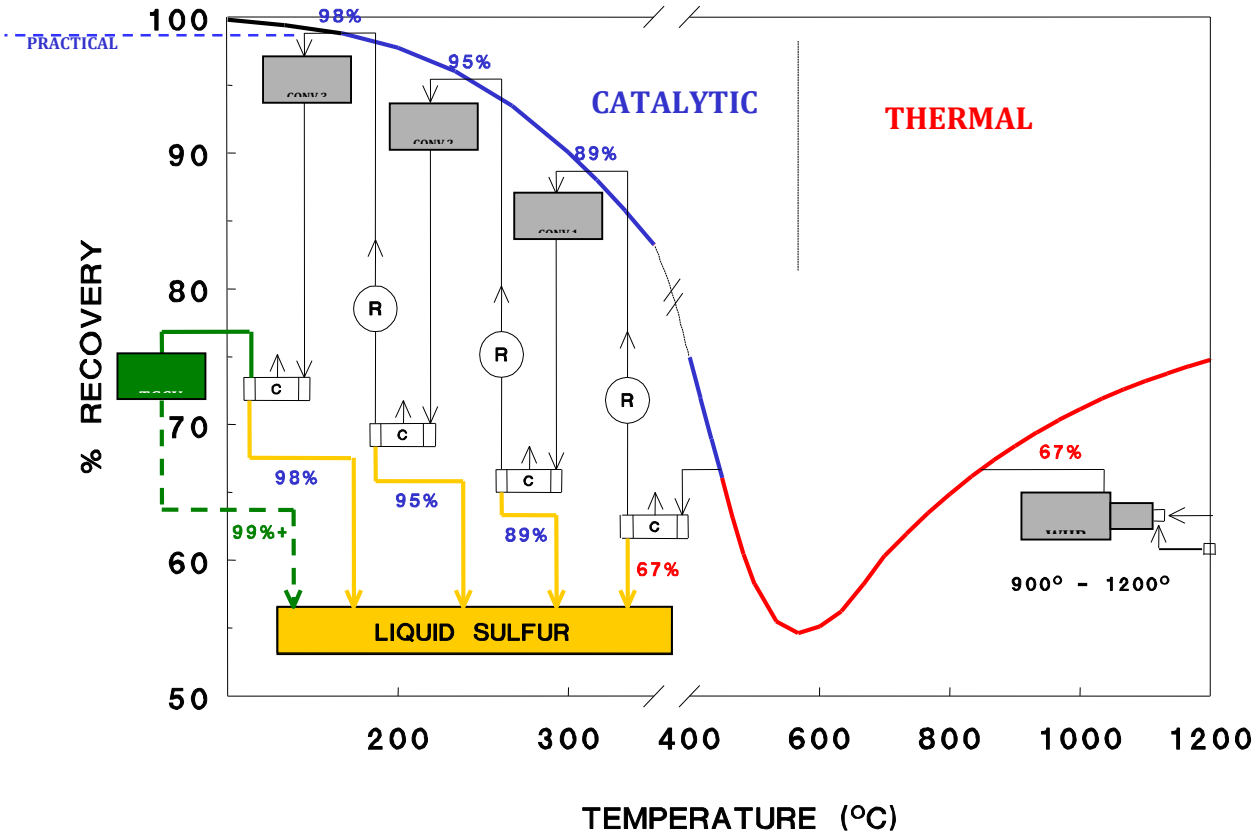

Figure 2.3/P-17 Temperature-recovery profile of the Claus unit [36]

A conventional Claus unit is usually comprised of the thermal stage components, two to three catalytic stages coupled with inter-stage heating and sulfur condensers. Further enhancement of the sulfur recovery by addition of extra stages is hindered by equilibrium limitations due to the existence of high water content in the gas stream. Removal of the water via inter-stage condensation proved to be uneconomical due to the corrosive nature of the resulting aqueous phase [5]. In situ removal of water during the catalytic reaction via adsorption was explored by Elsner et al [49]. Complete conversion was proved to be achievable, although over the course of short period of reactor operation after which water removal ceases due to adsorbent saturation. Although, this was reported in 2003, until this year (2014), commercial exploitation of this idea has not been realized.

2.2.2 PROCESS MODELING OF THE CLAUS TECHNOLOGY

Full scale modeling of the Claus unit while capturing all kinetic elements is hindered by the complexity of the reactions involved. Hence, process modeling of conventional Claus units is usually done either by assuming attainment of equilibrium conversions or using empirical correlations. Method of choice for equilibrium modeling both in the thermal stage and the catalytic stage is the Gibbs minimization technique [5]. For such purpose Sames and Paskall presented a set of empirical correlations for the purpose of determining effluent gas composition from the Claus furnace [5]. Currently, multiple commercial simulators exist in the market for the purpose of modeling the Sulfur Recovery Unit (SRU). Examples include Sulsim™ by Sulphur Experts and Promax™ by Bryan research. The coming section presents a review of commercial TGCU processes.

2.3 TAIL GAS CLEAN-UP PROCESSES

Commercial tail gas clean up approaches capable of achieving +99.9% recovery can be classified in to three categories: regenerative absorption processes, non-regenerative processes, and adsorption processes. This section presents a description of those approaches while explaining several examples from each approach. Following, a comparative study is presented involving economical parameters and other relevant parameters such as environmental impact and flexibility in operation.

2.3.1 REGENERATIVE ABSORPTION APPROACHES

In this approach sulfur species are recovered from the gas phase by selective absorption into an amine-based solvent, which is regenerated to recover the absorbed species. Those species are recycled back to the Claus furnace. Figure 2.4 presents a schematic of the Shell Claus Off Tail gas (SCOT) process, an example of regenerative-solvent based process [50]. The first step of the process involves the hydrogenation of all sulfur species to H_2S. Hydrogen gas required for this step can either be supplied by separate unit (e.g. steam reforming unit), exists within the Claus tail gas due to oxygen enriched operation coupled with optimized waste heat boiler design, or be indirectly generated via CO based water gas shift reaction [51]. For three catalytic stages Claus units, supplemental hydrogen is not required. For two stage Claus units, modern designs involve the enriching the CO concentration within the Claus tail gas by oxygen deficient combustion of natural gas in as in WorleyParsons™ reducing gas generator unit [51]. The same unit also is also used in increasing the temperature of the Claus tail gas to the required hydrogenation temperatures.

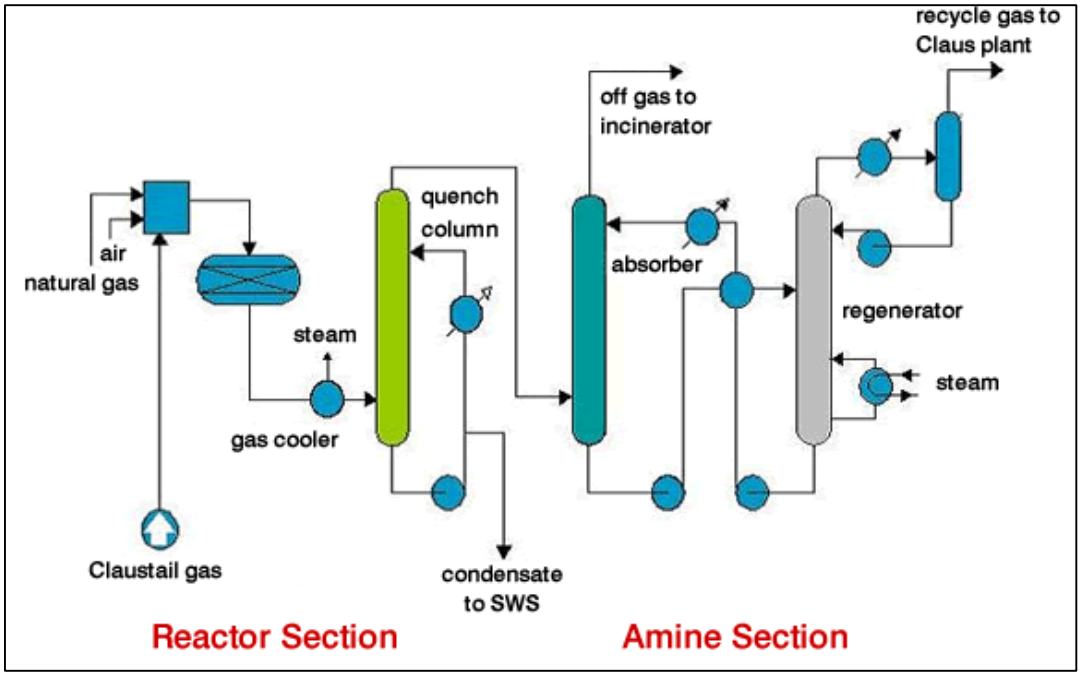

Figure 2.4/P-20 Schematic of the SCOT process [50]

The final mixed gas is introduced into a catalytic bed containing a hydrogenation catalyst typically Cobalt-Molybdenum supported on γ-alumina at a temperature in the range of 240-400^{o}C [5]. The same catalyst can also catalyze the water gas shift reaction and hence generate the hydrogen necessary for the step.

Reactions involved in the reducing step are shown in Figure 2.5 [5]. Sulfur species and oxides thereof are easily reduced and equilibrium can be achieved within relatively short residence times [52]. Catalyst hydrogenation activity towards COS and CS_2 usually deteriorates with time. As the catalyst ages, it is a common practice to increase the feed temperature beyond 240^{o}C. Typical space velocities for the hydrogenation reactor lie between 2000 to 3000 h^{-1} [51]. Patents have been filed on the reduction step by several companies including: Atlantic Richfield Company [53], SHELL [54], and Mobil oil company [55].

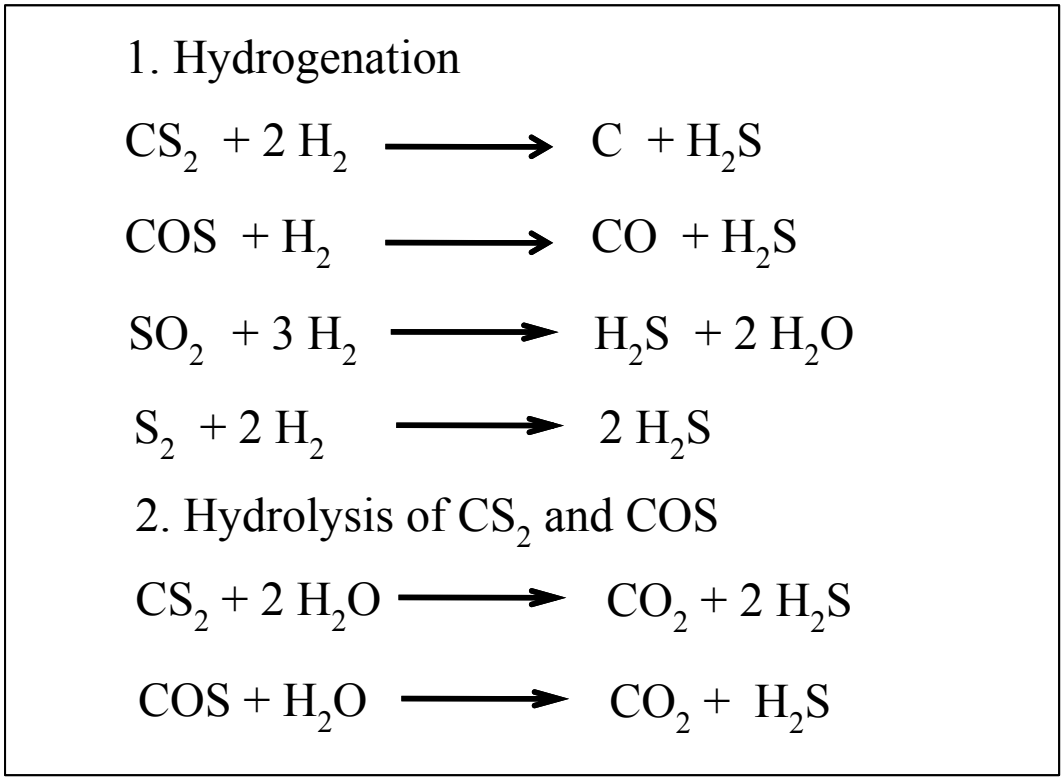

Figure 2.5/P-21 Relevant reactions occurring during the hydrogenation step of the SCOT process

Effluent gas from the reduction step is introduced to a quench column relying on water as the quenching medium. The benefits from this step are two folds: i) cool down the feed to ~40^{o}C in order to prepare it for the upcoming solvent capture based process and ii) achieve bulk removal of water in and to a lesser extent H_2S. The bulk removal of water from the Claus tail gas substantially reduces its volume and hence the size of the subsequent unit operations since by now the water content in the tail gas will exceed 20% mole. Accumulated sour water at the bottom of the column is sent to the sour water treatment unit. Outlet gas from the water scrubber is introduced into a solvent capture based process. Depending on the technology employed, different solvents can be used to attain selective removal of H_2S while assuring CO_2 rejection. The gas leaves the absorption column at a practical H_2S concentration of 1-10 ppm [5]. Such a low concentration of H_2S in the gas

does not require incineration according to many jurisdictions [5], hence eliminating the need for a final incinerator. The solvent on the other hand is thermally regenerated as to recover the absorbed H_2S in a gaseous form. Then, the solvent is recycled back to the absorption column. Outlet gas from the regenerator is recycled back to the inlet of the Claus furnace. Various solvents are commonly employed including Methyl Diethanol Amine (MDEA) [51], Diisopropanolamine (DIPA) [5], and Exxon proprietary Flexorb [56]. The solvent choice is made taking into account: i) the solvent price ii) the solvent absorption capacity towards H_2S absorption and iii) the solvent absorption capacity towards CO_2 with lower capacity being more favored.

Examples of commercial processes that follow the regenerative approach are: The SCOT™ process licensed by SHELL Petroleum [57], Exxon Flexsorb SE plus licensed by Exxon-Mobil [56], Resulf process licensed by TPA inc. [5], BSR/MDEA licensed by WorlyParsons [51]. Alternatively, all sulfur species in the Claus tail gas can be oxidized to SO_2. Following, an SO_2 capture technology is used. The Cansolv™ technology licensed by Shell and the Clintox™ technology licensed by Linde AG are two manifestations of that concept [9].

Direct oxidation of H_2S to sulfur is also implemented commercially as a mean for Claus tail gas clean up [5]. A standing manifestation for this concept is the LO-CAT process and its derivatives. The LO-CAT process relies on an aqueous solution of the trivalent form of iron. The iron is kept in solution by chelating agents. The process is comprised of three stages: 1) the absorption stage, 2) the oxidation stage and 3) the sulfur handling stage. During the absorption stage, the treated gas is contacted with the chelated iron solvent in an absorption column, ferric ions oxidizes the dissolved H_2S directly to elemental sulfur at

temperatures below the sulfur melting point. The ferric ions get reduced to ferrous ions. The resulting slurry laden with dispersed solid sulfur particles is rerouted to the oxidizer. The solvent is contacted with a stream of air which acts as the oxidant for the solvent. Ferrous ions are reoxidized to the ferric form thus regenerating the solvent active ingredient. Several side reactions can occur during the regeneration step including: thiosulfate and sulfate formation reactions.

A complete list of all reactions is presented in Figure 2.6 [5]. The regenerated solvent is then rerouted to the sulfur handling section where solid sulfur is recovered via a combination of filtration, gravitational settling vessels and/or centrifugal separation. Both H_2S absorption and O_2 absorption are strongly dependent on the pH of the solvent and its electropotential. High solvent pH promotes both oxygen and H_2S dissolution. While high H_2S dissolution rates are favored, excessive concentrations of oxygen within the solvent promotes the formation of undesired thiosulfate.

1. Absorption & Oxidation

$$H_2S \longrightarrow HS^- + H^+$$

$$2\,Fe^{3+} + HS^- \longrightarrow 2Fe^{2+} + S + H^+$$

2. Regeneration (Oxidizer)

$$2Fe^{2+} + \tfrac{1}{2}O_2 + H_2O \longrightarrow 2Fe^{3+} + 2OH^-$$

3. Side Reactions (Oxidizer)

$$2HS^- + 2O_2 \longrightarrow H_2O + S_2O_3^{2-}$$

$$S_2O_3^{2-} + 2.5O_2 \longrightarrow 2SO_4^{2-}$$

Figure 2.6/P-24 Relevant reactions occurring in the LO-CAT process [5]

Typically the solution pH is maintained between 8 and 8.5 [5]. Potassium hydroxide is continuously added as a mean for pH control. The solvent flow rate is the major factor determining the capital cost of the unit [5]. It is proportional to the gas flow rate, the H_2S concentration and inversely proportional to the iron concentration. Equipment size can be substantially reduced when the iron concentration is increased but it is associated with an increase in the initial cost of the solvent (due to higher concentration required of chelating agent), and subsequent increase in operating cost due to make up requirement.

The original design of the LO-CAT process relied on a solution with a ferric concentration typically twice the stoichiometric requirement [58, 59]. The process flow diagram is shown in Figure 2.7 [59]. The iron concentration in the solvent typically ranges between 500 and

1500 ppm [60]. Treated gas and the solvent are firstly introduced to a mixer (a static mixer or a Venturi pre-contactor). The gas/liquid mix is then introduced to the absorption column. While packed columns offer better mass transfer rates, due to solid sulfur plugging their use is limited to low H_2S gas streams [5]. Commonly, a liquid filled sparged column is employed as the absorption column in order to prevent plugging by solid sulfur. Typical sulfur loadings of the used solvent varies between 0.2 to 0.6 wt% [5]. The used solvent is then rerouted to the oxidizer vessel for the regeneration purposes. The vessel is designed as to allow gravitational settling of the sulfur particles thus forming concentrated slurry at the bottom of the oxidizer vessel.

Regenerated solvent is recovered from the sulfur laden slurry by phase separation and is recycled back to the absorption column. The sulfur laden slurry is routed to the sulfur handling system. Depending on the sulfur concentration, a sulfur melter can be used as mean for sulfur separation via melting of sulfur particles followed by liquid/liquid separation [5]. ARI technologies introduced a modified design to the LO-CAT system whereas the absorption column and the oxidizer are combined into one vessel. The system is designed to for applications requiring low concentrations of iron in the solvent (250-500 ppmw) [5]. Figure 2.8 presents the process [5].The combined design offers cost savings by reducing pumping power due to absence of piping. The savings are offset by the need for chemical additions as to combat the formation of side products [5].

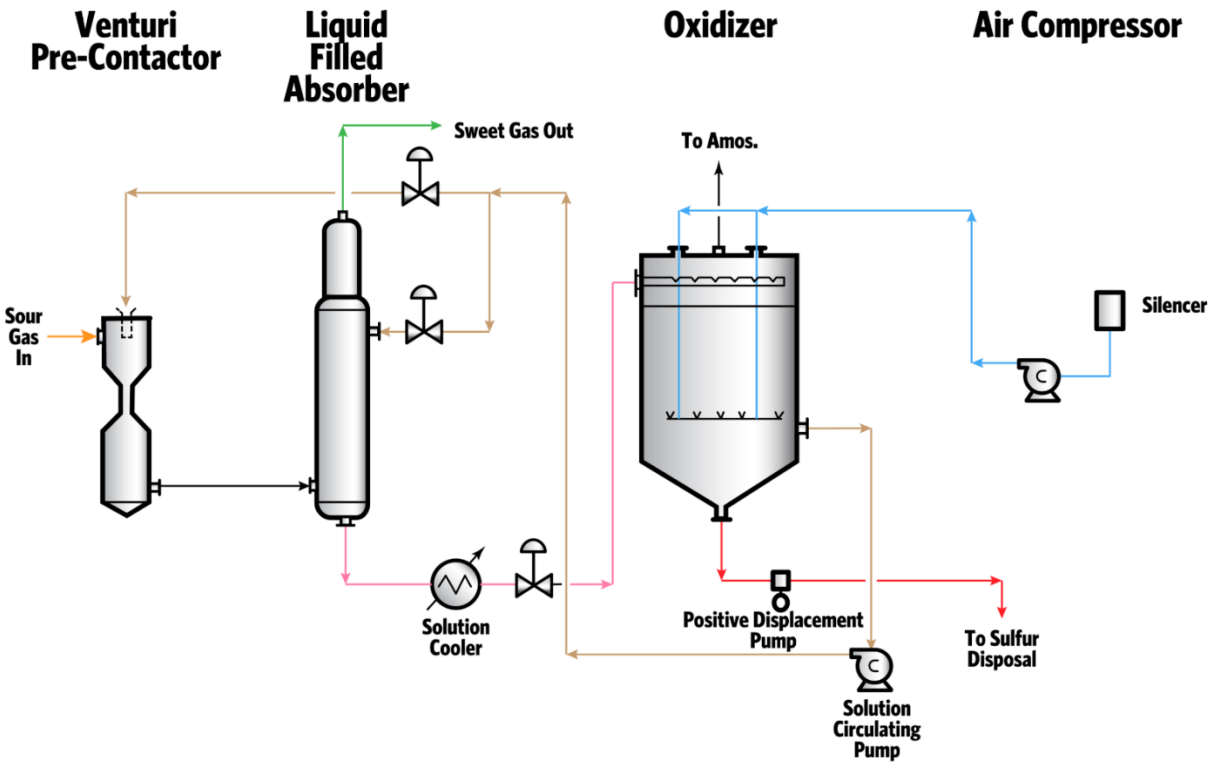

Figure 2.7/P-26 Process Flow diagram of the LO-CAT process (reproduced from [5])

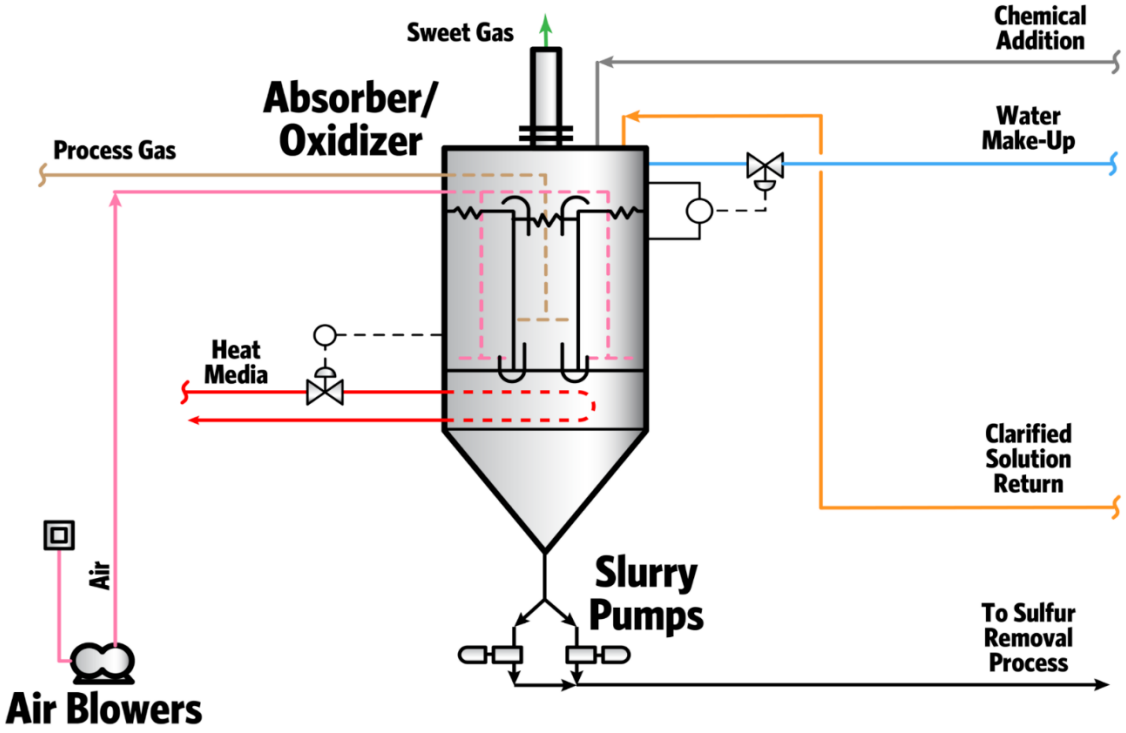

Figure 2.8/P-27 Process Flow diagram of the LO-CAT Auto-circulation process (reproduced from [5])

Current Commercial TGTUs rely on the latest development of the LO-CAT process; the LO-CAT II. The LO-CAT II process brings substantial reduction in the iron concentration to levels slightly below the stoichiometric ratio and minimizes the extents of side reactions via the use of a staged controlled oxidizer [5]. A proprietary oxidizing agent is added in order to assist the oxidation of H_2S. The oxidizer vessel is designed with a flat bottom and equipped with baffles separating the oxidation stages. The baffles force the solvent to follow a zig-zag path across the oxidizer. The design of the oxidation stages assure minimal contact time between the solvent and the oxidizing gas. Formation of side products is hence kinetically suppressed.

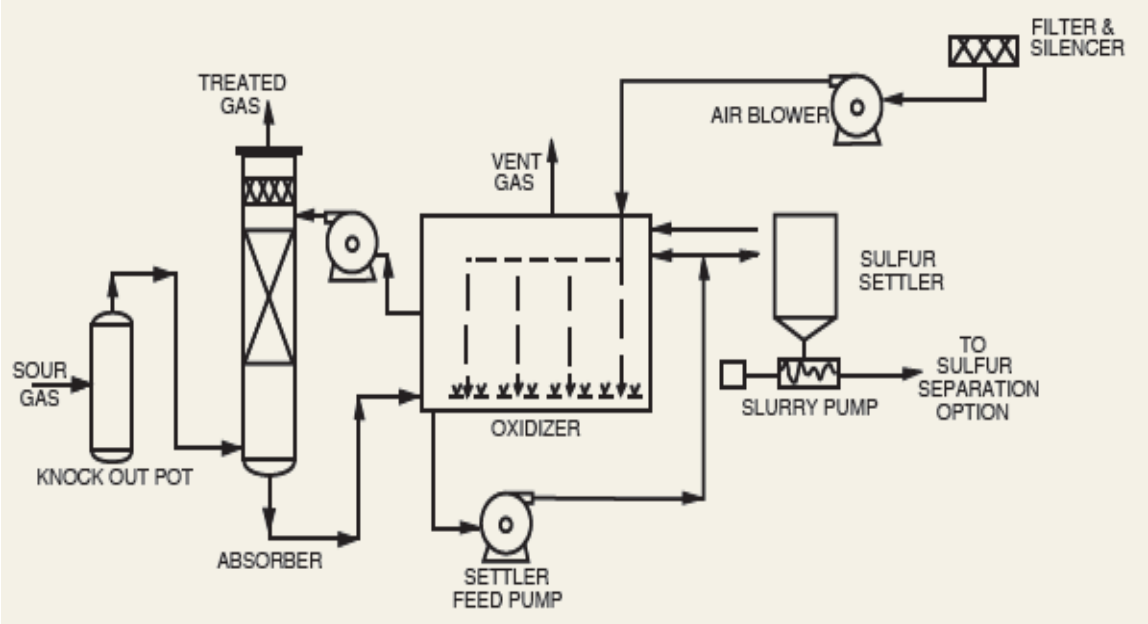

Figure 2.9/P-28 Process Flow Diagram of LO-CAT II process [61]

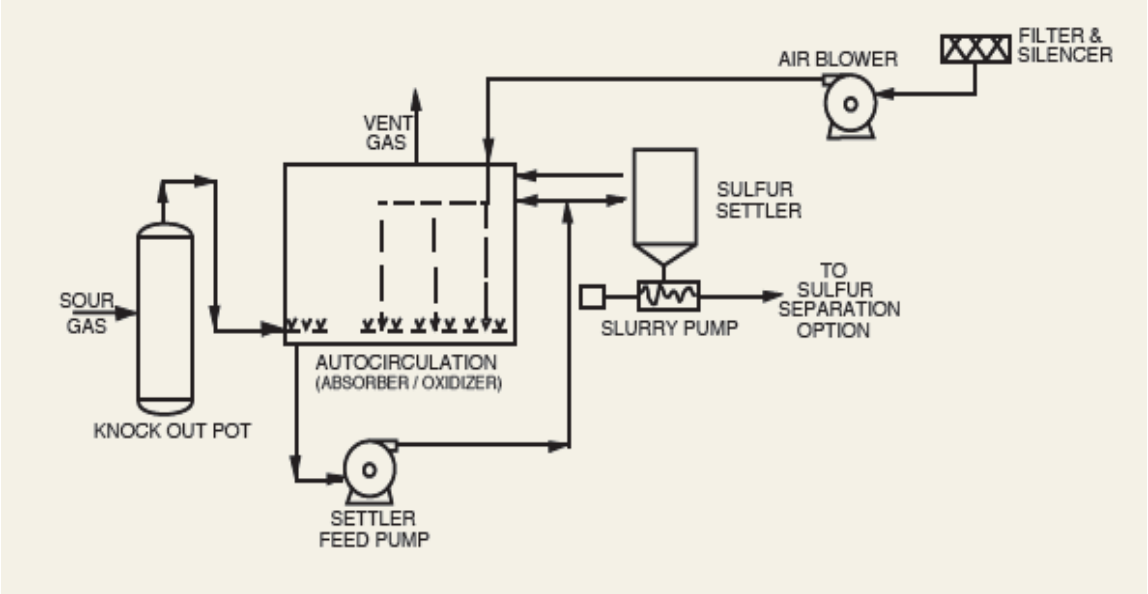

Figure 2.10/P-29 Process Flow Diagram of LO-CAT II process with auto-circulation option [61]

Currently, Merichem® Company commercializes two realizations of the LO-CAT II process shown in Figures 2.9 and 2.10 [61]. The AquaClaus process introduced by Darnell Engineering aimed at performing the Claus reaction in liquid phase at temperatures sufficient low to near complete conversion [9]. First, all sulfur species are completely oxidized to SO_2. The formed SO_2 is then absorbed by a proprietary phosphate based solvent. The solvent is then regenerated by an H_2S containing stream via the Claus reaction. Since the temperature of the solvent is low, the equilibrium limits of the Claus reaction are expanded thus pushing the reaction to near completion. According to the Gas Technology Institute report, two pilot units were tested with capacities of 6 and 1.9 long tons of sulfur per day [9].

2.3.2 NON-REGENERATIVE BASED APPROACHES

Non-regenerative approaches employ a solution enriched with a component that can chemically binds SO_x species. Among the commercial application of these technologies in the sulfur recovery field is the SuperClaus/DyneWave technology licensed by Jacobs Comprimo and MERCS global [62, 63].

A schematic of the DyneWave® system is presented in Figure 2.11 [63]. Claus tail gas is mixed with a stream of air and is passed through a SuperClaus bed for partial oxidation of H_2S to elemental sulfur. Any remaining sulfur containing species are oxidized to SO_x. The outlet stream passes through a sulfur condenser for elemental sulfur removal. The effluent gas is then introduced to a DyneWave reverse jet based technology employing an aqueous solution of sodium hydroxide. Application of the reverse jet based technology is claimed to greatly enhance rate of mass transfer from the gas phase to the aqueous phase by producing a highly turbulent froth. In addition, the MERCS and Jacobs Comprimo claims a 5 to 7 times enhancement in processing capacity as compared to the flooding limited conventional scrubbing column due to the reverse jet technology [62]. SO_x species react with NaOH forming sulfur based sodium salts. A purge stream is drawn from the system continuously as to prevent accumulation and subsequent precipation of salts within the system. Moreover, a makeup stream of fresh NaOH solution is also introduced. Employment of the SuperClaus/DyneWave technology ensue major reductions in plant footprint amounting to almost 60% compared to a SCOT based plant as claimed by Koscielnuk et al. [7]. Additionally, the technology is claimed to be highly robust against process setbacks. However, the continuous need for NaOH make up offset the gains by ensuing significant additional operating costs. Furthermore, a typical plant producing 400

metric tons of sulfur per day achieving 99.9% recovery is expected to produce 2-6 tons of sodium sulfate salts every day. Unless a plausible market sink exists for those salts, the financial burden of managing such waste may relinquish any chances for a profitable standpoint of the SRU project.

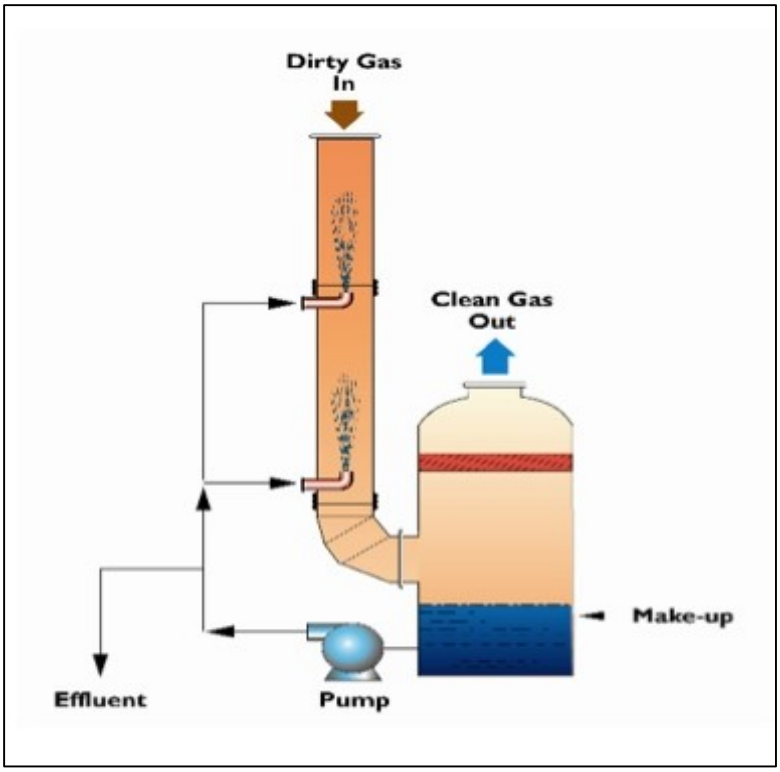

Figure 2.11/P-31 Schematic of the DyneWave reverse jet technology [63]

2.3.3 ADSORPTION BASED PROCESSES

Utilization of adsorption-based processes for Claus tail gas clean up did not find wide application as confirmed by the presence of only two pilot tested technologies in the SRU market. Those are AMOCO's Extremely Low Sulfur Emission (ELSE) process [64] and the Mobil Oil SOx treatment process (MOST) [12, 65]. Figure 2.12 depicts a generic process flow diagram for both technologies.

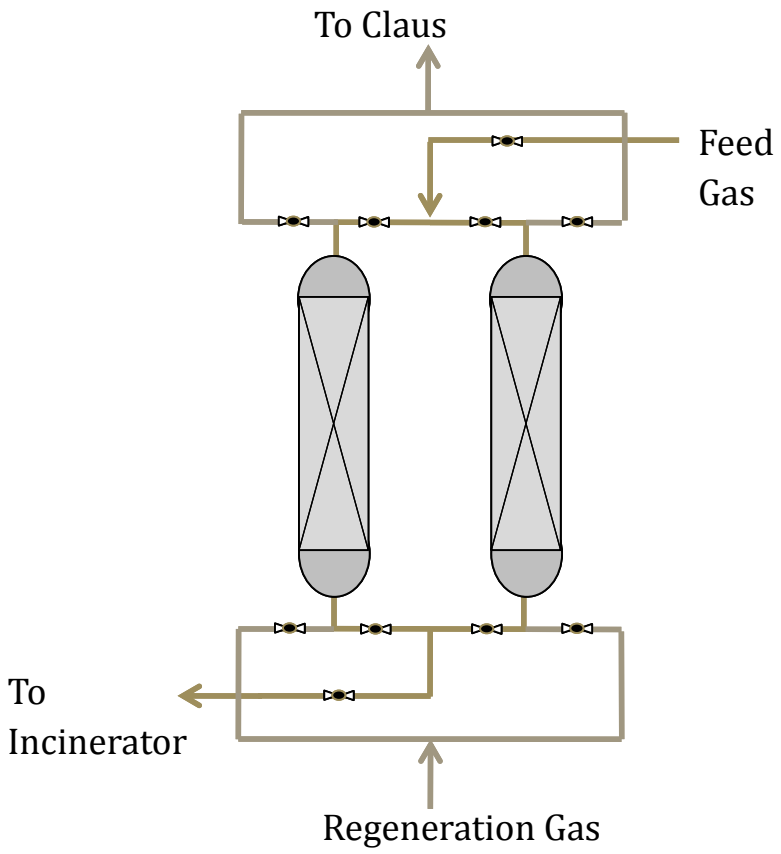

Figure 2.12/P-32 Schematic of the ELSE and MOST technologies

The ELSE technology utilizes a Zinc Oxide based sorbent targeting the removal of H_2S from the Claus tail gas. In order to assure complete removal of sulfur species, the ELSE adsorbent vessels are usually preceded by a hydrogenation bed as to achieve complete conversion of sulfur species to H_2S. Two sets of vessels containing ZnO sorbent are operated cyclically i.e. one vessel undergoing adsorption while the other undergoing regeneration. During the adsorption step, ZnO reacts with sulfur species to form ZnS. The sorbent is regenerated via oxidation using a dilute air stream at a temperature of 600^{o}C, which is rerouted back to the Claus process [64]. Such a high regeneration temperature is necessary in order to assure complete destruction of sulfates formed during the

regeneration step. According to Kohl et al as of 1996 the ELSE technology did not find any commercial application [5]. A similar manifestation of the adsorption based approach is the Z-Sorb process introduced by Philips Petroleum Company [66]. The unit has a similar arrangement to the ELSE process.

The MOST process on the other hand involve complete oxidation of all sulfur species to SO_x and subsequent adsorption on a solid sorbent at 650^oC [65]. Figure 2.13 presents the reactions involved in the process. Regeneration of the sorbent is done by introducing a reducing gas of H_2 thus reverting the sorbent to its oxide form. The study conducted by Stern et al. concluded that $Mg_2Al_2O_5$ promoted with cerium and vanadium possesses the highest capacity towards SO_x adsorption (> 50 wt%) based on breakthrough studies utilizing a gas containing 1% SO_2, 4% O_2, 10% H_2O, and balance nitrogen [65].

No study has been conducted to assess the sorbent resistance towards other competing species including CO and CO_2. Till this date (10/21/2014), none of the aforementioned technologies achieved commercialization [67, 68]. This might be attributed to a number of deficiencies the technologies suffer from. Firstly, both technologies require high temperatures during either regeneration or adsorption steps in excess of 600^oC. Such a high temperature in this sour service forces employment of stainless steel based alloys and hence considerably raise the capital cost of the vessels and its associated pipe networks [69]**.** Cost of sorbent is also quite high considering utilization of rare metals as in the MOST process. For the ELSE process, the ZnO sorbent cost around 7.2 $\$\cdot kg^{-1}$ [70].

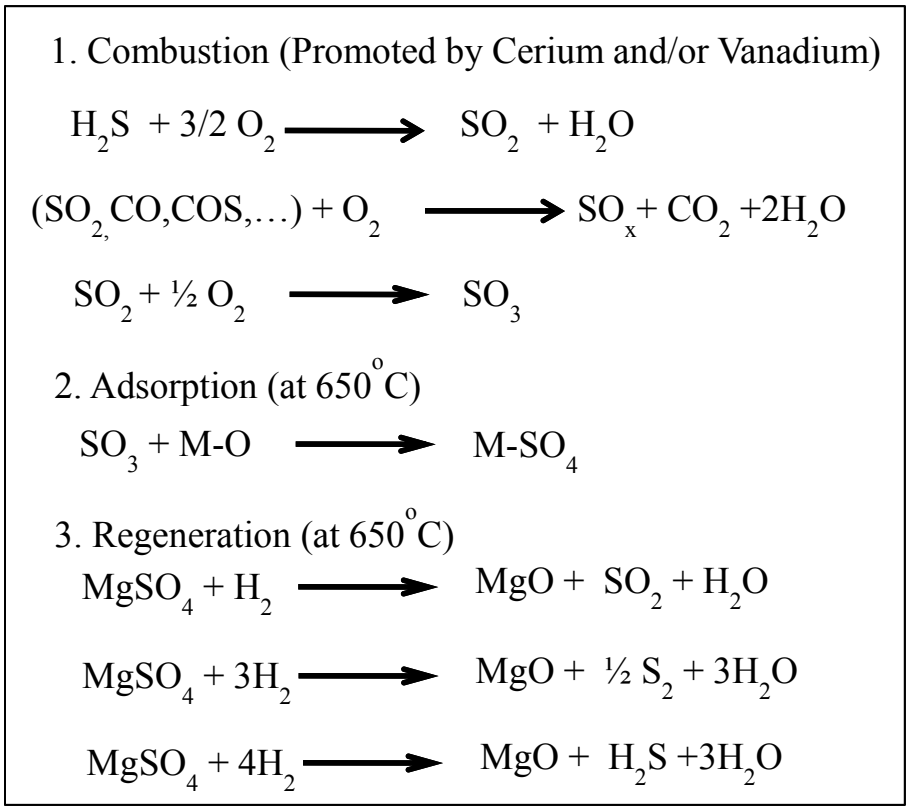

Figure 2.13/P-34 Relevant reactions in the MOST process [65]

2.4 A COMPARISON BETWEEN TECHNOLOGIES

Recent publicly accessible economic studies on the aforementioned technologies are limited. Early assessment of the economics of the SCOT process was reported by Harvey and Verloop [5]. Addition of a SCOT unit to a conventional SRU doubles its Capital cost. Furthermore, the estimated operating cost ensued by the SCOT unit amounts to 16 $/ long ton of sulfur processed. The more recent studies of Koscielnuk et al. and the Gas Technology Institute further confirm those findings [7, 9].

The Gas Technology Institute published a report, which studied the operating and capital costs of 14 TGTU options including SCOT, Clintox, and Lo-CAT II for low capacity SRUs

(< 100 long ton/day) [9]. Four cases were studied for two design capacities (10 and 70 long ton of sulfur per day) and two feed gases (67% H_2S and 30% H_2S). All units were assumed to be preceded by a conventional Claus unit. Costs relative to a conventional Claus unit were reported. Figures 2.14 and 2.15 show the relative operating and capital costs estimated for the case of 67% H_2S and a plant capacity of 76 long ton of sulfur per day. Clearly, all the aforementioned technologies ensues relative capital costs in excess of 100% with the exception of LO-CAT process (~50% relative capital cost). Furthermore, all of the studied options introduce operating costs on par with the Claus unit.

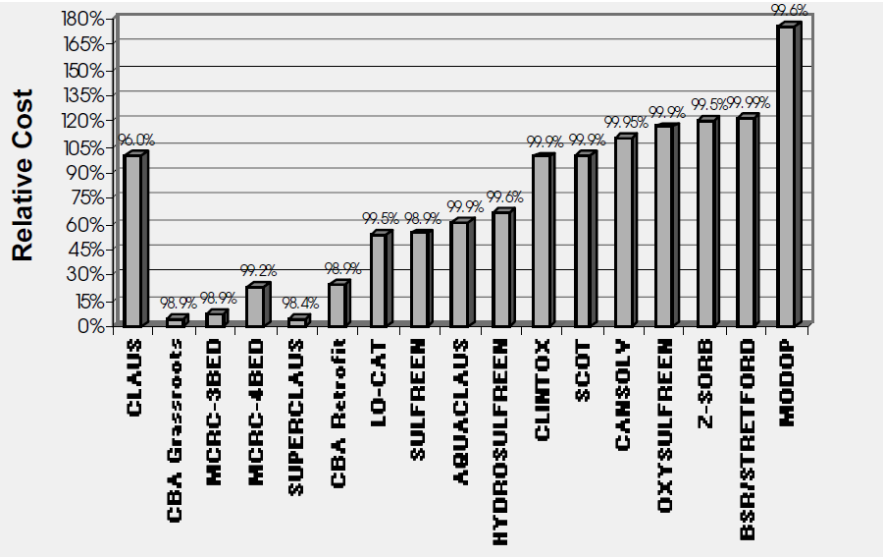

Figure 2.14/P-35 Relative capital costs of TGTU technologies [9]

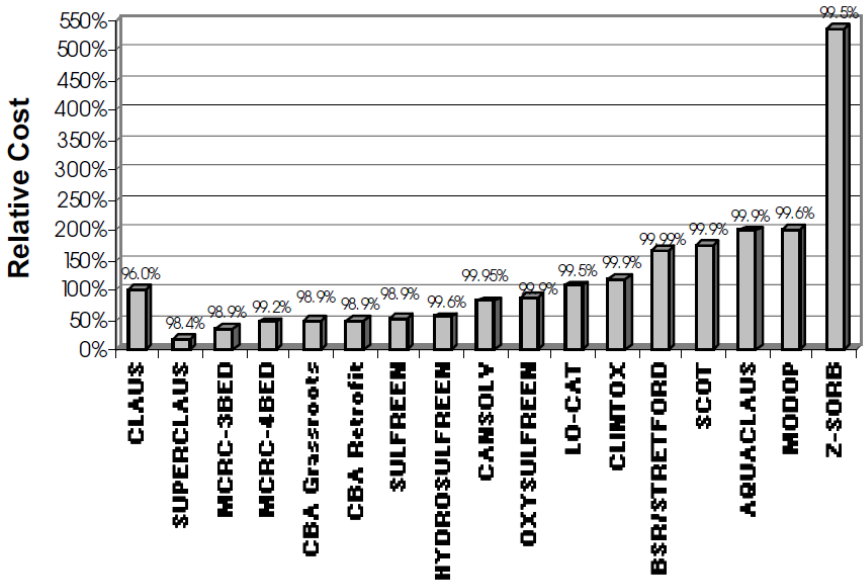

Figure 2.15/P-36 Relative operating costs of TGTU technologies [9]

The technological concepts discussed thus far are the only commercialized concepts capable of achieving +99.9% sulfur recovery (<50 ppm of SO_x in flue gas). Regenerative based approaches have by far the widest application in the world as compared to the other technologies. Non-regenerative based processes have only been implemented recently with the erection of 7 units as indicated by Koscielnuk et al. [62]. The major advantages gained from employment of the regenerative and non-regenerative based approaches lies in their ability to maintain the targeted sulfur recovery (+99.9%) while being capable of withstanding process fluctuations. However, commercialized manifestations of these approaches results to an increase of 80-100% in the SRU capital cost while ensuing additional operating costs (i.e. not including the conventional Claus unit operating cost) which can surmount the Claus unit cost [63]. Moreover, these processes necessitate in-house generation of hydrogen gas, which requires erection of a steam-reforming unit. Plant footprint area is also increased dramatically to around 150% of the original SRU area [63].

Considering the extreme volatility of the sulfur price in the market (e.g. Sulfur price in the period of 2010-2012 varied between 100-250 $\$\cdot MTS^{-1}$ [71]), chances of sustaining a profitable standpoint over time are compromised. As for the adsorption based processes, reported figures only exists for the Z-Sorb. To the best of the knowledge of the author, there has been no commercial implementation of this technology. Table 2.1 presents a comparison between the various technologies' pros and cons.

Category	Regenerative Solution	Non-regenerative	Adsorption
Robustness	High[a]	High[b]	U/K
Environmental Impact	Low	High due to waste	Low
Floor Foot print (% of SRU)	50-70 %[b]	20-30%[b]	<10%[c]
Capital cost (% of SRU)	40-50%[b]	30%[b]	<10%[c]
Operating cost ($\$\cdot ton^{-1}$)	~20[b]	~20[b]	< 4[c]

a: From ref [5]

b: From ref [63]

c: Value obtained for CuY presented in Chapter 5. Also sorbent dependent.

Table 2.1/P-37 Comparison of TGTU technologies

Based on the comparison presented in Table 2.1, we argue that a commercially competing technology should have the following merits:

- Firstly the technology should be of a regenerable nature since any side products would place an operating cost burden on the project rendering it unfeasible from an economical stand point.
- Secondly, the technology should have a small footprint thus allowing economical implementation on space limited places or where cost of land have a major contribution to the cost stand point of the project.

- Moreover, the technology should be able of withstanding process upsets without compromising low SO_x emission levels.
- Also, the regeneration step should preferably not involve utilization of gasses produced outside the fence of the SRU. Last but not least, the technology employed should be of low overall costs (costs comprising capital and operational cost) as compared to other technologies.

Arguably, adsorption based processes can encompass all those criteria provided that a proper adsorbent is implemented which has high capacities and high selectivity towards sour gas species, is easily regenerable with air at relatively low temperatures to allow usage of carbon steel alloys, retains its capacity even after thousands of regeneration cycles, and is relatively cheap. This section ends with a simulation-based study presenting qualitatively the expected attainable recovery from employing an adsorption based system.

Process simulation of a conventional SRU was conducted using Promax II® simulator with its native sulfur recovery data packages. The conventional unit is comprised of a standard once through Claus furnace coupled with three catalytic converters. A Super Claus unit is implemented for secondary recovery. Gibbs minimization algorithms were used in modeling the various unit operations [72]. In those algorithms all relevant reactions are assumed equilibrated. Moreover, the equilibrium concentrations of all the species are determined by minimizing the total Gibbs energy of the whole system. The proposed TGTU unit was modeled as a component divider considering complete removal of all heteroatomic sulfur species and recycle back to the Claus furnace. Figure 2.16 presents the converged process flow sheet of the SRU obtained from Promax II. Simulators results

matched those reported in the material balances obtained from the company operating the plant. Table 2.2 summarizes the critical results.

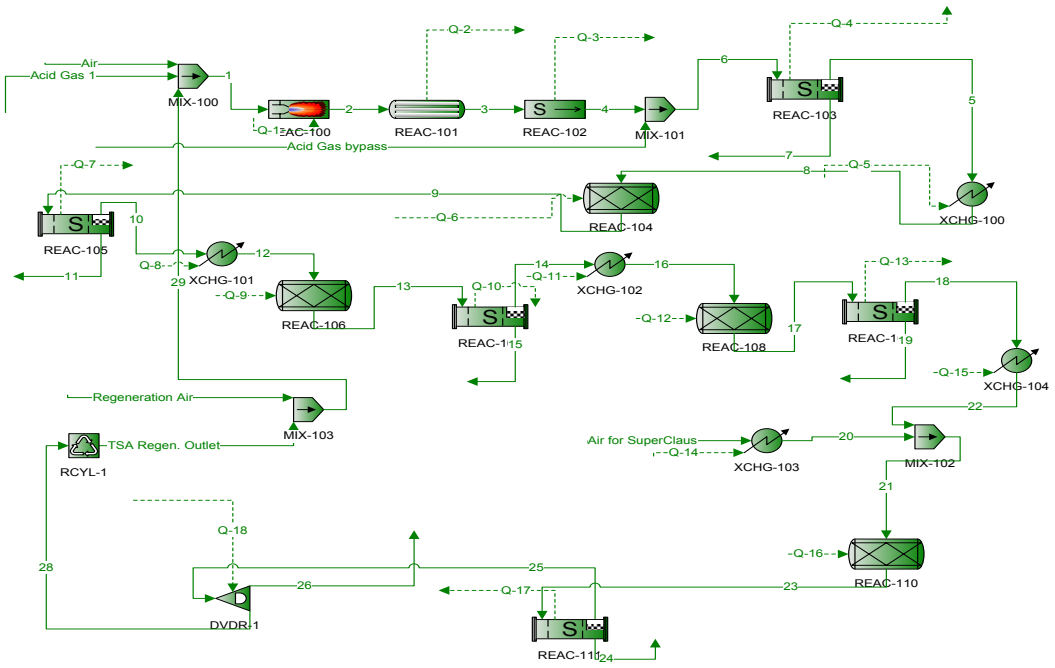

Figure 2.16/P-39 Process flow sheet of an operating SRU

Category	Simulation	Actual
Mole % H_2S	0	0.01
Mole % SO_2	0.083	0.09
Mole % CO	1.26	1.2

Table 2.2/P-39 Critical parameters comparison between Process simulation and given data

Introduction of the TSA unit and further recycle to the Claus furnace achieved convergence signifying absence of accumulation of sulfur species upon complete recycle. The sulfur recovery obtained was 99.95%. Hence, the TSA unit is expected to achieve the targeted recovery of +99.9%. This result is confirmed by pilot plant tests of ZnO sorbent through the ELSE process [5].

2.5 INTEGRATION OF THE TSA UNIT INTO THE SRU MATRIX

Finally this chapter ends with a proposed process flow scheme for the adsorption based TGTU. Two process concepts are investigated. Process concept 2 (TSA+Hydrogenation) assumes that the adsorbent targets only the capture of H_2S. Hence, a hydrogenation reactor system is employed upfront of the TSA unit as assure complete conversion of all sulfur species to H_2S. Process concept 1 assumes an adsorbent capable of capturing all sulfur species (TSA only). The process flow diagram of both process concepts are depicted in Figures 2.17 and 2.18. In process concept 2, Claus tail gas feed is firstly heated in a fired gas heater to 240^{o}C, the required temperature for hydrogenation of all sulfur species. Subsequently, the effluent gas is introduced to a typical hydrogenation reactor catalyst. The hydrogenation step targets the complete transformation of all sulfur species to H_2S in addition to significant destruction of carbon monoxide via the water gas shift reaction.

The effluent of the reactor is introduced to a water-based cooler in order to reduce the temperature to 150^{o}C. The cooled stream is then introduced to the TSA module. The TSA cycle's steps are adapted from the work of Wunder for natural gas driers design [73]. While adsorption is envisaged to occur isothermally with uniform velocity, regeneration is envisaged to simulate a phase change in which the adsorbed species transforms to the gas phase isothermally at an experimentally determined regeneration temperature. Hence the total regeneration cycle time comprises of the time required for system heating, the time required for the elusion of adsorbed contaminants, and the time required for system cooling back to the operating temperature. Details of the cycle steps and the invoked assumptions

are presented in the Supporting Information. Figure 2.19 depicts the unit integration within the SRU for typical feed conditions. The water cooler effluent is introduced to the vessel(s) undergoing adsorption. Once the contaminants' breakthrough point is reached, the Claus tail gas flow is switched to the stand-by vessels. During regeneration, a slipstream of the Claus unit air feed is re-routed using a centrifugal blower to a fired gas heater where it is heated to a temperature above the experimentally determined regeneration temperature. The hot air stream is routed to the beds undergoing regeneration for heating and regenerating the bed to fresh conditions. Finally, the air stream effluent of the centrifugal blower is introduced to the vessels undergoing regeneration for cooling purposes. The same process description applies for process concept 2 excluding the hydrogenation system.

2.6 CONCLUSIONS

This chapter addressed topics pertaining to the sulfur recovery unit and commercially available TGTU technologies capable of achieving the targeted sulfur recovery. Clearly, the substantial financial burden that is introduced by implementing a TGTU technology necessitates the search for a more cost effective option. Adsorption based technologies, despite of being proposed, did not achieve any commercial application yet. To evaluate the potential of such technologies, kinetic modeling is a key stone for a proper assessment. The upcoming chapter addresses topics pertaining to kinetic modeling of adsorption processes.

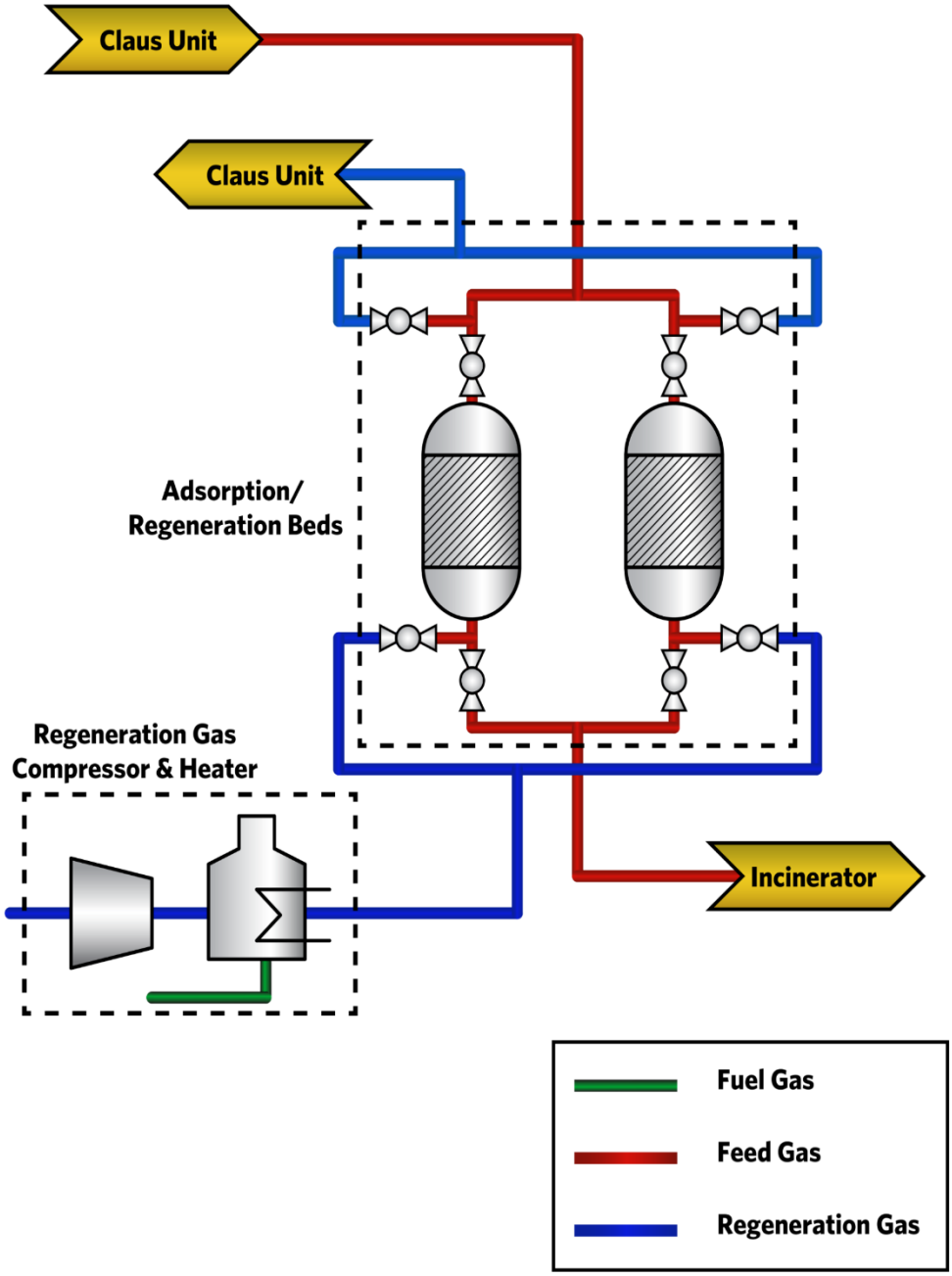

Figure 2.17/P-42 Process Flow Diagram of the proposed TGTU Unit for concept 1

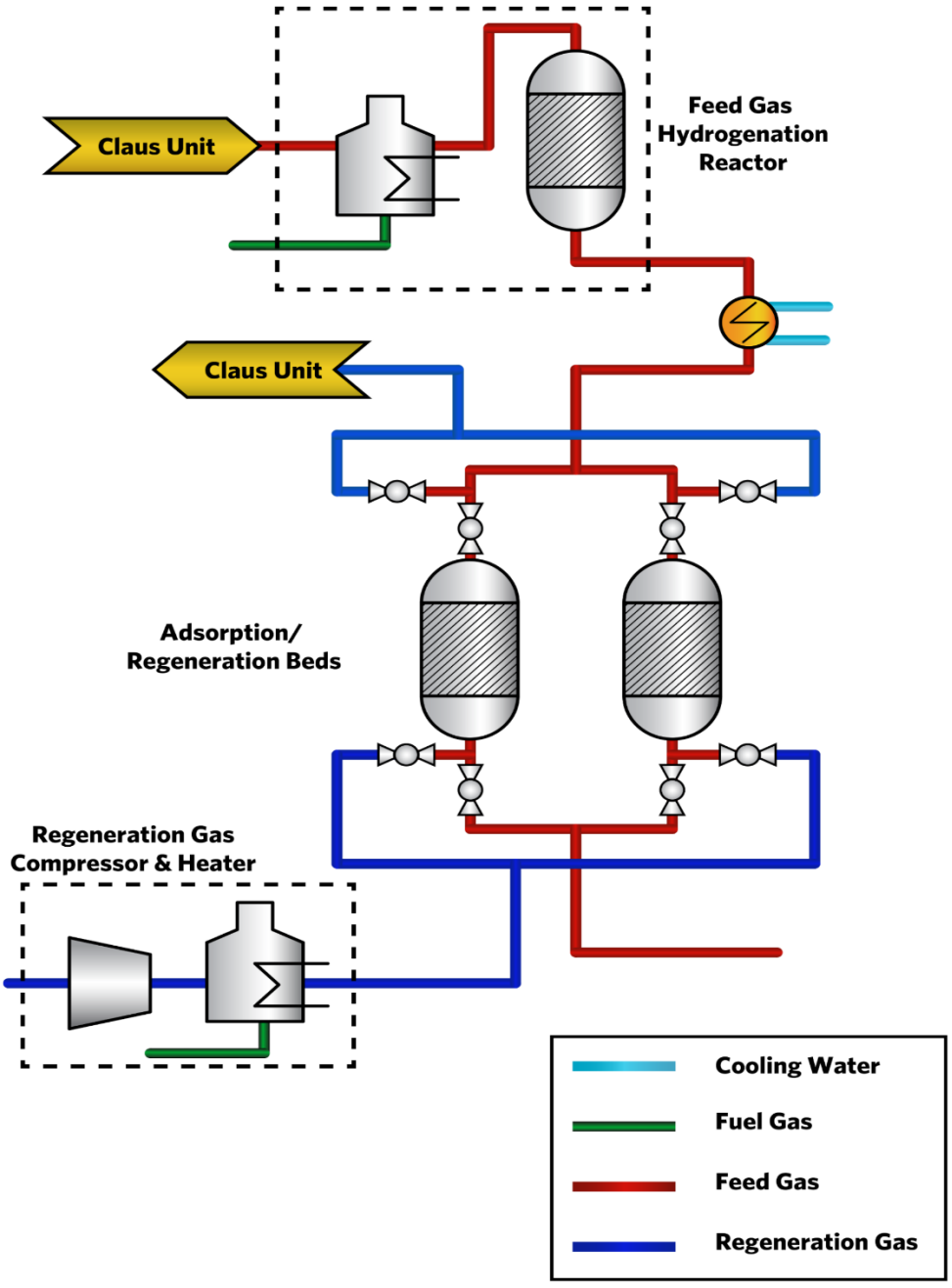

Figure 2.18/P-43 Process Flow Diagram of the proposed TGTU Unit for concept 2

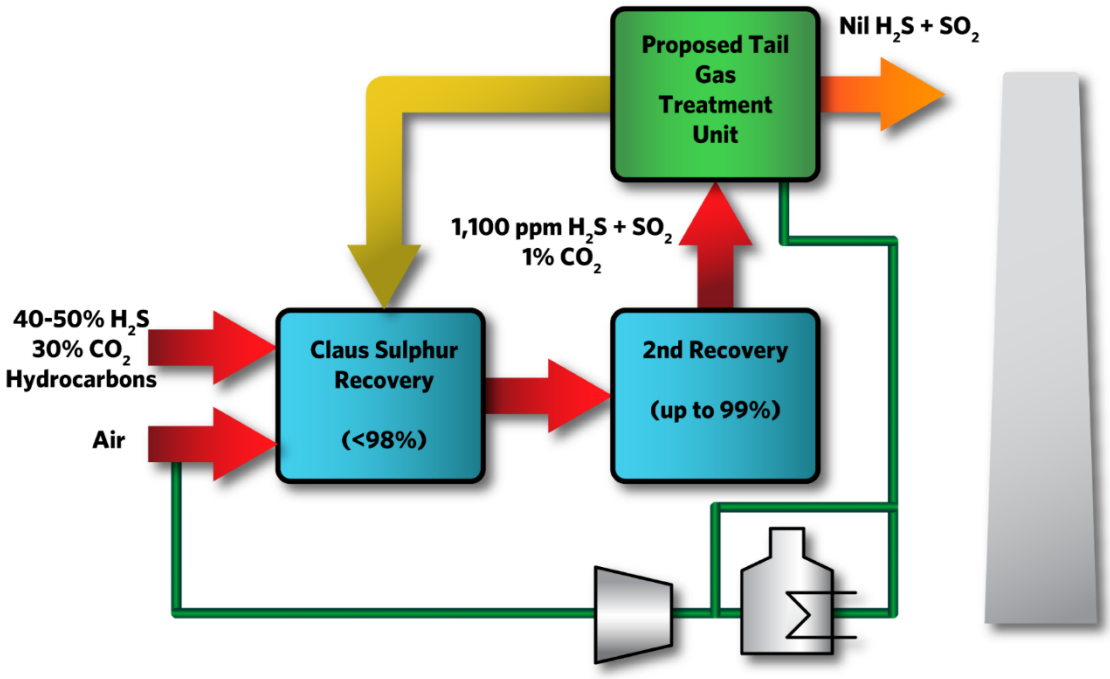

Figure 2.19/P-44 Integration of the proposed TGTU within the SRU

CHAPTER 3: KINETIC MODELING OF ADSORPTION PHENOMENA

3.1 INTRODUCTION

Kinetic modeling of adsorption phenomenon involves simultaneous solution of a number of differential balances depending on the model complexity and the number of relevant species. Analytical solutions are only obtained for cases involving linear adsorption isotherms rendering them of small practical interest [74]. The vast majority of cases require numerical solution techniques. A number of complexities arise when resolving to numerical techniques. For instance, explicit solution methods are by far computationally cheap but may suffer from serious numerical instabilities leading to unphysical results. Implicit methods on the other hand require inversion of large matrices rendering them computationally expensive. Finite element methods tend to lie in between both classes [74]. Within the context of adsorption system optimization, the complexity of the optimization process necessitates seeking the most reliable and computationally cheaper method.

The premise of this chapter is to critically review the various options available in adsorption modeling and chose the option that maximizes solver reliability while minimizing computational costs. I begin with a physical description of the adsorption problem and highlight the interacting phases. I then present the relevant model pertaining to the described physical image. Following, I review the main analytical solutions reported in literature. Next, I review reported numerical solution methods and compare their reliability and efficiency. Finally, a general comparison is laid; methods and models of

interest are chosen and tested with reported results. Integration of the method with the optimization algorithm described in Chapter 4 and their subsequent implementation is mentioned in Chapter 6.

3.2 MATHEMATICAL MODELING OF ADSORPTION PHENOMENON

3.2.1 THE PHYSICAL PICTURE

The envisioned physical model that gained wide consensus is depicted in Figure 3.1 [74]. The adsorption bed is comprised of a number of pellets each consisting of a conglomerate of sorbent phases bound together with a macroporous binder. Dispersion effects tend to disperse the adsorbing species in the axial direction within the bulk phase, thus resulting in earlier breakthrough. Mass transfer of adsorbing species to the interior of the sorbent pellet occurs via bulk diffusion through a thin film surrounding the sorbent pellet. Diffusion of species within the macroporous binder is commonly characterized as the reciprocal average of the Knudsen like diffusion (which accounts for diffusion where in the wall-molecules collisions dominate the process) and the bulk like diffusion (which accounts for diffusion where intermolecular collisions dominate the process). The latter is corrected for the binder porosity and tortuosity (see equation 3.25). Adsorption phenomenon is envisaged to occur at the external surface of the sorbent phase. The adsorption process is commonly assumed to be equilibrated. Following, the transfer of adsorbed species to the interior segment of the sorbent phase occurs via micropore diffusion. Bulk diffusion in the gas phase is usually in the order of 1 $cm^2 \cdot s^{-1}$ while in the liquid phase is in the order of 10^{-5} $cm^2 \cdot s^{-1}$ [75] Values of macroporous diffusion rates are functions of pore size, porosity and tortuosity and hence can vary substantially [75]. Microporous diffusion rates on the other hand can be strongly

affected by the concentration of adsorbate in addition to temperature. Typical values of microporous diffusion rates can vary substantially between 10^{-5} to 10^{-48} $cm^2 \cdot s^{-1}$ [75].

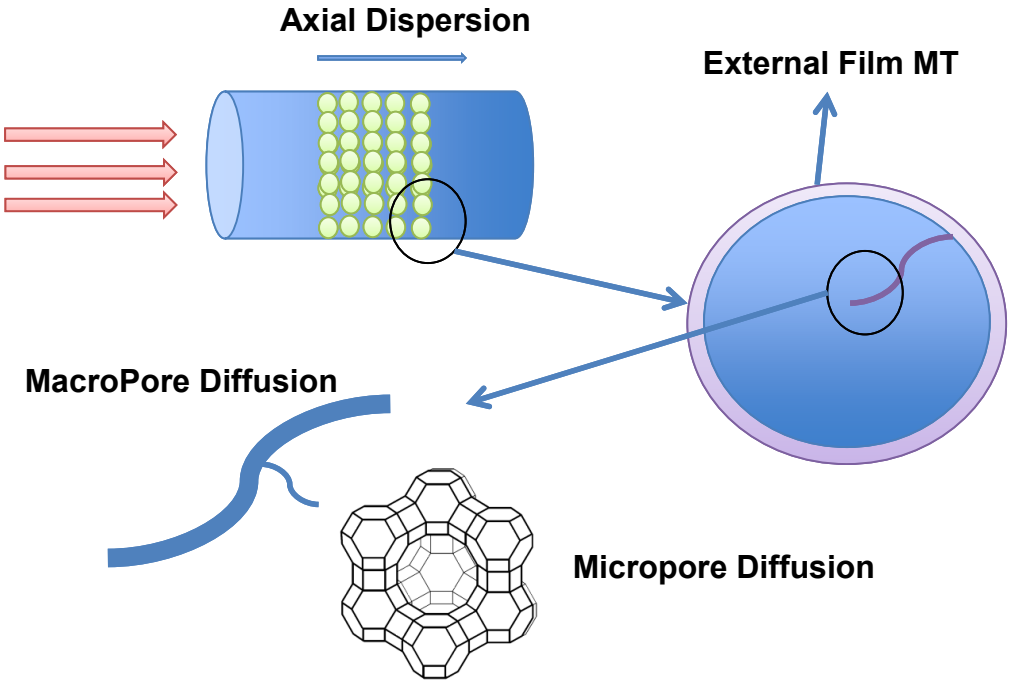

Figure 3.1/P-47 Pictorial illustration of the physical model of Adsorption. Crystal shown is for Faujasite obtained from [76].

The adsorption phenomenon is also envisioned as a series of concentration waves propagating through the bed [77]. When mass transfer resistances are absent and a uniform concentration feed is considered, the wave shape resembles a step function that propagates axially through the bed. Under mass transfer effects, the concentration profile loses its spatial uniformity and develops finite spatial gradients that decrease over time thus dispersing the concentration wave axially. Favorable adsorption isotherms tend to counteract mass transfer dispersive effects by having a compressive effect on the concentration wave [74]. When both effects balance each other, constant pattern waves develop [78, 79]. Those waves retain their shape and velocity as they elude from the bed.

Constant pattern waves have been observed on rare occasions and under controlled environments [78].

3.2.2 GOVERNING EQUATIONS

The mathematical model of the physical picture depicted in Figure 3.1 relies on a single mass balance per a component and a heat balance equation per modeled phase in addition to boundary conditions connecting the various phases at the interfaces. When transport rates are non-limiting within either the binder phase or the sorbent phase, a uniform concentration profile can be assumed thus removing one of the relevant balances. In most of the balances considered in literature single dimension spatial dependencies are employed [74].

In the bulk phase, the following equations describe the mass and energy balances assuming constant properties (from reference [74] with slight modifications):

$$\frac{\partial C_i}{\partial t}+\frac{\partial uC_i}{\partial z}+\frac{1-\varepsilon_b}{\varepsilon_b}k_{m,b,i}a_{b/P}\left(C_i-\overline{C}_i^{\,P}\right)=D_{z,i}\frac{\partial^2 C_i}{\partial z^2} \quad (3.1)$$

$$\frac{\partial T}{\partial t}+\frac{\partial uT}{\partial z}+\frac{1-\varepsilon_b}{\varepsilon_b}\frac{h_b a_{b/P}}{\rho_f C_b}\left(T-\overline{T}^{\,P}\right)=0 \quad (3.2)$$

where C_i is the species i concentration, u is the interstitial velocity of the bulk phase, ε_b is the bulk phase porosity, $k_{m,b}$ is the mass transfer constant describing the mass transfer rates across the interface between the bulk phase and the binder phase, $a_{b/P}$ is the surface area of the bulk-binder interface per unit volume, $\overline{C}_i^{\,P}$ is the average concentration of the species i within the binder phase, $D_{z,i}$ is the dispersion coefficient of species i, T is the temperature within the bulk phase, ρ_f is the density of the bulk phase, C_b is the constant pressure heat

capacity of the bulk phase, h_b is the heat transfer coefficient describing heat transfer across the bulk-binder interface, z is the axial dimension and t is time. Within the binder phase the following equations apply (from reference [74] modified to consider accumulation terms):

$$\frac{\partial C_i^P}{\partial t} + \frac{1-\varepsilon_P}{\varepsilon_P}\frac{\partial \overline{q}_i}{\partial t} = D_{P,i}\left(\frac{\partial^2 C_i^P}{\partial R^2} + \frac{2}{R}\frac{\partial C_i^P}{\partial R}\right) \quad (3.3)$$

$$\frac{\partial T^P}{\partial t} + \frac{1-\varepsilon_P}{\varepsilon_P}\frac{h_b a_{b/P}}{\rho_P C_P}\left(T^P - \overline{T}^S\right) = \frac{k_{H,p}}{\rho_P C_P}\left(\frac{\partial^2 T^P}{\partial R^2} + \frac{2}{R}\frac{\partial T^P}{\partial R}\right) \quad (3.4)$$

where C_i^P is the concentration of species i within the binder phase, ε_p is the binder phase porosity, $\overline{q}_i$ is the average concentration of the adsorbed species within the sorbent phase in units of moles per total volume, $D_{P,i}$ is the macroporous diffusion coefficient of species i, R is the radial spatial dimension assuming spherical pellets, T^P is the temperature within the binder phase, $a_{P/S}$ is the interfacial surface area per volume between the binder phase and the sorbent phase, h_P is the heat transfer coefficient describing heat exchange across the binder-sorbent interface, ρ_P is the density of the binder phase, C_P is the heat capacity of the binder phase, $\overline{T}^S$ is the average temperature within he sorbent phase., $k_{H,P}$ is the thermal conductivity of the binder. Within the sorbent phase, the following equations hold (from reference [74] modified to include accumulation terms):

$$\frac{\partial q_i}{\partial t} = D_{S,i}\left(\frac{\partial^2 q_i}{\partial r^2} + \frac{2}{r}\frac{\partial q_i}{\partial r}\right) \quad (3.5)$$

$$\frac{\partial T^S}{\partial t} = \frac{k_{H,S}}{\rho_S C_S}\left(\frac{\partial^2 T^S}{\partial r^2} + \frac{2}{r}\frac{\partial T^S}{\partial r}\right) + \frac{1}{\rho_S C_S}\sum_{i=1}^{Nu} H_{ads,i}\frac{\partial q_i}{\partial t} \quad (3.6)$$

where q_i is the adsorbed phase concentration, $D_{S,i}$ is the Micropore diffusion coefficient of species i, r is the radial spatial dimension assuming spherical sorbents, ρ_S and C_S are the sorbent density and heat capacity respectively, $k_{H,S}$ is the thermal conductivity of the sorbent phase, and H_{ads} is the species i adsorption enthalpy. The averaged properties used on the previous balances are obtained as follows (from reference [74] modified to accommodate employed symbols):

$$\bar{q}_i^S = \frac{3}{r_S^2}\int_0^{r_S} q_i r^2 dr \quad \bar{C}_i^P = \frac{3}{R_P^2}\int_0^{R_P} C_i R^2 dR \quad (3.7)$$

$$\bar{T}^S = \frac{3}{r_S^2}\int_0^{r_S} T^S r^2 dr \quad \bar{T}^P = \frac{3}{R_P^2}\int_0^{R_P} T^P R^2 dR \quad (3.8)$$

where r_s is the radius of the sorbent particle, and R_P is the radius of the pellet. Boundary conditions pertaining to the bulk phase are the following (from references [74, 80] modified to be in dimensional form):

$$C_i(t=0,z) = C_{i,ini} \quad C_i(t>0,z=0) = C_{i,o} \quad (3.09)\text{ a-c}$$

$$u_o C_{i,o} = u_o C_{i,ini} - D_{z,i}\left.\frac{\partial C_i}{\partial z}\right|_{z=0}$$

$$T(t=0,z) = T_{ini} \quad T(t>0,z=0) = T_o \quad (3.10)\text{ a,b}$$

where $C_{i,ini}$ is the initial concentration of species i within the bed's bulk phase, $C_{i,o}$ is the feed concentration of species i, u_o is the feed velocity, T_{ini} is the initial temperature of the bed's bulk phase, and T_o is the temperature of feed gas. Relevant boundary conditions for the pellet phase are the following (from reference [74] modified to accommodate the difference in symbols):

(3.11) a-c

$$C_i^P(t=0,R) = C_{i,ini}^P \quad C_i^P(t,R=R_P) = C_i$$
$$D_{P,i}\left.\frac{\partial C_i^P}{\partial R}\right|_{R=R_P} = k_{m,b,i}(C_i - C_i^P(t,R=R_P))$$
$$T_i^P(t=0,R) = T_{ini}^P \quad T_i^P(t,R=R_P) = T \qquad (3.12)\text{ a-c}$$
$$k_{H,P}\left.\frac{\partial T^P}{\partial R}\right|_{R=R_P} = h_P(T - T^P(t,R=R_P))$$

where $C_{i,ini}^P$ is the initial concentration of species within the pellet, T_{ini}^P is the initial pellet temperature. In the sorbent phase the relevant conditions are (from reference [74] modified to accommodate the difference in symbols):

$$q_i(t=0,r) = q_{i,ini} \quad q_i(t,r=r_s) = q_i^* \qquad (3.13)\text{ a-c}$$
$$D_{S,i}\left.\frac{\partial q_i}{\partial r}\right|_{r=r_s} = D_{P,i}\frac{\partial C_i^P}{\partial R}$$
$$T^S(t=0,r) = T_{ini}^S \quad T^S(t,r=r_S) = T^P \qquad (3.14)\text{ a-c}$$
$$k_{H,S}\left.\frac{\partial T^S}{\partial r}\right|_{r=r_s} = k_{H,P}\frac{\partial T^P}{\partial R}$$

where $q_{i,ini}$ is the initial adsorbed state concentration, q_i^* is the equilibrium adsorbed state concentration of species i and T_{ini}^S is the initial temperature within the crystals. Initial conditions of the bed are subject to the Cyclic Steady State (CSS) requirement[1]. Finally the adsorption equilibrium model is needed to form a complete set of equations:

$$q_i^* = f(T, C_i^P) \qquad (3.15)$$

[1] Refer to Chapter 4 for more information

The coming section describes the generally applied correlations for estimating mass transport parameters. For the sake of simplicity, isothermal condition is assumed through out the upcoming analysis. Such assumption is valid due to the scope of work considered i.e. removal of ppm level contaminants Claus tail gas.

3.2.3 MASS TRANSPORT CORRELATIONS

The model detailed in the previous section utilizes four parameters describing mass transfer rates. The bulk phase model employs a dispersion coefficient to describe axial dispersion effects and a mass transfer coefficient to describe mass transfer rate across the bulk-binder interface. The dispersion coefficient is obtained through the following correlation [81]:

$$\frac{\varepsilon_b D_{z,i}}{D_{m,i}} = 20 + 0.5 \cdot Sc_i \,\mathrm{Re} \qquad (3.16)$$

Where $D_{z,i}$ is the dispersion coefficient of species i, $D_{m,i}$ is the bulk phase molecular diffusion coefficient for species i and Sc_i is the Schmidt number of species i, and Re is the bulk phase Reynolds number. The mass transfer coefficient is obtained through the Ranz-Marshal correlation as follows [74]:

$$\frac{2k_{m,b,i}R_P}{D_{m,i}} = 2.0 + 0.6 \cdot Sc_i^{1/3}\,\mathrm{Re}^{1/2} \qquad (3.17)$$

Within the binder phase, macroporous diffusion coefficient is determined as the reciprocal average of the Knudsen diffusion coefficient and the molecular diffusion coefficient as follows:

$$\frac{1}{D_{P,i}} = \frac{\tau}{\varepsilon_P D_{m,i}} + \frac{1}{D_{k,i}} \quad (3.18)$$

$$D_{k,i} = 9.7 \times 10^3 r_{pore} \sqrt{\frac{T}{M}} \quad (3.19)$$

where τ is the binder tortosity, $D_{k,i}$ is the Knudsen diffusion coefficient in cm^2/s, r_{pore} is the pore radius measured in cm, T is the temperature in Kelvin, M is the species molecular weight. The microporous diffusion coefficient can be determined experimentally or through molecular simulations [82, 83]. Both methods suffer from deficiencies. Microporous diffusion rates obtained from different experimental methods can vary substantially. For instance, microporous diffusion coefficients for n-paraffins in ZSM-5 were found to be 10^{-11} $cm^2 \cdot s^{-1}$ via integral gravimetric uptake, 10^{-9} $cm^2 \cdot s^{-1}$ by NMR, and 10^{-6} $cm^2 \cdot s^{-1}$via large crystal permeation [74]. Ruthven et al. compared microporous diffusion rates for the same adsorbent but obtained from different sources and reported diffusivities varying by three orders of magnitude although using the same experimental technique [84]. The simulation method determination tends to be only applicable to crystalline sorbents under ideal conditions.

3.2.4 LINEAR DRIVING FORCE MODEL

We end this section with a description of the Linear Driving Force (LDF) approximation. When assuming equilibrium at the sorbent-binder interface, Glueckauf provided solutions for a variety of surface concentration profiles [74]. For the case when $D_p t/R_p^2 > 0.1$ and when the interior part of the sorbent is close to equilibrium the following expression holds:

$$\frac{\partial \bar{q}_i^S}{\partial t} = \frac{15}{R_P^2} D_{S,i} \left(q_i^* - \bar{q}_i \right) \quad (3.20)$$

Conditions for the viability of the LDF approximation require long adsorption times and/or fast microporous diffusion rates. For zeolites, time scales in excess of 100s are required while for activated carbon few seconds are sufficient to validate the LDF model [74]. The latter model has been used extensively in optimization literature in most cases without validating its conditions of viability. The full model generally employed in optimization literature which is based upon the linear driving force model is described herein. Assuming: 1) uniformity in velocity, concentration, and temperature profiles in the radial direction ,2) axial and temporal dependency of species concentration, temperature, pressure, and velocity ,3) ideal gas law, 4) extended Langmuir adsorption to describe mixture adsorption and 5) applicability of the linear driving force model [85], the governing Partial Differential Equations (PDE) are as follows:

1) Species *i* mass balance in the bulk phase:

$$\frac{\partial C_i}{\partial t} + \frac{\partial (uC_i)}{\partial z} + \frac{1-\varepsilon_b}{\varepsilon_b}\frac{\partial q_i}{\partial t} = D_{z,i}\frac{\partial^2 C_i}{\partial z^2} \qquad (3.21)$$

$$C_i\left(t=0, z \neq z_B\right) = C_{i,ini} \quad C_i\left(t, z=z_B\right) = C_{i,o}$$

$$uC_i\left(t, z=z_B\right) = uC_i^o - D_{z,i}\left.\frac{\partial C_i}{\partial z}\right|_{z=z_B}$$

where z_B is the limiting boundary, during adsorption $z_B = 0$ and during regeneration $z_B = L$.

2) The concentration is given by:

$$C_i = \frac{y_i P}{RT} \quad (3.22)$$

3) The dispersion coefficient is given by equation (3.16)

4) The linear driving force expression [85]:

$$\frac{\partial q_i}{\partial t} = k_{mass,i}\left(q_i^* - q_i\right) \qquad (3.23)$$

5) $k_{mass,i}$ is given by [85]:

$$k_{mass,i} = \left(\frac{q_i^*}{y_i k_{fi} \rho_f a_{b/P}} + \frac{R_P}{5 a_{b/P}} \left(\frac{1}{D_{P,i}} + \frac{\tau}{\varepsilon_P D_{m,i}} \right) \right)^{-1} \qquad (3.24)$$

$$k_{m,b,i} = \frac{0.357}{\varepsilon_b} \mathrm{Re}^{0.64}\, Sc_i^{033}\, \frac{D_{m,i}}{2R_P} \qquad (3.25)\ \text{a,b}$$

where the $k_{m,b,i}$ correlation is obtained from [74].

6) The following energy balances hold:

a) Energy balance in the bulk phase:

$$\frac{\partial T}{\partial t} + \frac{\partial (uT)}{\partial z} + h_b \frac{a_{b/P}}{C_b \rho_f} \left(\frac{1-\varepsilon_b}{\varepsilon_b} \right) \left(T - T^P\right) + \frac{4h_b}{D \varepsilon_b C_b \rho_f} \left(T - T_s\right) = 0 \qquad (3.26)$$

$$T\left(t, z = z_B\right) = T_o \quad T(t = 0, z) = T_{ini}$$

where T_s is the temperature of the vessel.

b) Energy balance of the solid sorbent:

$$\frac{\partial T_P}{\partial t} = h_s \frac{a_{b/P}}{C_P \rho_P} \left(T - T_P\right) - \frac{1}{\rho_P C_P} \sum_{i=1}^{Nu} H_{ads,i} \frac{\partial q_i}{\partial t} \qquad (3.27)$$

c) Energy balance of the wall steel:

$$\frac{\partial T_s}{\partial t} = h_b \frac{a_{b/P}}{C_{P,v}\rho_v}\left(T - T_s\right) \quad (3.28)$$

where $C_{P,v}$ is the heat capacity of the vessel and ρ_v is the vessel material density.

d) The heat transfer coefficient is given by [74]**:**

$$h_b = \frac{0.357}{\varepsilon_b}\mathrm{Re}^{0.64}\,\mathrm{Pr}^{033}\,\frac{k_{H,g}}{2R_P} \quad (3.29)$$

where Pr is the Prandtle number.

e) The pressure dependency on axial dimension is given by the Ergun equation:

$$\frac{\partial P}{\partial z} = \frac{150\mu\left(1-\varepsilon_b\right)^2 u}{4{R_P}^2{\varepsilon_b}^3} + \frac{1.75\rho_f\left(1-\varepsilon_b\right)u^2}{2R_P{\varepsilon_b}^3} \quad (3.30)$$

f) The equilibrium concentration is given by:

$$q_i^* = \frac{K_i \exp\left(\frac{H_{ads,i}}{R}\left(\frac{1}{T_P} - \frac{1}{T_{ref}}\right)\right) q_i^{sat} C_i}{1 + \sum_{i=1}^{Nu} K_i \exp\left(\frac{H_{ads,i}}{R}\left(\frac{1}{T_P} - \frac{1}{T_{ref}}\right)\right) C_i} \quad (3.31)$$

where q_i^{sat} is the saturation capacity of the adsorbent and Ki is the equilibrium constant for adsorption.

3.3 ANALYTICAL SOLUTIONS OF ADSORPTION MODELS

3.3.1 THE EQUILIBRIUM MODEL

Analytical solutions of the adsorption can be found for few limited cases. When mass transfer effects are neglected, adsorption model reduces to the equilibrium model on which the governing equation become:

$$\frac{\partial C_i}{\partial t} + u\frac{\partial C_i}{\partial z} + \frac{1-\varepsilon_b}{\varepsilon_b}\frac{\partial q_i}{\partial t} = 0 \qquad (3.32)$$

Analytical solutions for the equilibrium model are available for two cases: the linear adsorption case and the Langmuir adsorption case. For the linear adsorption case the outlet concentration profile resemble that of the inlet feed. The breakthrough time can be found for the case of uniform velocity as follows:

$$\frac{\partial q_i}{\partial t} = \sum_{j=1}^{Nu}\frac{\partial q_i}{\partial C_j}\frac{\partial C_j}{\partial t} = \frac{\partial q_i}{\partial C_i}\frac{\partial C_i}{\partial t} + \sum_{j=1, j\neq i}^{Nu}\frac{\partial q_i}{\partial C_j}\frac{\partial C_j}{\partial t} \qquad (3.33)$$

For the case of linear adsorption isotherm:

$$\sum_{j=1, j\neq i}^{Nu}\frac{\partial q_i}{\partial C_j}\frac{\partial C_j}{\partial t} = 0$$

$$\therefore \frac{\partial C_i}{\partial t} + u\frac{\partial C_i}{\partial z} + \frac{1-\varepsilon_b}{\varepsilon_b}\frac{\partial q_i}{\partial C_i}\frac{\partial C_i}{\partial t} = 0 \Rightarrow \frac{\partial C_i}{\partial t} = \frac{-u}{\left(1+\frac{1-\varepsilon_b}{\varepsilon_b}\frac{\partial q_i}{\partial C_i}\right)}\frac{\partial C_i}{\partial z} = u_c\frac{\partial C_i}{\partial z} \qquad (3.34)$$

where u_c is the velocity of the concentration front. Hence, the breakthrough time is given by:

$$t_{br,i} = \frac{L}{u}\left(1+\frac{1-\varepsilon_b}{\varepsilon_b}\frac{\partial q_i}{\partial C_i}\right) = \frac{L}{u}\left(1+\frac{1-\varepsilon_b}{\varepsilon_b}H_i\right) \qquad (3.35)$$

where $t_{br,i}$ is the breakthrough time of species i, L is the bed length, and H_i is Henry's constant. When mass transfer effects are considered, analytical solutions are only

obtainable for linear adsorption isotherms. Those are discussed in the coming section. For the case of when the extended Langmuir model holds, Rhee et al. reported an analytical solution, which is presented in chapter 4.

3.3.2 THE ROSEN MODEL

The Rosen model solves the governing equations presented in section 3.2.2 while excluding the sorbent phase [74]. The Rosen model assumes uniform velocity profile, isothermal bed operation, and linear adsorption isotherm for spherical pellets while considering mass transfer through the film surrounding the pellet and macroporous diffusion through the pellet. The exact solution for the Rosen model is:

$$\frac{C}{C_o} = \frac{1}{2} + \frac{2}{\pi}\int_0^{\infty} \exp(-\eta H_1^*(\lambda,\upsilon))\sin\left(\frac{2\lambda^2\tau}{15} - \eta H_2^*(\lambda,\upsilon)\right)\frac{d\lambda}{\lambda} \qquad (3.36)\text{ a-h}$$

$$\eta = \frac{15D_p}{R_P{}^2}\left(\frac{KL}{u}\right)\left(\frac{1-\varepsilon_b}{\varepsilon_b}\right)$$

$$\tau = \frac{15D_p}{R_P{}^2}\left(t - \frac{L}{u}\right)$$

$$\upsilon = \frac{D_P K}{k_{m,b} R_p}$$

$$H_1^*(\lambda,\upsilon) = \frac{H_1 + \upsilon\left(H_1{}^2 + H_2{}^2\right)}{\left(1+\upsilon H_1\right)^2 + \left(\upsilon H_2\right)^2}$$

$$H_2{}^*(\lambda,\upsilon) = \frac{H_2}{\left(1+\upsilon H_1\right)^2 + \left(\upsilon H_2\right)^2}$$

$$H_1 = \frac{\lambda\left[\sinh(2\lambda)+\sin(2\lambda)\right]}{\left[\cosh(2\lambda)-\cos(2\lambda)\right]} - 1$$

$$H_2 = \frac{\lambda\left[\sinh(2\lambda)-\sin(2\lambda)\right]}{\left[\cosh(2\lambda)-\cos(2\lambda)\right]}$$

Ralph Yang indicated that the integral of the Rosen model is slowly converging [74]. To bypass that hurdle, Thomas et al. obtained simplified solutions for the case when mass transfer film rates are neglected [74]. Such case is commonly experienced in gas adsorption processes. The Rosen model has been tested by Ruthven and Garg for the adsorption of several species over zeolites and was found to produce satisfactory results only when the adsorption follows Henry's law [83].

3.3.3 YANG'S MODEL

Cen and Yang presented a solution to the governing equations shown in section 3.3.3 for the case when isothermal condition holds, uniform velocity profiles, linear adsorption isotherms, and when the Glueckauf LDF approximation applies [86]. The solution provided is:

$$\frac{C}{C_o} = \exp\left(-\psi\left[\tau - x(1-\sigma)\right]\right)\sum_{j=0}^{\infty}\frac{\left[\psi(\tau - x)\right]^j}{(j+1)!}\sum_{i=0}^{j}\frac{(\sigma\psi x)^i}{i!} \qquad (3.37)\text{ a-e}$$

$$2\sigma = \frac{15D_{S,i}L}{{r_S}^2 u}\left[1 + \frac{1-\varepsilon_P}{\varepsilon_P}H_i + \frac{({D_{b,i}}/{{R_P}^2})({D_{S,i}}/{{r_S}^2})}{1+\frac{5D_{b,i}}{kR_P}}\right]$$

$$\psi = \frac{\frac{15({D_{b,i}}/{{R_P}^2})\left(\frac{L}{u}\right)^2}{1+\frac{5D_{b,i}}{kR_P}}}{\frac{2\sigma}{15({D_{S,i}}/{{r_S}^2})}}, \tau = \frac{ut}{L}, x = \frac{z}{L}$$

The above solution applies when 2σ is greater than 1, a condition that is practically satisfied [86]. Yang et al. have tested their solution in modeling experimental data of N_2 and CH_4 breakthroughs over Zeolite 5A and achieved a good agreement [86]. They also provided a

set of conditions for identifying the controlling mass transfer resistance [74]. Film mass transfer can be neglected if the following condition holds:

$$\frac{5D_{b,i}}{kR_P} >> 1 \qquad (3.38)$$

In addition microporous diffusion can be neglected if the following condition holds:

$$1+\frac{1-\varepsilon_P}{\varepsilon_P}H_i >> \frac{(D_{b,i}/R_P{}^2)}{(D_{S,i}/r_S{}^2)} \qquad (3.39)$$

If the opposite holds, then macropore binder diffusion can be neglected. The foregoing conditions allow significant simplifications of the governing model since in many cases a single mass transfer mode usually controls.

3.4 NUMERICAL METHODS IN ADSORPTION MODELING

The solutions presented thus far are of limited practical use due to the simplified adsorption models that were implemented. Still, they can be used as guidance for understanding the extent of mass transfer resistances and the qualitative behavior of real systems [78]. A wide spectrum of practical applications requires numerical solutions of the governing equations. A number of methods were used in literature for the numerical solution of adsorption models including finite differences methods, finite elements methods and method of lines [74]. Finite differences and finite elements gain the widest popularity due to their wide range of applicability. This section reviews both classes of methods and identifies their pros and cons. We begin by studying finite element methods and their application in

adsorption system modeling. Following, similar analysis is done to finite differences methods.

3.4.1 FINITE ELEMENTS METHODS

In the finite elements methods, the normalized space of the problem is broken down to a number of elements. Then, in each element a solution is proposed which matches the boundary conditions and satisfies the governing equations. Two methods are commonly used within the finite elements class; these are the Galerkin method [87] and the method of Orthogonal Collocations over Finite Elements (OCFE) [87] with the latter being the mostly applied in adsorption literature [80, 88, 89]. Any adsorption problem tackled with both methods can be posed in the following generic form:

$$L(y,x,c) - f = 0 \qquad (3.40)$$

Where L is a differential operator acting on a set of dependent variables (y), a set of independent variables (x), and a set of constants (c). Also f is a forcing function usually nonlinear. In the j^{th} element, a series solution is proposed of the following form:

$$y_j = F_o + \sum_{k=1}^{N} a_k F_k \qquad (3.41)$$

Where F_o is usually the initial boundary condition, F_k is a chosen function, and a_k is the preceding coefficient of the chosen function to be determined by satisfying the governing equations. Since the proposed solution is an approximate one, direct substitution into governing equations will result into a residue, which needs to be minimized by proper choice of the preceding coefficients. Rather than minimizing the residue function at a

specific point, the commonly applied method is to minimize the integral of the residue function normalized by a weighting function as follows:

$$R_N(y_j,x,c) = L(y_j,x,c) - f = 0$$

$$\int W_j(u) R_N(a_k,x,c) dV = 0, \quad j = 1,2,...,N \qquad (3.42)$$

Where R is the residue function and W is the weighing function In Galerkin's method, the weighing function is chosen to be:

$$W_j(x) = \frac{\partial y_N}{\partial a_k}$$

$$\int \frac{\partial y_N}{\partial a_k} R_N(a_k,x,c) dV = 0, \quad j = 1,2,...,N \qquad (3.43)$$

While in the orthogonal collocations method, the weighing function chosen is a Dirac delta function positioned at specific points called the collocation points as follows:

$$W_j(x) = \delta(x - x_j) \qquad (3.44)$$

Hence:

$$\int \delta(x - x_j) R_N(a_k,x,c) dV = 0, \quad j = 1,2,...,N \qquad (3.45)$$
$$\therefore R_N(a_k,x_j,c) = 0$$

Galerkin's method enjoys superior accuracy in emulating the actual solution if the integral can be evaluated analytically [87]. However, in many cases numerical evaluation of the integral is necessitated due to absence of an analytical expression as the solution This increases the computational burden and introduces sources of inaccuracies. Villadsen and Michelsen showed that the orthogonal collocations method could match the accuracy of

Galerkin's method if the collocation points are chosen such that they are the roots of a Legendre polynomial [87]. This allows bypassing the computational hurdle of evaluating the integral, while enjoying superior accuracy. For that reason the method of orthogonal collocations is used extensively in adsorption modeling literature.

The custom in adsorption modeling is to apply orthogonal collocations on the spatial derivatives, thus reducing the governing equations into a set of ordinary differential equations in time that can be solved numerically using the Runge Kutta 4^{th} order method or Euler's implicit method [88]. Early work utilizing the orthogonal collocation methods tested its accuracy in a number of applications such as ion exchange [89]. Due to the steepness of the concentration front, a large number of collocation points are required for accurate modeling. Kaczmarski and co-workers suggested the implementation of moving finite elements in order to minimize the number collocation points required and hence minimize the computational time [80]. They tested the moving elements concept on predicting the breakthrough curves of a mixture of xylenes (para- and ortho-), isopropyl benzene and ethyl benzene as compared to the fixed element approach. In one of the studied cases, the CPU time required for the moving elements method was thirty times lower than the one obtained by fixed elements approach, while retaining excellent agreement between both methods. The finite elements approach enjoys superior accuracy and stability. Still, the computational expense of the finite elements approach is far greater than the finite differences method. The next section reviews usage of finite differences methods in adsorption modeling.

3.4.2 FINITE DIFFERENCES METHODS

Finite differences methods enjoy the widest application in adsorption modeling due to their computational simplicity and long history of implementation [74]. The construction of the governing equations allows usage of explicit methods in their numerical solution. While their computational cost is cheap, explicit methods suffer from numerical instabilities and the existence numerical dispersion artifact intrinsic within them [90, 91]. Implicit methods are on the other hand numerical stable, however the computational cost of inverting the Jacobian matrix to simulate long adsorption cycles can be prohibitive.

Rouchon and co-workers have shown that a proper choice of the grid spacing and the differences scheme can not only insure numerical stability but also matches the numerical dispersion artifact with actual dispersion commonly experienced in real adsorption beds. The proposed scheme for an adsorption system experiencing only dispersion effects is as follows [90]:

$$\frac{C_{i,x-1}^{t+1} - C_{i,x-1}^{t}}{\Delta t_i} + u\frac{C_{i,x}^{t+1} - C_{i,x-1}^{t}}{\Delta x} + \frac{1-\varepsilon_b}{\varepsilon_b}\frac{q_{i,x-1}^{t+1} - q_{i,x-1}^{t}}{\Delta t} \qquad (3.46)$$

$$\Delta x = \frac{2D_{z,i}}{u}$$

$$\Delta t = \frac{1.5\Delta x}{u}\left(1 + H_i\right)$$

where Δx is the spatial grid spacing, and Δt is the temporal grid spacing both chosen for species having the lowest dispersion coefficient and Henry constant. Results obtained from that scheme lacked accuracy as compared to OCFE [91]. Kaczmarski and Antos modified the Rouchon scheme to include other all forms of mass transfer with the exception of micropore diffusion [92, 93]. They also modified the gridding scheme to increase the

accuracy and stability of the solution. Their suggested scheme in dimensionless form is the following:

$$C_{i,x}^{t+1}u_x^{t+1} = C_{i,x-1}^{t+1}u_{x-1}^{t+1} - \left(\frac{C_{i,x-1}^{t+1} - C_{i,x-1}^{t}}{\Delta t} + \frac{1-\varepsilon_b}{\varepsilon_b} \frac{St_i\left(C_{i,x-1}^{t+1} - C_{i,b,x-1}^{t+1}\right)}{1+Bi_i/5} \right) \qquad (3.47)\text{ a-g}$$

$$C_{i,P,x}^{t+1} = C_{i,x}^{t+1} - \frac{\varepsilon_p\left(C_{i,P,x}^{t+1} - C_{i,P,x}^{t}\right) + \left(1-\varepsilon_P\right)\left(q_{i,x}^{t+1} - q_{i,x}^{t}\right)}{St_i \Delta t}\left(1+\frac{Bi_i}{5}\right)$$

$$\frac{\partial u}{\partial x} = -u_o \frac{1-\varepsilon_b}{\varepsilon_b} \sum_{i=1}^{N} St_i \frac{\left(C_{i,x}^{t} - C_{i,P,x}^{t}\right)}{C_{i,o}}$$

$$St_i = \frac{k_{m,b} a_p L}{u}$$

$$Bi_i = \frac{k_{m,b} R_P}{D_{P,i}}$$

$$\Delta x_i = \frac{2D_{z,i}}{u}$$

$$\Delta t_i = \frac{1.5\Delta x_i}{u}\left(1+H_i\right)$$

where u_o is the entrance fluid velocity, $C_{i,o}$ is the feed concentration of species i, St_i is the species Stanton number, Bi_i is the species Biot number both defined above. Kaczmarksi scheme is partially implicit since it requires simultaneous solution of the binder phase concentration and the adsorbed phase concentration in each step of the explicit algorithm. Since the number of equations solved simultaneously is small (2N where N is the number of species) with the initial guess usually close to the final solution, Newton-Raphson algorithms are finely suited for such purpose. Kaczmarski and co-workers have benchmarked their algorithm with the accurate solution obtained from OCFE in a multitude of examples and obtained excellent agreement [92, 93]. One or two orders of magnitude reductions in computational time were obtained.

Considering the computational simplicity and cheapness of the Kaczmarski scheme in conjunction of its accuracy, the Kaczmarski scheme is the method of choice for adsorption bed modeling provided micropore diffusion is neglected. Implementation of the Kaczmarski algorithm for adsorption isotherms beyond the extended Langmuir isotherm was not considered till this date.

Implicit methods for the solution of the adsorption model were used in optimization literature [94]. The method of choice usually implemented is the central differences scheme since it provides quadratic convergence and insure numerical stability. Since optimization work requires spanning a large set of design variables where the numerical stability state of the method may drastically change, utilization of inherently stable methods, although expensive, is justified.

3.5 COMPARISONS & CONFIRMATION

The analysis laid thus far covered the general aspects of a selection of reported analytical solutions and numerical methods specifically used in adsorption modeling. As stated in Chapter 1 and Chapter 4, the optimization protocol followed herein is comprised of two steps[2] each involving different levels of modeling. In the first step, the basis for modeling should be an analytical equation corrected to account for mass transfer effect. In the second step, the employed has to be comprehensive to allow for full cycle modeling. This section discusses the selection of the appropriate models and methods pertaining to each step.

[2] Refer to Chapter 1 and Chapter 4 for more details.

Table 3.1 presents a summarized comparison among the methods studied. The equilibrium theory is well suited to be used as the skeleton solution for the purpose of optimization since it incorporates a realistic adsorption model unlike the other analytical methods. Moreover, it does not require numerical methods to evaluate the solutions thus insuring fast optimization of the adsorption model. Still, mass transfer effects have to be accounted for.

Category	Method	Pros	Cons
Analytical	Rosen model	Incorporate all elements of mass transfer with the exception of macroporous diffusion	Linear Isotherms
	Yang's Model	Incorporate all elements of mass transfer	Linear Isotherms
	Equilibrium Theory	Provides an analytical solution for the case of Langmuir adsorption	Do not include mass transfer
Numerical	LDF with Orthogonal Collocations [80]	Ensures numerical stability and high level of accuracy under a wide range of cases.	Computationally Expensive
	LDF with Implicit Finite Differences [94]	Ensures numerical stability and high level of accuracy under a wide range of cases.	Computationally Expensive
	Kaczmarski Explicit Method [92, 93]	Computationally cheap	Do not include micropore diffusion Only applicable for isothermal cases

Table 3.1/P-68 Comparison of analytical and numerical models for kinetic adsorption

In the work presented in this thesis, I have chosen the Kaczmarski algorithm as the basis for generating correlations for mass transfer efficiencies for the following reasons:

1) The algorithm is explicit in the most part hence hastening the modeling process.
2) Numerical stability of the algorithm was shown for a number of cases considered by Kaczmarski et al. [93].
3) The model incorporates all forms of mass transfer with the exception of micropore diffusion.
4) Incorporation of micropore diffusion into the model requires trustworthy estimates of the micropore diffusion coefficients. Those are clearly absent for a number of cases[3].

The conditions suggested by Yang (equations 3.39 and 3.40), although applicable to linear isotherms, can be used in determining the controlling resistance in mass transfer. I suggest employment of those conditions to determine cases were macroporous diffusion dominates. For those cases, a higher degree of confidence on the validity of the Kaczmarski algorithm is obtained. The Kaczmarski algorithm was implemented in a Matlab code and tested for several cases in order to assure the codes capability of reproducing Kaczmarski data in terms of breakthrough times. Breakthrough times were chosen as the performance benchmarks since the main objective of the modeling work is to determine the adequate design specifications that ensure a chosen breakthrough time is met. Variations in the fluid velocity due to adsorption of the analytes were not considered. Those variations were

[3] Refer to section 4.2.3

neglected since the scope of the thesis is focused on removal of ppm-level contaminants and inclusion of such variations would increase the computational expense of the code. The first case considered was reported by Kaczmarski et al. analyzing the breakthrough behavior of a pulsed feed of 1-Chlor-4-Nitrobenzol (analyte1) and 1-Chlor-2-Nitrobenzol (analyte 2) for chromatography purposes [93]. The case analyzes the influence of the Stanton number and the analytes concentration on the breakthrough time and the breakthrough curve shape. Model parameters are summarized in Table 3.2 [93].

Parameter	Analyte 1	Analyte 2
Saturation Cap. (mmol·g^{-1})	0.689	0.875
K (m^3·kmol^{-1})	4.56	4.56
Pulse Conc. (kmol·m^{-3})	0.127 (A) 0.063 (B)	0.127
Pulse end time (s)	54.8	54.8
Fluid velocity (m·s^{-1})	0.0011	
Bed Porosity	0.34	
Pellet porosity	0.52	
Stanton Number	1246 (A) & 312 (B)	
Sorbent density (kg·m^{-3})	1960	

Table 3.2/P-69 Model parameters for cases 1A and 1B

Table 3.3 summarizes the breakthrough times predicted by the Matlab code as compared to those reported by Kaczmarski and co-workers. Here the breakthrough time is defined as the time at which the concentration reaches ~25% of the maximum peak concentration. Kaczmarski breakthrough times were read from the figures provided in ref [93](Fig 1. for case 1 A and Fig 2. for case 1 B). Excellent agreement is established considering the minimal percentage deviation (<8%) although variations in fluid velocity were not taken into account. Figures 3.2 A and B depict the resulting breakthrough curves.

CASE No.	B.T.1 (Matlab)	B.T.1 (Kacz)	B.T.2 (Matlab)	B.T.2 (Kacz)
Case 1 A	1874	2000	2255	2450

Case 1 B	430	450	529	520

Table 3.3/P-70 Breakthrough times for the studied cases

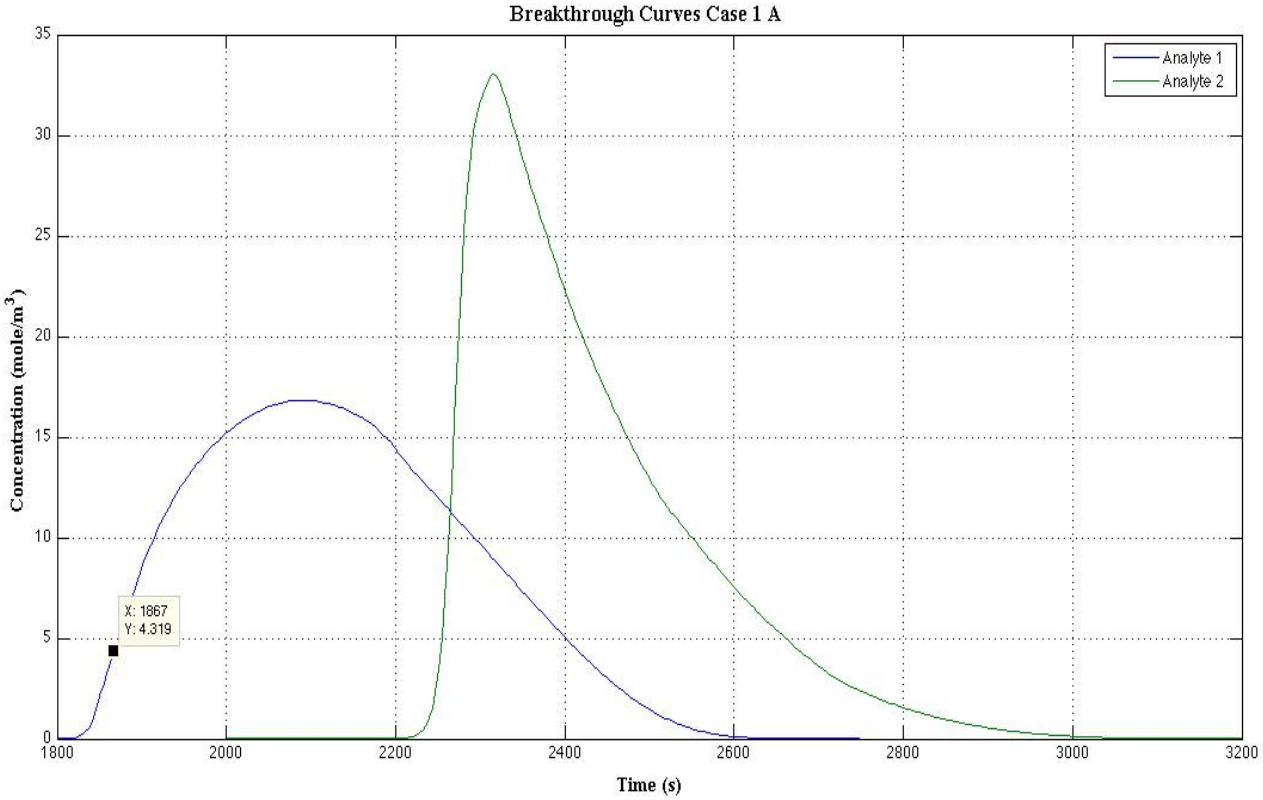

Figure 3.2A/P-71 Breakthrough curves for Case 1 A

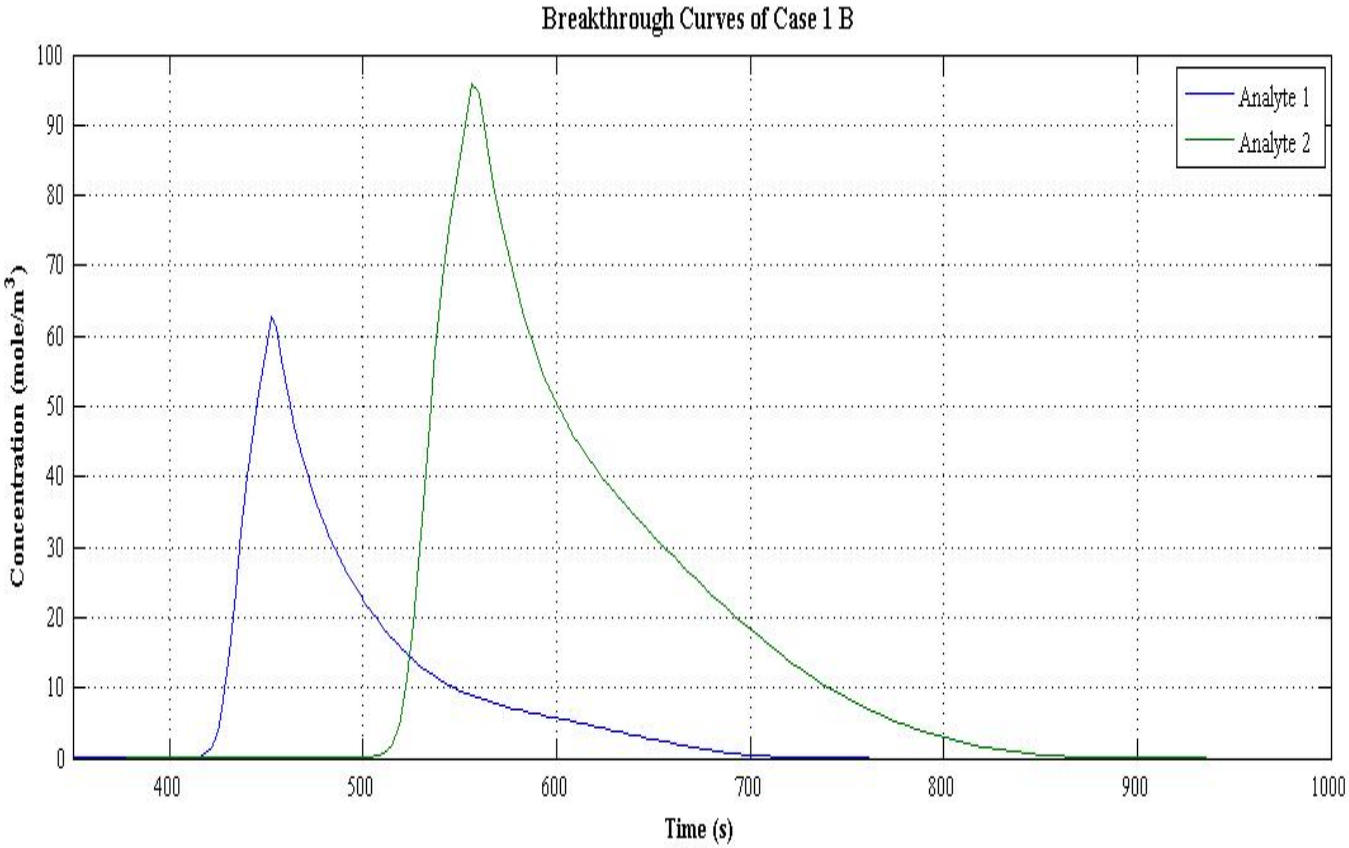

Figure 3.2B/P-72 Breakthrough curves for Case 1 B

For the second optimization step which involves the full scale modeling and optimization of the TSA system, I propose the use of the linear driving force based model. Numerically the model is highly stable and has been implemented in a multitude of optimization studies. Considering that full cycle modeling will demand a numerical technique which can withstand flow reversals, the orthogonal collocations approach is chosen as the numerical basis for the solution of the LDF model. The simulation is performed using gPROMS model builder. Further details on the solution method is presented in Chapter 6.

I end the chapter with a comparative study reflecting the close agreement between the Kaczmarski approach and the solution obtained via OCFE methods using gPROMS model builder. The model presented in section 3.2.4 is solved for the cases described in Chapter 6 using gPROMS process builder DASOLV time integration solver coupled with 40 elements based OCFE technique. The breakthrough times predicted by both methods are presented in Table 3.4 for a selection of bed lengths, diameters, and number of vessels[4]. The results clearly shows close agreement between both approaches predictions.

CASE No.	(L,D,N)	t_{br} (s)-Kacz	t_{br} (s)-OCFE	% difference
Case 1	(6.72,4.32,4)	106365	98235	8.3
Case 2	(7.56,4.01,4)	102018	98303	3.8
Case 3	(8.22,3.80,4)	99067	98193	0.9

Table 3.4/P-73 Breakthrough times predicted by the Kaczmarski approach compared to OCFE

[4] Refer to Chapter 6 for further details on the cases origin and associated results

3.6 CONCLUSIONS

In this chapter we have analyzed the adsorption modeling problem and a selection of the reported analytical solutions. Those solutions were found to be of limited practical use due to the assumption of linear adsorption isotherms or the negligence of mass transfer effects, hence reverting to numerical methods becomes necessary. Of the numerical techniques analyzed, the Kaczmarski semi-explicit finite differences algorithm coupled with the LDF full cycle model were found to be the most appropriate for the scope of thesis. The next chapter addresses optimization literature, presents the proposed model for the process design, and ends with the proposed global protocol for full process optimization.

CHAPTER 4: PROPOSED TGTU MODEL AND ITS OPTIMIZATION[5]

4.1 INTRODUCTION

Despite its industrial importance, optimization of Temperature Swing Adsorption (TSA) systems has not received much attention as confirmed by the limited number of studies conducted [85, 95]. The vast majority of adsorption studies were focused on Pressure Swing Adsorption (PSA) systems employing the black box approach, or the equation oriented approach to tackle the intricate coupling between the optimization algorithm and adsorption kinetic modeling as described in Chapter 1 [96]. The computational expense of such approaches tends to be high, hence limiting the number of probed design variables, objective functions, and imposed constraints. Moreover, the work detailed in those studies was far from being comprehensive due to the limited number of constraints included. For instance, pressure drop constraint and floor foot print constraint were never considered in all of those studies despite their indispensable importance in industrial applications. In addition, none of the conducted studies considered the net present value of costs as an objective despite the importance of the operating costs and sorbent replacement costs on the project standpoint. The premise of this chapter is to develop a comprehensive optimization algorithm that utilizes the equilibrium theory of Rhee et al [30] to bypass the need for solving coupled partial differential equations as described in chapter 1. First, we present a literature review on the topic of adsorption systems optimization. Following, I

[5] Significant segments of this chapter are published in (Al Wahedi et al., Chem Eng. Sci., 2014). License for reproduction in thesis was obtained under the number 3550021329985.

present in detail the suggested optimization algorithm. Implementation of the optimization algorithm is presented in chapter 6.

4.2 BACKGROUND ON ADSORPTION SYSTEMS OPTIMIZATION

4.2.1 SOLUTION APPROACHES

Optimization of adsorption systems can be decoupled into three levels of computational complexity as depicted in Figure 4.1. The inner level comprises the work required for modeling the detailed kinetics of adsorption within the bed. The intermediate level comprises the work required to achieve the Cyclic Steady State (CSS) condition, which specifies that conditions of the bed at the beginning of an adsorption cycle are equivalent to the same conditions at the beginning of the next adsorption cycle. The outer level comprises work related to conducting optimization of the adsorption system. Required computational time increases by orders of magnitude going from the inner level to the outer level. As I have indicated in Chapter 1, there are three approaches employed in literature for tackling the optimization problem: the black box approach, the equation oriented approach and the simultaneous tailoring approach depicted in Figure 4.1 [22]. In the black box approach, the optimizer supplies values of the design variables to a separate calculation algorithm i.e. the black box. Within the black box, kinetic modeling of adsorption is performed successively until the CSS condition is achieved. The black box generates values of the objective functions, relevant constraints, and sensitivity estimates which are in turn supplied to the optimizer.

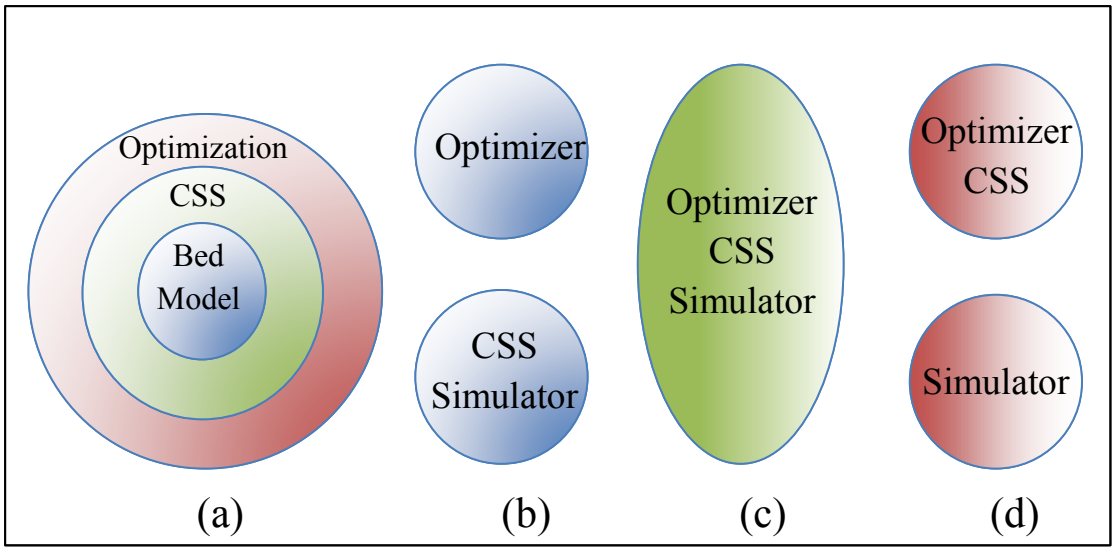

Figure 4.1/P-77 a) Schematic of the Optimization problem b) The black box approach c) The equation oriented approach d) the simultaneous tailoring approach

Based on those parameters, the optimizer generates a new set of design variables and supplies them to the black box. The cycle continues until an optimum point is realized. Since the optimization and simulation algorithms are separated, the black box approach can handle complex models without inducing numerical instabilities. Still, the computational cost of such approach is extremely high. For instance, Jiang et al. employed the black box approach for the study of six-step single bed vacuum swing adsorption on an i686 1 GHz CPU while considering six design variables and reported a computational time of 455 hours [22]. In order to minimize the computational time extensively, Kapoor and Yang generated a polynomial expression of the objective function in terms of design variables via running extensive simulations using the black box approach and regressing the resulting data [97]. This scheme allowed usage of simple optimization algorithms since a direct functional relationship exists.

In the equation-oriented approach, the simulation models' Partial Differential Equations (PDEs) are discretized using single-dimension discretization (SD) [27], complete discretization (CD) [94], or orthogonal collocations (OC) [23] in order to reduce the PDEs system into sets of algebraic or ordinary differential equations. Those sets are compiled with the optimization problem equations and solved simultaneously using the optimizer engine. Boundary conditions and CSS conditions are used as constraints. This approach reduces the computational time significantly and allows for increasing the complexity of the optimization problem. Still, when this approach is used in considering complex kinetic model it often fails due to the numerical instabilities in the Newton algorithm or due to accumulation of errors [22]. The kinetic model widely employed consists of a single mass balance equation per component, an energy balance, and an explicit adsorption model such as the extended Langmuir model. Mass transfer effects are usually expressed using the Linear Driving Force model (LDF).

The latter model is only applicable for long adsorption times under certain constraints (Refer to Chapter 3 for more details). In the equation-oriented approach, computational cost is a strong function of the complexity of the studied optimization problem. For instance, Sankararao et al considered multi-objective functions optimization of a PSA system and reported a computational time of 720 hrs using a Pentium 4 2.99 GHz CPU [28]. For a simpler case, Ko and co-workers considered single objective optimization of a PSA system for the purpose of CO_2 sequestration and reported a computational of 5273 CPU s using a dual core 800 GHz machine [26]. The major cause for the length of the computational times is the size of the studied system, which typically consists of thousands of equations that are solved simultaneously.

In order to decrease the required computational time, Agarwal et al. suggested a reduced order method as to replace the thousands of equations that describe the problem with a smaller set of equations while capturing accurately all the details [21]. For that purpose, the method of snap shots was used. In this method, the complete model simulations are conducted with various sets of design variables spanning the range of interest in the optimization problem. The results obtained from those snap shots are regressed into a reduced model that reproduces the model outcomes. The reduced model is then used in the optimization process. Utilizing this method, Agarwal and co-workers reported a computation time of 195 CPU seconds while considering four design variables for a single bed PSA system [21].

The main disadvantage of this method lies in the time required for the generation of the reduced model. Moreover, obtaining accurate results outside the studied range of design variables is not guaranteed. Jiang and co-workers were the first to propose the simultaneous tailoring approach in order to accommodate more complicated models as compared to the equation-oriented approach while reducing the required computational time [22]. In this approach, the solution work is distributed between an optimization algorithm and a simulation algorithm. Unlike the black box approach, CSS conditions are added as constraints to the optimization algorithm. In other words, while the optimizer is seeking an optimum solution it also tries to satisfy the CSS condition, hence the first convergence point that satisfy the CSS condition is also an optimum one. Since this method is an intermediate combination between the equation oriented approach and the black box approach, the computational cost is expected to be intermediate i.e. between hundreds of hours to few hours. For instance, Jiang et al. considered the optimization of a five bed PSA

system using effectively five design variables in a 2.4 GHz CPU and reported a computational time of 50-200 hours [27]. In another study by Jiang and co-workers considered single bed dual sorbent PSA optimization using an i686 1 GHz machine and reported a computational time of 69 hours as compared to 691 hours using the black box approach.

4.2.2 MODIFICATIONS ON SOLUTION STEPS

I have indicated previously that the solution of the optimization problem consists of three sub-algorithms: the optimization algorithm, CSS achievement algorithm and the bed-modeling algorithm. This section presents a literature background on specific studies done on those algorithms.

Adsorption kinetic modeling is commonly done using a single mass balance equation per component, an energy balance and the extended Langmuir adsorption model. The linear driving force approximation is used to model mass transfer processes. Cruz, Magalhaes and Mendes investigated a number of alterations to bed modeling [23]. A dual phase mass balance model was employed. Five different mass transfer approximations were investigated. Those are: LDF assuming negligible accumulation within the intraparticle (LDF1), LDF assuming instantaneous equilibrium between the gas phases residing within interparticle and intraparticle (LDF2), Linear driving force dusty gas model (LDF3), a differential mass balance within the particle phase assuming instantaneous equilibrium with the intraparticle gas phase (DM), and the dusty gas model (DS) [98]. Two adsorption models were investigated: the Langmuir-Freundlich model (LF) and the Ideal Adsorption Solution theory (IAS). Comparing the studied mass transfer models in oxygen separation

from air, LDF2, LDF3 and DM models resulted in practically similar oxygen recoveries while LDF1 deviated within 15% from the others. The authors recommended employment of LDF2 model while suggesting further experimental investigations to ascertain the accuracy of the studied adsorption models.

CSS confirmation algorithms are the major bottleneck in modeling complicated systems. The common approach for ensuring achievement of CSS involves successive substitution of end bed conditions of a cycle into the initial bed conditions of the subsequent cycle. Such approach simulates reality and hence is numerically stable [23]. However, for certain cases the number of cycles required to achieve CSS can be numerous and for cases described by highly nonlinear adsorption models the number can reach tens of thousands of iterations [99]. Croft and LeVan suggested a Newton based approach that utilizes the bed end conditions and sensitivity estimates to predict the subsequent cycle initial conditions [100]. Computational time per iteration is increased by 200 times compared to the successive substitution, however the number of cycles is reduced from 30000 to 15 only. This increase in computational time per iteration is due to the expensive calculation procedure for the estimating the Jacobian matrix. Overall, this leads to computational savings. To address the computational problems of the Newton approach, Kvamsdal and Hertzberg studied other approaches for hastening achievement of CSS and compared them to the successive substitution approach [99]. Those are: the Aitken update method [99], Muller's secant method [99], and Broyden update method [101]. Aitken's and Muller's methods are computationally cheap and require calculation of at least three cycles via successive substitution. Broyden's update method of estimating the Jacobian involves a seven-step calculation procedure.

All those methods result into substantial reduction in the number of cycles processed before achieving CSS, however numerical stability of those methods is strongly system dependent. This issue was addressed by Ding and LeVan and was solved by suggesting a hybrid algorithm composed of four methods for hastening the process of Jacobian evaluation through a hybrid Newton-Broyden approach complemented with an iterative secant approach, dynamic grid allocation for sensitivity estimations, and dynamic specification of integration error tolerances [102]. The algorithm estimates the error of each iteration and decides which method to employ depending on the convergence rate and the error trends. The authors claim two to three orders of magnitude savings in computational time required to reach CSS. Based on those studies, we suggest implementing the successive substitution technique if the number of cycles required for achieving CSS is less than 50 otherwise, the Ding and LeVan hybrid approach should be used. This is driven by the fact that the hybrid approach computational cost per iteration is about an order of magnitude higher than the successive substitution method.

Moving the focus towards optimization methods and algorithms, one of the early studies on PSA optimization addressed a Mixed Integer Non-Linear Programming (MINLP) model [103]. The model considered was of simplistic nature due to the weak computational resources available at that time. Later studies employed the reduced space Successive Quadratic Programming (r-SQP), which stands as the most widely used technique [22, 26, 27, 104]. The technique is favored due to the low functional evaluations required to reach the optima given a close initial guess.

More advanced methods were considered lately such as the simulated annealing method [28], and the genetic evolution method [105] due to the availability of multi-core

processers. With the exception of the genetic evolution method, to our best knowledge no study has considered multi-start algorithms despite the strong nonlinearly of the models employed. This strong nonlinearity raises the chances of having multiple local optima that have to be spanned in order to raise the confidence on the closeness of the obtained optima to the global one.

Efforts to simplify the optimization process considered reduced order modeling [21], objective function regression in terms of design variables [97], and dimensional analysis reduction [23, 24]. The latter reduce the model equations into dimensionless form. All the design variables are compiled into a fewer group of dimensionless numbers thus easing the optimization process. Due to the strong nonlinearity of the adsorption problem, I emphasize the need for employing multi-start algorithms.

4.2.3 THE SUGGESTED APPROACH

The literature presented thus far reflects the level of complexity of adsorption system optimization. Efforts of increasing the complexity of the kinetic model are compensated by sacrifices in the optimization problem and vice versa. Realistic simulations require incorporation of higher levels of model complexity, realistic optimization problems along with multi-start optimization algorithms. Personal computational resources may fail to address all these issues with relatively low computational times.

As described in Chapter 1, I propose a two-step optimization approach. In the first step, the PDE governing model is recast into an analytical nonlinear by using the equilibrium solution proposed by Rhee et al. as the solution skeleton [30]. An efficiency factor is then introduced in order to account for mass transfer effects. The recast model is incorporated

into the full scale Mixed Integer Non-Linear Problem which includes the objective function, constraints not relevant to the PDE model, and the mixed integer decision variables.

Then, the formulated MINLP is solved using Sequential Quadratic Programming approach coupled with a multi-start engine. In the second step, the parent PDE model is incorporated into a nonlinear optimization problem and solved using the equation oriented approach. The new optimization problem is simplified in two levels. The decision variables now include only continuous variables. All the integer decision variables assumes the fixed values obtained from the first step solution. Moreover, a single point optimization is done wherein the optimal solution of the first step is used as the initial guess.

4.3 TGTU NONLINEAR MODEL

Herein I present the detailed derivation of the TGTU model for process concepts 1 and 2 (refer to Chapter 2 for more information on the process flow diagram). The TGTU of process concept 2 is comprised of two subsystems: the hydrogenation subsystem and the TSA subsystem. The hydrogenation subsystem is comprised of the feed gas heater, the hydrogenation reactor, and the water cooler. The TSA subsystem is comprised of the adsorbent vessels, the regeneration gas compressor and the regeneration gas heater. Process concept 1 only incorporates the TSA subsystem. Starting with the TSA subsystem and for the nonlinear algebraic version of the model, the cycle's steps are incorporated from the work of Wunder et al. for natural gas driers design [73]. While adsorption is envisaged to occur isothermally with a uniform velocity, regeneration is envisaged to simulate a phase change on which the adsorbed species transforms to the gas phase isothermally at an

experimentally determined regeneration temperature. Hence, the cycle for nonlinear algebraic version of the model is envisaged to occur via the following steps:

1) Adsorption Step: Isothermal adsorption of sulfur species from a uniform flow of Claus tail gas stream.
2) Heating Step: Heating the sorbent bed and vessel to an experimentally determined temperature via passage of hot regeneration gas and supplying the adsorption heat required to remove the adsorbed phases.
3) Regeneration Step: Regeneration by passing hot regeneration gas across the bed until complete bed regeneration to fresh conditions is achieved. This step is assumed to occur isothermally.
4) Cooling Step: Cooling down of bed back to operating temperature using the cold purge stream.

Hence, the total required time for regeneration comprises the time required for heating the bed to the experimentally determined regeneration temperature, the time required for complete removal of adsorbed species as determined by the model implemented and finally the time required to cool down the bed to the operating temperature. This approach is expected to provide a conservative design of the TSA unit since a segment of regeneration occurs during the heating step. The following major assumptions are invoked in this analysis in order to facilitate the initial step of the optimization:

1) Extended Langmuir adsorption model to be applicable. This assumption is invoked in order to allow for the use of the Rhee et al. analytical solution [30].
2) Ideal gas conditions prevail during all steps.

3) Isothermal conditions to hold during adsorption and regeneration steps. For adsorption this assumption is valid considering that the Claus tail gas stream is dilute.
4) Uniform axial and radial velocity profiles.
5) Bed regeneration is done to fresh conditions defined by reaching an adsorbed phase concentration of 10^{-6} of the saturation value. This assumption eliminates the need to consider the achievement of the cyclic steady state condition.
6) Equivalency of the number of vessels undergoing adsorption to those undergoing regeneration.
7) Feed gas distributes evenly among vessels.
8) Sorbent adsorption characteristics deterioration upon successive regeneration cycles is neglected throughout the life cycle of the sorbent.
9) Adiabatic compression of regeneration gas.
10) During bed heating and cooling, the outlet temperature of the regeneration gas remains constant and is equivalent to the weighted average of the bed initial temperature and the regeneration gas inlet temperature.

As stated previously, the Net Present Worth of costs (NPW) is chosen as the economic criterion. It is comprised of three cost elements: the Total Capital Investment (TCI), operating costs (OPEX), and bed replacement costs (BED). The latter is ensued upon the full exhaustion of the bed after a certain number of regeneration cycles. The mathematical form of the NPW function is:

$$NPW = \underbrace{6\cdot\left(P_{bed}+P_{hyd}+P_{v}+P_{FHR}+P_{FHF}+P_{v,hyd}+P_{CB}+P_{HxC}\right)}_{TCI}+$$

$$\underbrace{\sum_{j=1}^{J}\left(P_{W}+P_{HDF}+P_{HDR}+P_{CW}\right)\left(\frac{1+r_{\inf}}{1+r_{dis}}\right)^{j}}_{OPEX} \quad \underbrace{+\sum_{j=n^{*}f}^{J}\left(P_{bed}\right)\left(\frac{1+r_{\inf}}{1+r_{dis}}\right)^{j}}_{BED}$$

where,

$$P_{bed}=P_{ads}\cdot N\cdot\rho_{c}\left(1-\varepsilon_{b}\right)\pi\frac{D^{2}}{4}L \quad P_{hyd}=P_{cat}\cdot\rho_{cat}\frac{3600}{SV}\cdot Q_{F}\left(1-\varepsilon_{b}\right)$$

$$P_{v}=N\cdot\left(-2.59\cdot10^{-3}\left[\rho_{v}\left(\pi D\left(L+L_{\text{int}}\right)th+\pi D^{2}th\right)\right]^{2}+3.99\cdot\left[\rho_{v}\left(\pi D\left(L+L_{\text{int}}\right)th+\pi D^{2}th\right)\right]+56540\right)\cdot\frac{CECPI_{current}}{CEPCI_{2007}}$$

$$P_{v,hyd}=N\cdot\left(-2.59\cdot10^{-3}\left[\rho_{v}\left(\pi D\left(L_{hyd}+L_{\text{int}}\right)th+\pi D^{2}th\right)\right]^{2}+3.99\cdot\left[\rho_{v}\left(\pi D\left(L_{hyd}+L_{\text{int}}\right)th+\pi D^{2}th\right)\right]+56540\right)\cdot\frac{CECPI_{current}}{CEPCI_{2007}}$$

$$L_{hyd}=\frac{3600}{SV}\cdot\frac{Q_{F}}{\frac{\pi}{4}D^{2}}$$

$$P_{FHR}=\frac{CEPCI_{current}}{CEPCI_{2002}}10^{0.752\cdot\log\left(HDR\right)+2.29} \quad P_{FHF}=\frac{CEPCI_{current}}{CEPCI_{2002}}10^{0.752\cdot\log\left(HDF\right)+2.29}$$

$$P_{CB}=\frac{CEPCI_{current}}{CEPCI_{2002}}10^{0.67\cdot\log\left(Q_{reg}\right)+4.65} \quad P_{HxC}=\frac{CEPCI_{current}}{CEPCI_{2002}}10^{0.11(\log_{10}A_{c})^{2}+0.17\log_{10}A_{c}+3.3}$$

$$P_{HDR}=P_{FG}\cdot HDR=P_{FG}\cdot N_{1}\int_{T_{2}}^{T_{regG}}C_{regG,P}dT \quad P_{HDF}=P_{FG}\cdot HDF=P_{FG}\cdot F\int_{T_{feed}}^{T_{hyd}}C_{F,P}dT$$

$$P_{W}=\frac{5P_{EP}B}{2\eta}N_{1}RT_{envi}\left(\left(\frac{P_{2}}{P_{envi}}\right)^{\frac{\frac{C_{regG,P}}{C_{regG,V}}-1}{\frac{C_{regG,P}}{C_{regG,V}}}}-1\right) \quad P_{CW}=Q_{CW}\cdot24\cdot365\cdot P_{Water}$$

Detailed derivation is presented in section 4.3.1. Seven design/decision variables are selected: bed length, bed diameter, regeneration gas flow, regeneration gas temperature, number of vessels and adsorption cycle time. Six operational constraints including pressure drop, footprint, breakthrough time, and total cycle time balance, should be satisfied. Tables 4.1 and 4.2 present the design variables and the operational constraints of the model.

Design Variable	Description	Lower Bound	Upper Bound
L	Bed Length (m)	0	70
D	Bed Diameter (m)	0	5

N	Number of Vessels an integer variable	2	40
N_1	Molar flow of regeneration gas (kmol·h^{-1})	0	3500
T_{regG}	Temperature of regeneration gas (^oC)	T_{reg}	550
t_{reg}	Allocated time for regeneration (h)	0	70
t_{ads}	Adsorption cycle time (h)	0	70

Table 4.1/P-88 List of selected design variables

The breakthrough and minimum regeneration times ($t_{ads,max}$ and $t_{reg,min}$) are determined by solving the governing partial differential equations of the adsorption and regeneration steps or via the correcting the equilibrium analytical solution for mass transfer effects. $t_{ads,max}$ is defined as the time at which the exit concentration of the contaminant species reaches 5% of the inlet concentration while $t_{reg,min}$ is defined as the time at which the contaminant concentration as an adsorbed phase reaches 10^{-6} of the sorbent saturation capacity.

Constraint Description	Mathematical Expression
Assigned adsorption cycle time should not exceed the breakthrough time predicted via simulation given L, D and N.	$t_{ads} \leq t_{ads,\max}$
Total regeneration time should not exceed the assigned adsorption cycle time.	$t_{ads} \geq t_{reg} + t_{heating} + t_{cooling}$

Assigned regeneration cycle should exceed the minimum required time for regeneration predicted via simulations given L,D, N and N_1	$t_{reg} \geq t_{reg,\min}$
TSA unit pressure drop should not exceed the maximum allowable pressure drop ΔP_{max}	$\Delta_{\max} \geq L\left(\frac{150\mu(1-\varepsilon_b)^2 U_f}{4R_P{}^2\varepsilon_b{}^3} + \frac{1.75\rho_f(1-\varepsilon_b)U_f{}^2}{2R_P\varepsilon_b{}^3}\right)$
TSA unit foot print should not exceed the maximum allowable foot print A_{max}	$A_{\max} \geq \frac{7}{4}(D+2th)^2\left(1+\frac{3N}{2}\right)$
Interstitial velocity of treated gas should not exceed 80% of the bed minimum fluidization velocity.	$U_f \leq 6\cdot 10^{-4} g \frac{4R_P{}^2}{\mu}(\rho_C - \rho)$

Table 4.2/P-89 Description of employed constraints of the model

4.3.1 OBJECTIVE FUNCTION CONSTRUCTION

The NPW function employed comprises of three cost elements; the total capital cost, bed replacement cost, and the operating costs. The hydrogenation reactor, sorbent bed, steel vessels, a centrifugal blower and fired gas heaters for the feed gas and the regeneration gas and the water cooler for the feed gas prior to the introduction to the TSA system. The total capital investment is obtained by summing all the equipment costs and multiplying the sum by 6. Operating costs comprise of the cost of electrical power supply to the centrifugal blower, fuel gas consumption in the fired heaters, and water cooling flow rate needed. Other operating cost elements such as personnel salaries, auxiliary systems requirements, e.g. lube oil system for the centrifugal blower and instrument air costs, are neglected. The NPW function is computed for a project life cycle of 30 years assuming that all prices escalate at a fixed inflation rate.

I start with the TSA subsystem first. Given a set of decision variables, the total capital investment is computed based on the major equipment costs, which are computed as follows:

1) Sorbent bed cost is computed via equation (4.1):

$$P_{bed} = P_{ads} \cdot N \cdot \rho_c (1 - \varepsilon_b) \pi \frac{D^2}{4} L \quad (4.1)$$

where P_{bed} is the total cost of all sorbent beds in \$, P_{ads} is the current price of the sorbent in $\$\cdot kg^{-1}$, N is the number of vessels, ρ_c is the solid density of the sorbent in $kg \cdot m^{-3}$, D is the bed diameter in m, L is the bed length in m and ε_b is the bed porosity.

2) Vessels costs are computed from the mass of the vessel via a cost correlation generated by regressing data obtained from [106] for carbon steel vessels:

$$m_v = \rho_v \left(\pi D (L + L_{\text{int}}) th + \pi D^2 th \right) \quad (4.2)$$

$$P_v = N \cdot \left(-2.59 \cdot 10^{-5} m_v^2 + 3.99 \cdot m_v + 56540 \right) \cdot \frac{CECPI_{current}}{CEPCI_{2007}} \quad (4.3)$$

where m_v is the mass of each vessel in kg, ρ_v is the steel density in $kg \cdot m^{-3}$, L_{int} is the allocated length for bed internals in m, *th* is the vessel thickness in m, and P_v is the total current cost of all vessels in \$. CEPCI is the chemical engineering plant cost index and the subscript denotes the year at which the index is computed.

3) Centrifugal blower cost is computed from the regeneration gas volumetric flowrate, which is computed via the ideal gas law. The blower cost correlation is a logarithmic fit of a graphical cost correlation found in [107]:

$$P_{CB} = \frac{CEPCI_{current}}{CEPCI_{2002}} 10^{0.67 \cdot \log(Q_{reg}) + 4.65} \quad (4.4)$$

where P_{CB} is the current cost of the centrifugal blower in \$, Q_{reg} is the volumetric flow rate of regeneration gas in $m^3 \cdot s^{-1}$. Outlet temperature from the blower (T_2) is calculated assuming adiabatic compression:

$$T_2 = T_{envi} \left(\frac{P_2}{P_{envi}} \right)^{\frac{\frac{C_{regG,P}}{C_{regG,V}} - 1}{\frac{C_{regG,P}}{C_{regG,V}}}} \quad (4.5)$$

where T_{envi} centrifugal blower regeneration gas inlet temperature in K, P_2 outlet pressure of the regeneration gas in Pa, P_{envi} inlet pressure of the regeneration gas in Pa, $C_{regG,P}$ constant pressure heat capacity of the regeneration gas in $J \cdot K^{-1} \cdot mol^{-1}$, $C_{regG,V}$ constant volume heat capacity of the regeneration gas in $J \cdot K^{-1} \cdot mol^{-1}$.

4) Regeneration gas heater cost is calculated based on its heating duty. The cost correlation was obtained via a logarithmic fit of the graphical cost correlation for direct fired heaters from [107]. The heating duty is computed through an energy balance done on the fired heater system:

$$P_{FH} = \frac{CEPCI_{current}}{CEPCI_{2002}} 10^{0.752 \cdot \log(HDR) + 2.29} \quad (4.6)$$

$$HDR = N_1 \int_{T_2}^{T_{regG}} C_{regG,P} dT \quad (4.7)$$

where, P_{FH} is the current cost of the fired gas heaters in \$, HDR is the heating duty of the regeneration gas fired heater in W, $T_{reg,G}$ is the regeneration gas temperature in ^oC.

The hydrogenation subsystem consists of the following equipment:

1) The feed gas heater is sized using the same approach of the of the regeneration gas heater. However, the target temperature is set to 240^{o}C in line with the existing low temperature hydrogenation technologies [108]. Moreover, the heat capacity of the feed gas is used instead.
2) The hydrogenation reactor is sized based on reported space velocity for the commercial hydrogenation reactor. Reported space velocities range from 2000 h^{-1} to 3000 h^{-1} [108]. The reactor diameter is assumed to match that of the adsorbent vessels. Hence, the required catalyst mass can be computed as follows:

$$m_{hyd} = \rho_{cat} \frac{3600}{SV} \cdot Q_F (1 - \varepsilon_b) \quad (4.8)$$

where ρ_{cat} is the catalyst density in kg·m^{-3}, SV is the space velocity in h^{-1}, and Q_F is the feed gas volumetric flow rate in $m^3 \cdot s^{-1}$. Reactor vessel size is given by:

$$m_{v,hyd} = \rho_v \left(\pi D \left(L_{hyd} + L_{\text{int}} \right) th + \pi D^2 th \right) \quad (4.9)$$

where L_{hyd} is the reactor bed length in m which can be computed as follows:

$$L_{hyd} = \frac{3600}{SV} \cdot \frac{Q_F}{\frac{\pi}{4} D^2} \quad (4.10)$$

Finally, the total hydrogenation reactor cost, i.e. catalyst cost and the vessel cost are computed using the formulae for the adsorbent bed however taking into account the hydrogenation catalyst price.

3) The water gas cooler is assumed to be a standard shell and tube heat exchanger. The area of heat exchange is determined as follows:

$$A_c = \frac{F \int_{T_{outg}}^{T_{hyd}} C_{F,P} dT}{U \Delta T_{LM}} \quad (4.11)$$

where, A_c is the area of heat exchange in m^2, F is the feed gas flow here in $mol \cdot s^{-1}$, $C_{F,P}$ is the mole based heat capacity function for the feed gas $J \cdot mol^{-1} \cdot K^{-1}$, T_{hyd} is the hydrogenation reactor temperature, T_{outg} is the outlet temperature, U is the overall heat transfer coefficient, and ΔT_{LM} is the log mean temperature difference between the cooling fluid and the feed gas. The water cooler cost is computed using the following formula obtained via:

$$P_{HxC} = \frac{CEPCI_{current}}{CEPCI_{2002}} 10^{0.1104 (\log_{10} A_c)^2 + 0.1685 \log_{10} A_c + 3.2958} \quad (4.12)$$

The operating costs on the other hand comprise of the fuel gas cost for the feed gas heater and the regeneration gas heater, the cooling water for the water gas cooler and the electrical power cost. The fuel gas cost is computed based on the heating duty. The fuel gas unit cost is usually expressed in $ per energy units. The electrical power cost is computed from the power demand of the centrifugal blower as follows:

$$P_W = \frac{5 P_{EP} B}{2\eta} N_1 R T_{envi} \left(\left(\frac{P_2}{P_{envi}} \right)^{\frac{\frac{C_{regG,P}}{C_{regG,V}} - 1}{\frac{C_{regG,P}}{C_{regG,V}}}} - 1 \right) \quad (4.13)$$

where, P_W is the electrical power cost in $\$ \cdot yr^{--1}$, P_{EP} is the electrical power cost in $\$ \cdot kWh^{-1}$, B is a conversion factor, and η is the adiabatic efficiency of the blower. The cooling water used is a 5 bar boiler feed water at saturated conditions. This grade of water is chosen

as to utilize the heat of water vaporization generate 5 bar steam. No credit is given for the steam produced. The following correlation was generated via HYSYS^{TM} simulator as to compute the required volumetric flow rate of cooling water given a targeted feed gas outlet temperature:

$$Q_{cool} = -5.14 \cdot 10^{-2} T_{outg} + 12.36 \quad (4.14)$$

where Q_{cool} is the volumetric flow rate of cooling water in $m^3 \cdot h^{-1}$ required to achieve the targeted temperature of the feed gas (T_{outg} in ^oC). Finally the bed replacement cost is computed from P_{bed} escalated at a fixed inflation rate.

The NPW function is evaluated from the yearly cash flow statement for a nominal plant life of 30 years. The function is expressed by equation (4.15):

$$NPW = 6 \cdot \underbrace{\left(P_{bed} + P_{hyd} + P_{v,bed} + P_{FHR} + P_{FHF} + P_{v,hyd} + P_{CB} + P_{HxC}\right)}_{MEC} + \underbrace{\sum_{j=1}^{J} \left(P_W + P_{HDF} + P_{HDR} + P_{CW}\right)\left(\frac{1+r_{inf}}{1+r_{dis}}\right)^j}_{OPEX} \quad \underbrace{+ \sum_{j=n^*f}^{J} \left(P_{bed}\right)\left(\frac{1+r_{inf}}{1+r_{dis}}\right)^j}_{BED} \quad (4.15)$$

where j is the year index extending from year zero to year 30; the end of the plant life, n is a dummy integer, r_{inf} inflation rate, r_{dis} discounting rate employed in the NPW calculation and f is the period of bed replacement in years. Herein, the factor 6 is the Lang factor used in estimating the TCI given the MEC.

4.3.2 DESIGN CONSTRAINTS

Six design constraints are employed in the proposed algorithm. Three of which are governed by the dynamics of the adsorption process, a constraint for pressure drop in order

to accommodate the low available pressure in the Claus unit, a constraint for plant foot print to accommodate for limited spaces in offshore locations, and a constraint to prevent bed fluidization during adsorption. Herein I describe those constraints in detail:

1) Maximum adsorption time: The maximum adsorption time possible is governed by the dynamics of the adsorption process. The constraint is obtained by correcting the breakthrough time computed from the equilibrium model [30] using an efficiency factor. For fresh bed adsorption, the constraint is expressed as follows:

$$t_{ads} \le \frac{\zeta_{ads} L}{\left(U_f / \varepsilon_b\right)} \left(1 + \frac{1-\varepsilon_b}{\varepsilon_b} \rho_C \frac{\min\left(K_{i,ads} \cdot q_{si}\right)}{1 + \sum_{i=1}^{n} K_i C_i^F} \right) \quad (4.16)$$

where, ζ_{ads} is the efficiency factor accounting for mass transfer effects during adsorption, U_f is the feed gas velocity in $m \cdot s^{-1}$, $K_{i,ads}$ is the adsorption equilibrium constant for species i in $m^3 \cdot mole^{-1}$, q_{si} the saturation capacity of species i in $mole \cdot kg^{-1}$ both computed at the adsorption condition, and C_i^F is the feed molar concentration of species i in $mole \cdot m^{-3}$.

2) Cycle time balance: This constraint establishes an upper bound on the total regeneration time of the cycle. As stated previously, the regeneration cycle consists of three steps; heating, regeneration, and cooling. The combined time of those steps should not exceed the selected adsorption time. The required times of bed heating and cooling are computed from an energy balance done on the bed. The regeneration time is an assigned decision variable. Equations (4.17) and (4.18) for

bed heating and equations (4.19) and (4.20) for bed cooling while inequality (4.21) is expressed through the constraint:

$$Heat = \frac{N}{2}\left(m_c \int_{T_{opt}}^{T_{regen}} C_c dT + m_v \int_{T_{opt}}^{T_{regen}} C_v dT + t_{ads} \cdot F \sum_{i=1}^{n} y_i H_{ads,i} \right) \quad (4.17)$$

$$t_{Heating} = \frac{Heat}{N_1 \int_{T_{regG}}^{T_{reg,out}} C_{regG,P} dT} \quad (4.18)$$

$$Cooling = \frac{N}{2}\left(m_c \int_{T_{regen}}^{T_{opt}} C_c dT + m_v \int_{T_{regen}}^{T_{opt}} C_v dT \right) \quad (4.19)$$

$$t_{Cooling} = \frac{Cooling}{N_1 \int_{T_{reg,out}}^{T_2} C_{regG,P} dT} \quad (4.20)$$

$$t_{ads} \geq t_{reg} + t_{Heating} + t_{Cooling} \quad (4.21)$$

where, C_c is the heat capacity temperature function of the sorbent in $J \cdot kg^{-1} \cdot {}^oC^{-1}$, C_v is the heat capacity temperature function of the vessel in $J \cdot kg^{-1} \cdot {}^oC^{-1}$, F is the molar flow of feed gas in each vessel in $kmole \cdot h^{-1}$, y_i is the mole fraction is species i in the feed gas, $H_{ads,i}$ the heat of adsorption of species i in J $mole^{-1}$, and $T_{reg,out}$ is the outlet temperature of the regeneration gas during the cooling step and the heating step computed as per assumption 10 (in ^oC).

3) Minimum regeneration time: This constraint establishes a lower bound on the allocated regeneration time. As stated previously, the analytical solution of the equilibrium model is used in conjunction with an efficiency correction factor to

obtain a realistic estimate of the time required for complete bed regeneration. The inequality below expresses the constraint:

$$t_{reg} \geq \frac{L}{\zeta_{reg}\left(U_{reg}/\varepsilon_b\right)}\left(1+\frac{1-\varepsilon_b}{\varepsilon_b}\rho_C \max\left(K_{i,reg}\cdot q_{si}\right)\right) \quad (4.22)$$

where ζ_{reg} is the efficiency factor accounting for mass transfer effects during regeneration, U_{reg} is the regeneration gas velocity in $m\cdot s^{-1}$, $K_{i,reg}$ is the adsorption equilibrium constant for species i in $m^3\cdot mole^{-1}$, q_{si} the saturation capacity of species i in $mole\cdot kg^{-1}$ both computed at the regeneration conditions.

4) Pressure drop constraint: the maximum permitted pressure drop is dictated by the conditions of the feed gas eluding from the Claus unit. The feed gas should have sufficient pressure at the exit of the bed in order to allow safe emission to environment. The pressure drop constraint is computed via the Ergun equation as expressed below:

$$\Delta_{max} \geq L\left(\frac{150\mu\left(1-\varepsilon_b\right)^2 U_f}{4{R_p}^2{\varepsilon_b}^3}+\frac{1.75\rho_f\left(1-\varepsilon_b\right){U_f}^2}{2R_P{\varepsilon_b}^3}\right) \quad (4.23)$$

Where Δ_{max} is the maximum allowable pressure drop in Pa, μ is the feed gas viscosity in $Pa\cdot s$, ρ_f is the feed gas mass density in $kg\cdot m^{-3}$, U_f is the feed gas superficial velocity in $m\cdot s^{-1}$, R_p is the sorbent pellet radius in m.

5) Plant maximum footprint: due to the limit space available in offshore sites, this constraint has been incorporated in order to expand the applicability of the algorithm. The plant footprint is computed based upon the schematic depicted in

Figure 4.2 while excluding the foot prints of the blower and the heater. The governing constraint is:

$$A_{FP} = W_{FP} \cdot L_{FP}$$

$$L_{FP} = \frac{(D + 2th)}{2}(1 + 3N) \quad W_{FP} = \frac{7}{2}(D + 2th)$$

$$A_{\max} \geq \frac{7}{4}(D + 2th)^2\left(1 + \frac{3N}{2}\right) \quad (4.24)$$

6) Bed fluidization constraint: This constraint establishes an upper bound on the velocity of the feed gas in order to prevent the occurrence of bed fluidization. The fluidization velocity constraint is expressed as follows [109]:

$$U_f \leq 6 \cdot 10^{-4} g \cdot \frac{4R_p^{\ 2}}{\mu}(\rho_c - \rho_f) \quad (4.25)$$

Given the objective function and the imposed constraints, the symbolic statement of the optimization problem is the following:

$$NPW = 6 \cdot \underbrace{\left(P_{bed} + P_{hyd} + P_{v,bed} + P_{FHR} + P_{FHF} + P_{v,hyd} + P_{CB} + P_{HxC}\right)}_{MEC} +$$

$$\underbrace{\sum_{j=1}^{J}\left(P_W + P_{HDF} + P_{HDR} + P_{CW}\right)\left(\frac{1+r_{\inf}}{1+r_{dis}}\right)^j}_{OPEX} \quad \underbrace{+ \sum_{j=n*f}^{J}\left(P_{bed}\right)\left(\frac{1+r_{\inf}}{1+r_{dis}}\right)^j}_{BED}$$

s.t.

$$t_{ads} \le \frac{\zeta_{ads} L}{\left(U_f / \varepsilon_b\right)}\left(1 + \frac{1-\varepsilon_b}{\varepsilon_b}\rho_C \frac{\min\left(K_{i,ads} \cdot q_{si}\right)}{1 + \sum_{i=1}^{n} K_i C_i^F}\right)$$

$$t_{reg} \ge \frac{L}{\zeta_{reg}\left(U_{reg} / \varepsilon_b\right)}\left(1 + \frac{1-\varepsilon_b}{\varepsilon_b}\rho_C \max\left(K_{i,reg} \cdot q_{si}\right)\right)$$

$$t_{ads} \ge t_{reg} + t_{Heating} + t_{Cooling}$$

$$\Delta_{\max} \ge L\left(\frac{150\mu(1-\varepsilon_b)^2}{{D_P}^2 {\varepsilon_b}^3} + \frac{1.75\rho_f(1-\varepsilon_b){U_f}^2}{D_P {\varepsilon_b}^3}\right)$$

$$A_{\max} \ge \frac{7}{4}(D + 2th)^2\left(1 + \frac{3N}{2}\right)$$

$$U_f \le 6 \cdot 10^{-4} g \frac{{D_P}^2}{\mu}\left(\rho_C - \rho\right)$$

$$LB \le \left[L, N, D, N_1, t_{reg}, T_{reg,g}, f\right] \le UB$$

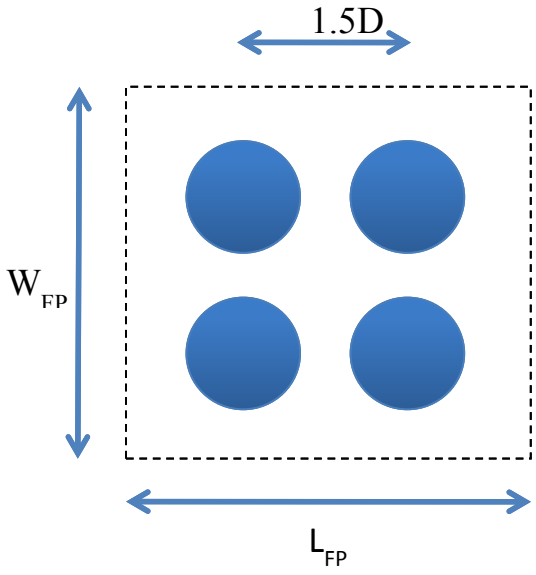

Figure 4.2/P-99 TSA unit Layout

4.4 SENSITIVITY STUDIES

In this section I present sensitivity case studies done on the process concept 1 (TSA only) for a hypothetical adsorbent in order to probe the NPW solution space given the governing constraints. The conclusions of this study can be extrapolated to process concept 2 (TSA+hydrogenation) since the hydrogenation system cost is governed only by the feed conditions rendering it a fixed cost. The case studies are done on two industrial plants: GASCO and ADGAS. The GASCO plant relies on the conventional Claus process coupled with Cold Bed Adsorption technology (CBA) for a targeted SC of 99.5% [110]. The ADGAS plant relies on the conventional Claus coupled with Super Claus technology for a targeted SC of 99.5% [111]. For both cases, the TSA unit is proposed to be situated downstream the secondary recovery step (i.e. CBA for GASCO and Super Claus for ADGAS).

4.4.1 SENSTIVITY STUDY INPUTS

Table 4.3 summarizes GASCO and ADGAS feed streams composition, flows and conditions. I have chosen the sorbent zeolite based CuX reported by Kumar et al. as the basis for the hypothetical sorbent [15]. The sorbent is known to be sensitive towards presence of CO, hence I assumed the feed stream to be CO free. Langmuir adsorption parameters for CuX towards H_2S adsorption were obtained from Kumar et al. [15]. Adsorption parameters of H_2S including heat of adsorption, equilibrium constant, and saturation capacity were all obtained from the results reported by Tsapatsis et al. [112]. Due to absence of adsorption data regarding SO_2 in CuX, this works assumes sorbent adsorption behavior of SO_2 can be modeled as that reported for zeolite 5A [113].

Experimental regeneration temperature for the sorbent is obtained from results in [112]. Porosity of the sorbent pellet was assumed to be 0.4 while the pellet diameter was assumed to be 1 cm. Bulk phase diffusion coefficients of the species of interest were determined using the Chapman–Enskog correlation assuming binary system with N_2 being the bulk phase. Sorbent solid density was assumed to be 1700 kg m^{-3}. Heat capacity of the sorbent was assumed to replicate that of NaX [114]. Finally, sorbent replacement is assumed to occur every 1000 regenerations. During that period the sorbent is assumed to retain its adsorption qualities. A summary of sorbent specifications is presented in Table 4.4.

Category	GASCO	ADGAS
Temperature (°C)	127	150
Pressure (kPa)	130	130
Molar Flow (kmol h^{-1})	3451	3313
Hydrogen (kmol h^{-1})	52.39	24.51
Water (kmol h^{-1})	1094.56	905.8
CO (kmol h^{-1})	30.12	38.10
N_2 (kmol h^{-1})	1689.39	1636.3
O_2 (kmol h^{-1})	0	16.57
CO_2 (kmol h^{-1})	580.6	658.6
H_2S (kmol h^{-1})	2.27	0.66
SO_2 (kmol h^{-1})	1.14	2.98
COS (kmol h^{-1})	0.2	0.33
CS_2 (kmol h^{-1})	0.61	0.33
Molecular Weight (kg $kmol^{-1}$)	27.18	28.18

Table 4.3/P-101 ADGAS and GASCO Feed streams conditions

Category	Value

Regeneration Temperature (°C)	**500**
Pellet Porosity	**0.4**
Pellet diameter (cm)	**1.0**
Saturation Capacity of H_2S (mmol g^{-1})	**1.2**
Saturation Capacity of SO_2 (mmol g^{-1})	**1.0**
Saturation Capacity of CO (mmol g^{-1})	**1.0**
Equilibrium Constant H_2S (m^3 total volume mol^{-1})	**483**
Equilibrium Constant SO_2 (m^3 total volume mol^{-1})	**115**
Equilibrium Constant CO (m^3 total volume mol^{-1})	**4.94**
Adsorption Enthalpy H_2S (kJ mol^{-1})	**60**
Adsorption Enthalpy SO_2 (kJ mol^{-1})	**40**
Adsorption Enthalpy CO (kJ mol^{-1})	**65**
Bulk phase diffusion coefficient H_2S (cm^2 s^{-1})	**0.82**
Bulk phase diffusion coefficient SO_2 (cm^2 s^{-1})	**0.63**
Bulk phase diffusion coefficient CO (cm^2 s^{-1})	**0.97**
Sorbent Heat Capacity (kJ mol^{-1} K^{-1})	**-6.077 +251.68 (T/1000)-324.8 $(T/1000)^2$**

Table 4.4/P-102 Sorbent Specifications

As for feed gas specifications, gas density was obtained by assuming ideal gas behavior. Feed gas viscosity determined via ASPEN HYSYS™ simulator prediction. Bed porosity was assumed to be 0.4. Vessels material of construction is carbon steel. Heat capacity and density of carbon steel were obtained from reference [115] & [116] respectively. Thickness of the vessel is assumed to be 5 cm. Extra length allocated for vessel internals was set at 2 meters. Air is used as the regeneration medium. Heat capacity of air is obtained from reference [116].

Category	GASCO	ADGAS
Feed gas density (kmol m^{-3})	0.041	0.039
Feed gas viscosity (cP)	0.018	0.0198
Steel Density (kg m^{-3})	7850	7850
Vessel Thickness (cm)	5.0	5.0
Bed porosity	0.4	0.4
Extra length for internals (m)	2.0	2.0
Heat Capacity of Steel (kJ mol^{-1} K^{-1})	18.43 +24.64 (T/1000)-8.91 $(T/1000)^2$	
Heat Capacity of Air (kJ mol^{-1} $^oC^{-1}$)	28.94+0.415T	

Table 4.5/P-103 Auxiliary Specifications

As for the economical inputs, adsorbent price is computed based on reported price of AgX adsorbent from reference [117] taking into consideration the difference in bulk price of copper to that of silver. Utility prices were obtained from GASCO [110]. Chemical Engineering Plant Cost Index used to correlate prices to year 2011 is 555.5 [118]. In the computation of the NPW, a discounting rate of 8% is assumed. The inflation rate of prices was assumed to be 5%. Table 4.6 summarizes economical inputs of the model.

Category	Value
CEPCI	555.5
Sorbent Price ($/ton)	1700
Electrical Power Cost ($/MWh)	30
Fuel Gas Cost ($/GCal)	4.36
Inflation rate	5%
Discounting rate	8%
Project life (yrs)	30

Table 4.6/P-103 Economic parameters

Finally, the correlations for the efficiency factors are discussed. Adsorption and regeneration efficiency factors were obtained by regressing kinetic simulation predictions of the breakthrough and regeneration times covering three decision variables; L, D, and N for adsorption and L, D, and N_1 for regeneration via the Kaczmarski et al. described earlier

[92]. Adsorption breakthrough time is defined as the time when the bed outlet contaminant concentration reaches 5% of its inlet value. A bed is considered fully regenerated if the contaminants adsorbed phase concentration reached 10^{-6} of its saturation value.

Breakthrough times obtained from the simulation were collected for bed length ranges from 5 to 15 m, for bed diameter ranges from 1 to 5 m and for a total number of vessels ranging from 4 to 16. Regeneration times were obtained for the same length and diameter ranges, however regeneration gas flows ranging from 200 to 800 kmol h^{-1} per vessel were considered. Those ranges were found to encompass the space of optimum decisions variables for the cases understudy. A total number of data points regressed were 57 for the adsorption step and 90 for the regeneration step. The following empirical form was found to provide good fit of the obtained data for adsorption and regeneration cases:

$$\zeta = \frac{X_1 \left(\frac{L}{D} \right)^{X_2}}{X_3 \, \mathrm{Re}^{X_4} \, Sc^{X_5} + X_6} \quad (4.26)$$

Where X_1, X_2 , X_3, X_4 , X_5, X_6 are fitting parameters, Re is the particle based Reynolds number and Sc is the limiting species based Schmidt number. The limiting species is defined as the species which breakthroughs first and complete removal of it is achieved last. Table 4.7 presents the fitting parameters and their confidence intervals for both ADGAS and GASCO cases for the controlling species; sulfur dioxide. Overall, average correlation deviations from simulated times falls below 10%. Figures 4.3 and 4.4 depicts error contour maps for GASCO and ADGAS expressed in LD (Length times Diameter) vs. Particle Reynolds number form. Higher error values are observed in regions of lower LD values and high Reynolds numbers.

	GASCO		ADGAS	
Parameter	**Adsorption**	**Regeneration**	**Adsorption**	**Regeneration**
M	13.806 ± 0.83	16.264±7.5E-04	13.348± 9.6E-02	16.286 ± 7.5E-05
x	0.144 ± 3.6 E-03	0.238± 3.55E-05	0.135± 5.5E-03	0.232 ± 3.5E-06
C	$1.4 \cdot 10^{-03}$ ± 4.7E-04	$4.0 \cdot 10^{-03}$ ± 6.1E-07	$1.9 \cdot 10^{-03}$ ± 6.9E-05	$3.8 \cdot 10^{-03}$ ± 5.9E-08
y	1.112 ± 3.9E-02	0.919 ± 2.37E-05	1.063 ± 4.4E-03	0.934 ± 2.4E-06
z	-0.107 ±0.24	-2.578 ± 1.55E-04	-0.282 ± 2.6E-02	-2.45 ± 1.6E-05
N	24.137 ±1.5	19.020 ± 1.15E-03	24.966 ± 0.21	18.879 ±1.1E-04
Average Error	8.6%	7.1%	8.5%	7.0%

Table 4.7/P-105 Fitting parameters for mass transfer efficiency factors

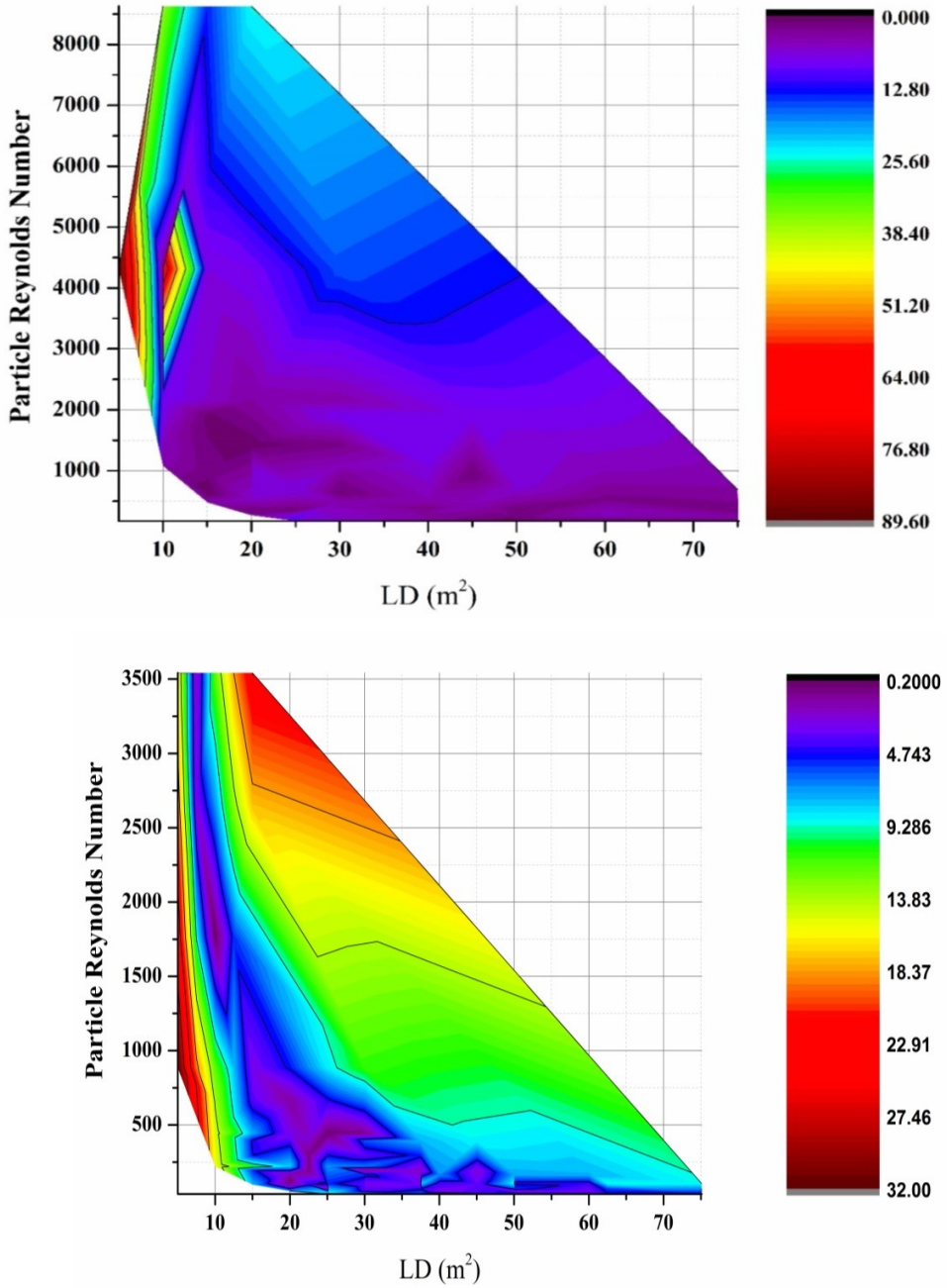

Figure 4.3/P-106 Error maps: GASCO Adsorption Cases (top) & GASCO Regeneration Cases (bottom)

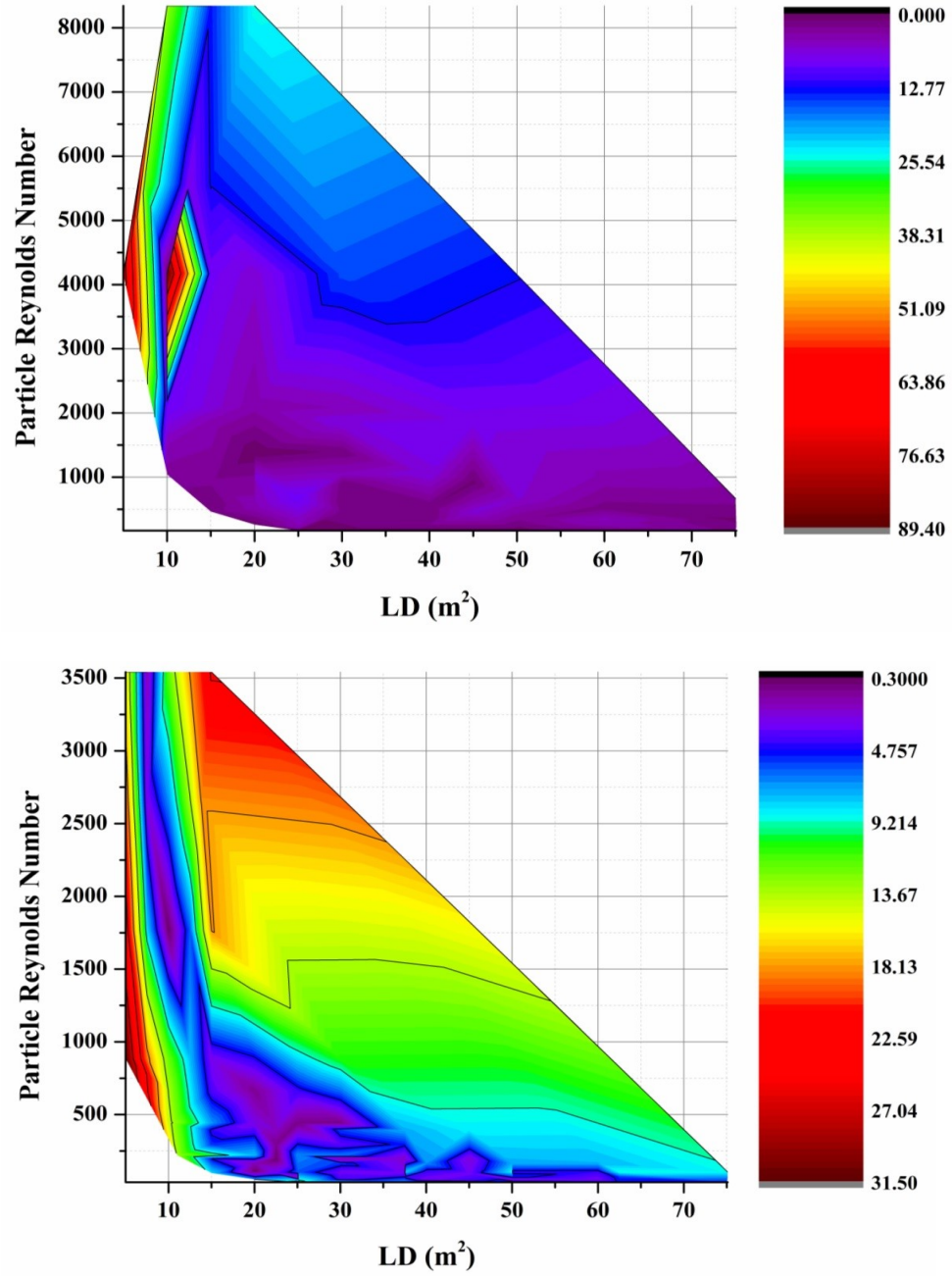

Figure 4.4/P-116 Error maps: ADGAS Adsorption Cases (top) & ADGAS Regeneration Cases (bottom)

4.4.2 SENSITIVITY STUDY RESULTS

Several case studies were conducted based on the model described previously. Instead of the NPW function described previously, the direct summation of MEC, OPEX, and BED

is taken as the probe function. This is summation is given the acronym (NPWC). An initial feasible point was found for these values of design variables: L=23 m, D=4.4 m, N=4, $T_{reg,G}$=520°C, N_1=1580 kmol h^{-1} for ADGAS and 2850 kmol h^{-1} for GASCO, t_{reg}=3.1 h, and t_{ads}=40 h. Following, the NPWC profile is determined by varying only one of the design variables L ,D ,N_1 or $T_{reg,g}$ while satisfying the constraints. Figure 4.5 depicts the trends of the NPWC and its elements (i.e. major equipment cost, operating cost and bed replacement costs) for the ADGAS and GASCO cases as a function of bed length. NPWC is significantly lower for ADGAS than the one of GASCO (~37%). Overall, NPWC trends exhibit cyclic behavior with lowest NPWC values being attained at the lowest possible bed length. This behavior can be explained by looking at the elements comprising NPWC:

1- The major equipment cost increases linearly with bed length. This is a direct consequence of the linear dependency of the bed and vessel masses on bed length.
2- Operating costs are independent of bed length. This is expected considering that operating costs are due only to regeneration parameters (N_1 and $T_{reg,g}$) which were fixed for this part.
3- The bed replacement exhibits a cyclic trend with bed length. Over each cycle, the bed replacement cost increases with bed length, and then falls once a critical value is reached. The cycles' period (i.e. the difference between subsequent critical length values at which the sharp decline is observed) appears to increase with increasing bed length. Moreover, the amplitude of the cycle seems to decrease with increasing bed length.

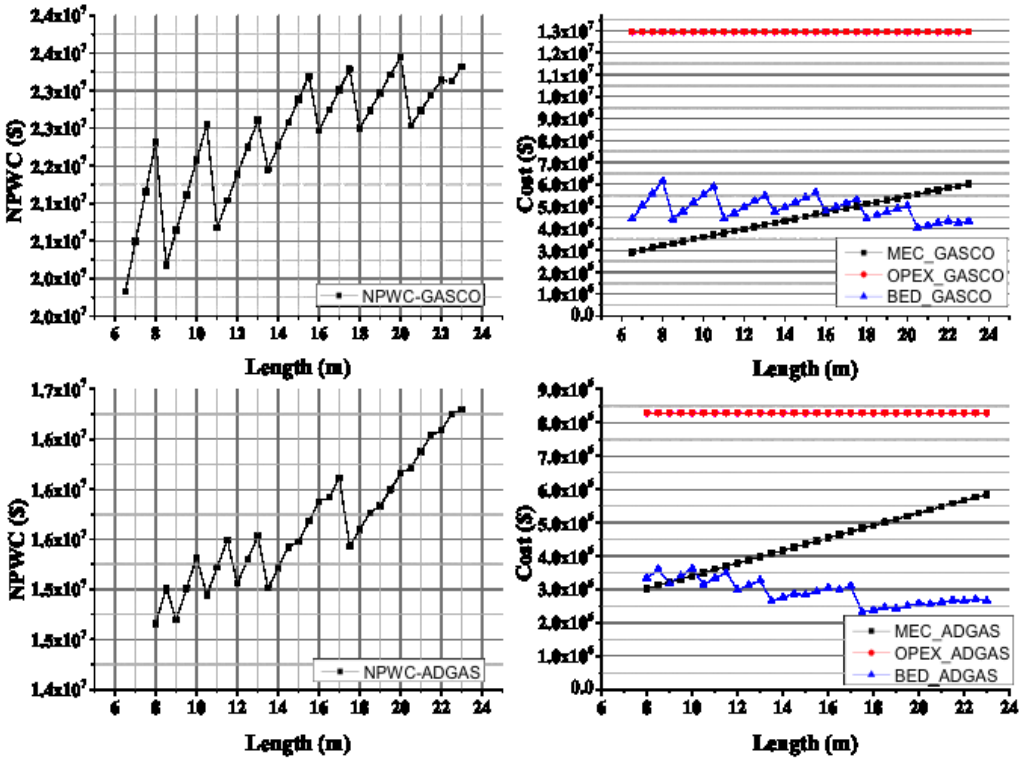

Figure 4.5/P-109 Response of NPWC and its elements towards changes in the bed length

Bed replacement is ensued upon experiencing a fixed number of regeneration cycles (1000 in this case). The time in years after which bed replacement is due is found as follows:

$$f = \frac{t_{ads} \cdot N_R}{4380} \quad (4.27)$$

Practically, f is rounded down to the nearest year in order to match the shutdown period of the plant. Over the course of the project life, the number of times bed replacement is conducted is strongly dependent on f. For instance, an f value of 3 years is equivalent to replacing the bed 9 times over the course of 30 years while an f value of 4 years is equivalent to 7 bed replacements over the course of the same period. Due to the effect of rounding, slight changes in bed length and hence in adsorption time can lead to dramatic

changes in f (e.g. going from 3 to 4), and thus, a dramatic decrease in the number of bed replacements despite the slight variation in the mass of sorbent replaced. Moreover, with higher bed lengths (i.e. higher f values) the number of bed replacement does not change dramatically (for an f value of 11 to 14, only two bed replacements are conducted). This explains the increasing period of the bed replacement cycles with bed length and decreasing cycle amplitude. Over a single cycle the bed replacement element cost is lowest at the lowest feasible length. Similar behavior is found for the dependency on bed diameter (figures not shown here). For N_1 and $T_{reg,g}$ (figures not shown here), NPWC exhibited a linearly increasing trend caused primarily by increase in the operating costs.

The results analyzed thus far suggest the existence of minimum NPWC values at the lower bounds of the design variables. However, the range of feasible values of the design variables, once one is fixed, is determined by the constraints shown in Table 2. In an attempt to analyze the change in NPWC while taking this into account, I performed a second set of sensitivity analyses, whereby I transformed all but one of the inequalities (pressure drop) into equality constraints and varied one design variable. Considering the seven design variables, two degrees of freedom have to be set in order to obtain a solvable set of equations. For convenience, I chose the number of vessels (N) and the temperature of regeneration gas $T_{reg,g}$ set at 4 and 520^{o}C respectively. Then, the system of equations was solved considering a maximum pressure drop and foot print of 30 kPa and 250 m^2 respectively. Next, the NPWC function and its comprising elements were evaluated as a function of bed length.

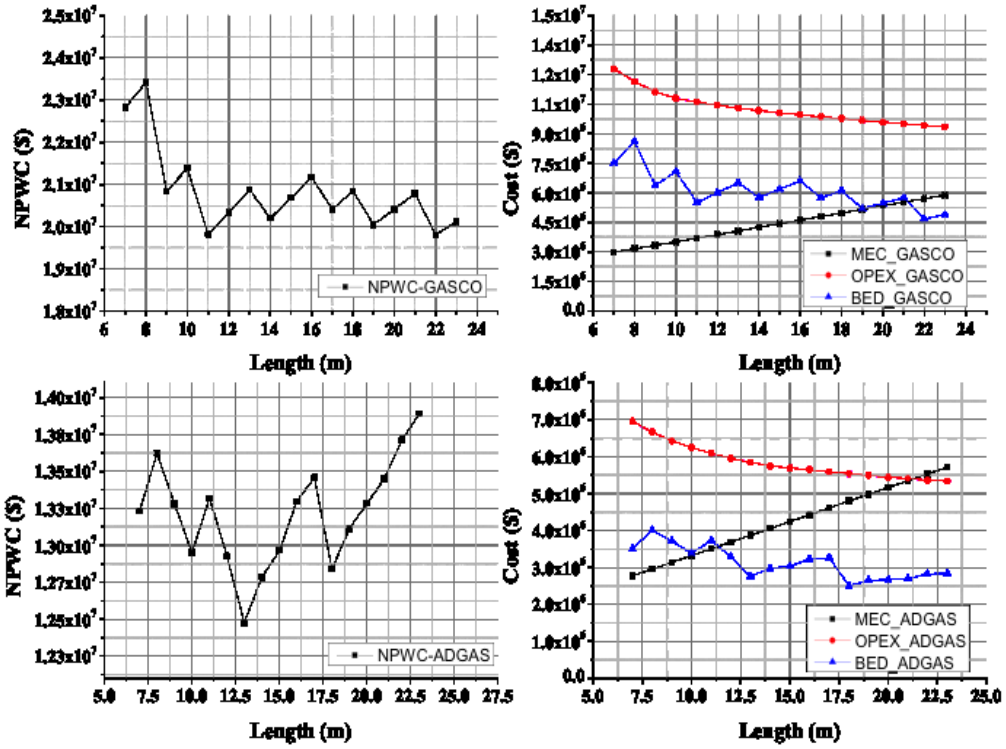

Figure 4.6/P-111 Response of NPWC and its elements towards changes in the bed length while enforcing cycle balance

The results are shown in Figure 4.6. The NPWC in the ADGAS case hints at the existence of an optimum at the vicinity of 12.5 m while such optimum is not clear in the GASCO case. Looking at the comprising elements of NPWC, the major equipment cost appears to increase linearly with bed length in line with what was observed previously. Bed replacement cost exhibits the same behavior as observed previously. However, the operating cost element decreases with bed length. The increase in bed length translates to an increase in the mass of sorbent requiring regeneration, hence leading to higher operating costs. Concurrently, the increase in bed length translates to an increase in the adsorption cycle time, and in turn, an increase in the time available for regeneration. As a consequence, the rate of energy supply required for regenerating the bed, which is governed by the

regeneration gas flow and temperature, decreases. Accordingly, the operating cost decreases. The latter factor dominates as suggested by results presented in Figure 4.6.

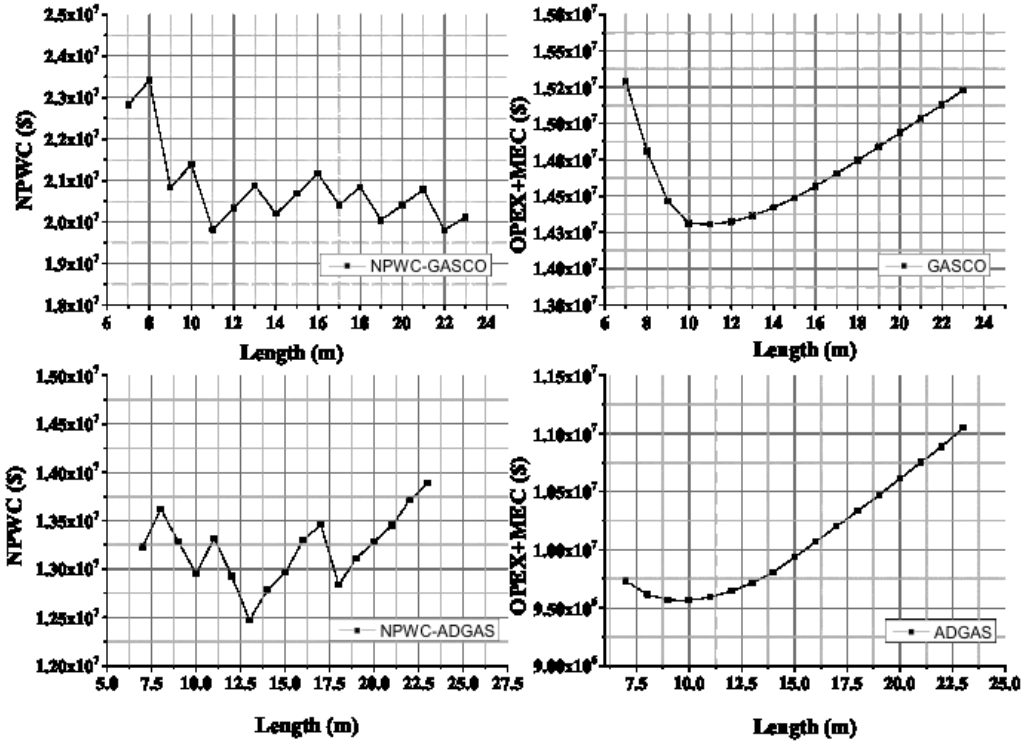

Figure 4.7/P112 Comparison between NPWC with (left figures) and without (right figures) the bed replacement element

Figure 4.7 depicts a comparison between NPWC computed with and without the bed replacement element. A minimum is observed in the absence of the bed replacement element for both the ADGAS and GASCO cases. However, as the bed replacement contribution is significant (up to 30%) it should not be excluded from the NPWC calculation. The above sensitivity analysis is based on the assumption that the optimum lies on the surface defined by the equality constraints, which is not necessarily true. Hence, an optimization approach is needed to determine optimal set of decision variables that will minimize NPWC and thus the NPW function. In the following section, I present the

detailed optimization protocol which will be followed in order to arrive at the realistic optimal solution.

4.5 THE OPTIMIZATION PROTOCOL

The conducted sensitivity studies suggest that the source of the NPW discontinuities stems from the bed replacement element, which introduces cost cash flows at distinct points in the NPW function. The time instants at which bed replacement is ensued are strongly dependent on the total cycle time. The exact timing at which bed replacement is due is given by the bed replacement period f:

$$f = \text{int}\left(\frac{N_R \cdot t_{ads}}{4380} \right) \quad (4.28)$$

where the function **int** rounds the result of the expression within the brackets to the nearest integer. Clearly, slight changes in the adsorption time cycle t_{ads} can lead to significant changes in the value of f, which in turn significantly affect the NPW function as suggested by expression (1). To overcome these difficulties, I propose a dual step approach for arriving at the optimal solution. In the first step, the governing model is recast from its PDE form into a set of nonlinear algebraic equations and a first approximation of the optimal solution is found, through the following protocol:

1) The adsorption step is assumed to be isothermal hence eliminating the need for simultaneous solution of the energy balances. This permits the use of the mass transfer corrected equilibrium based analytical solution in estimating the expected breakthrough time given by expression (4.16).

2) The regeneration step is modeled in a similar way to a pure substance phase change. The bed and the vessel steel are heated to an experimentally determined regeneration temperature. Then, isothermal removal of adsorbed contaminants occurs. Finally the bed and the vessel steel are cooled down to the operating temperature. None of the contaminants is assumed to elude during the cooling and heating steps.
3) An analytical solution is used to compute the required heating and cooling times based upon global energy balances. The regeneration time (i.e. the time at which the adsorbed contaminants are removed isothermally) is computed using the same approach described earlier for adsorption.
4) I introduce the bed replacement period, *f,* as an integer design variable instead of the adsorption cycle time $t_{ads.}$ The bounds for *f* are set from 3 to 15 years in line with the general norm of shut down frequencies for gas processing plants. The resulting optimization problem now includes two integer variables (*f* and *N*) with a small number of possible values. The original objective function remains unchanged.
5) The resulting MINLP problem is then transformed to a set of NLP sub-problems corresponding to all possible combinations of *f* and *N*. The resulting NLPs are solved using an SQP based algorithm coupled with a multi-start subroutine which generates 100 randomly distributed initial guesses. The resulting NLPs are solved using the *fmincon* Matlab™ function with the SQP option.

The resulting solution from the protocol is used as an initial guess in the second step, during which the full-scale PDE model detailed in chapter 3 is optimized for a reduced set of

optimization variables, which comprises only the continuous ones. gPROMS™ version 3.7.1 CVB_SS optimization routine is used for the solution. The PDEs are discretized to forty finite elements using second order orthogonal collocations. The resulting system is integrated in time and the sensitivities are computed using the DASOLV solver. In the upcoming chapter, a realistic case study is presented wherein the experimentally determined properties of the adsorbent selected are used in the protocol.

4.6 CONCLUSIONS

This chapter addressed the challenges that exist in optimizing adsorption systems. Given the complexity of the models employed and the nonlinear discontinuous nature of the chosen objective function, a two-step optimization protocol is suggested as a mean to arrive at the optimal design for the proposed unit thus providing a fair ground for benchmarking against commercial technologies. The upcoming chapter addresses the adsorbent side of the process.

CHAPTER 5: ADSORBENTS – REVIEW & EXPERIMETNAL ASSESSMENT[6]

5.1 INTRODUCTION

The previous chapters have laid the necessary foundation for the optimization and economical assessment of the proposed TGTU. A cornerstone of the proposed TGTU process is the adsorbent material which will perform the targeted removal. This chapter reviews and experimentally assesses a selection of the reported adsorbents in literature which have desirable adsorption properties towards sulfur species. The chapter begins with a review of two classes of reported adsorbents in literature: metal oxides and metal exchanged zeolites. Following, a comparative study is presented during which a single adsorbent is selected among the reviewed materials based upon its adsorption characteristics, its price, and availability of data on it. Next, the details of conducted experimental studies on the selected adsorbent are presented associated with details of the followed experimental protocols, data regression, and results discussion. The chapter ends with the conclusions of the studies conducted.

5.2 ADSORBENTS REVIEW

For adsorption systems to be a viable option in Claus Tail Gas clean up, the sorbent active temperature range should lie between 393 and 423 K. Moreover, the sorbent regeneration conditions must be mild enough to allow use of carbon steel; i.e. less than 773 K [69].

[6] Significant segments of this chapter are published in (Al Wahedi et al., Chem Eng. Sci., 2014). License for reproduction in thesis was obtained under the number 3550021329985.

Several adsorbents were reported to be highly active towards H_2S adsorption in literature. Over the temperature range 298 K to 370 K, siliceous based functionalized adsorbents and Metal Organic Frameworks (MOFs) are favored due to their relatively high capacity and good regenerability. In functionalized siliceous materials, Belmabkhout and co-workers reported a tri-amine functionalized MCM-41 adsorbent with a stable capacity of ~3.4 mmol g^{-1} at 298 K, 1 bar pressure in pure H_2S [119]. Sorbent regeneration is performed in vacuum at 348 K. In addition, Huang et al. reported an amine grafted MCM-48 based adsorbent with a capacity of 13.5 cm^3 g^{-1} at 0.001 atm H_2S partial pressure and 298 K [120]. In MOFs, Hamon et al. studied the adsorption capacities of several MOFs with varying metal core at room temperature [121]. The reported capacities ranged from 1 to 3 mmol g^{-1} at 20 kPa H_2S partial pressure. Heymans et al. reported that the saturation capacity of H_2S on MIL-53 is 15.1 $mmol \cdot g^{-1}$ assuming Toth adsorption isotherm model to apply at 303 K [122]. On MIL-68, Yang et al. reported ~10 $mmol \cdot g^{-1}$ as the saturation capacity at 303 K [123]. At temperatures exceeding 370 K, the attained capacity of MOFs and functionalized siliceous materials is very limited. Considering the expected high prices of MOFs coupled with the absence of evidence suggesting their applicability in temperatures relevant to the Claus process, the potential for their application is miniscule and hence they will be excluded from the upcoming analysis.

For both low and high temperature applications (>523 K), metal oxides and mixtures thereof attain the highest reported capacities. Unlike conventional sorbents, metal oxide based sorbents chemically bind with H_2S by exchanging the sulfur atom in H_2S with an oxygen atom thus transforming the metal oxide into a metal sulfide. This chemical reaction renders metal oxide adsorbents very high capacities and sub-ppm equilibrium

concentrations of H_2S. Several studies were conducted on mixed oxide sorbents for the removal of H_2S [124]. Reported capacities range between 2 and 8 mmol·g^{-1}adsorbent. Such a high capacity renders a promising option for Claus tail gas clean up. However**,** the profound disadvantage of metal oxides based adsorbents lies in the requirement for high regeneration temperature (>873 K) in order to assure complete decomposition of metal sulfates, a common side product that results during the oxidation of the metal sulfide to metal oxide [125]. Metal exchanged zeolites satisfy the requirement for intermediate temperature application of that of Claus tail gas and the property of full regenerability at relatively mild temperatures. Kumar et al. reported a study on several Faujasite based exchanged sorbents [15]. Their capacities ranged between 1 and 2 mmol·g^{-1} in the temperature range of 298 to 423 K. Crespo et al. reported a copper exchanged zeolite Y sorbent prepared via vapor ionic exchange protocol. The sorbent saturation capacities were 7.15 mmol·g^{-1} at 298 K and 2.36 mmol·g^{-1} at 333 K [14]. Full regenerability has been achieved using air as the purge medium and at a temperature of 523 K. Modeling parameters were obtained for the adsorption step using standard adsorption isotherms such as Sips [14]. Still, studies on the adsorbent chemical structure, long term adsorbent regenerability, and adsorption kinetics are lacking. The properties of metal oxides and metal exchanged zeolites render them high potential options for Claus tail gas clean up. Herein, I present detailed review of reported results on both classes of materials.

5.2.1 METAL EXCHANGED ZEOLITES

Zeolites and especially their metal exchanged forms exhibit a wide interval of temperature applicability extending from ambient up to 150^{o}C. Although they suffer from relatively low capacities at temperatures in excess of 100^{o}C (<3 mmol.g^{-1}), the ease of their

regeneration renders them a potential option for Claus tail gas clean up. Literature studies conducted on H_2S and SO_2 capture by zeolites focused for the most part on low silicon to aluminum ratio (Si/Al) zeolites. In this section, I present a review on the reported literature on H_2S and SO_2 adsorption over zeolites and metal exchanged zeolites. Starting with H_2S then SO_2, the review presented herein focused on the following topics: i) the role of the zeolite structure, ii) adsorption mechanisms, and iii) the role of metal cations on the adsorption of the studied species.

Focusing on H_2S, its adsorption affinity was found to be proportional to the degree of hydrophilicity of the adsorbent which is generally determined by the Si/Al of the zeolite. Cosoli and co-workers investigated the adsorption properties of H_2S in pure form and in a mixture of CH_4 and CO_2 over four zeolite frameworks via molecular simulations [126, 127]. In their first study, grand canonical Monte Carlo molecular simulations relying on the Metropolis approach for sampling was used in probing the adsorption of H_2S over four zeolite frameworks: FAU Na-Y, FAU Na-X, LTA and MFI) [126]. The simulations were conducted at 298K and at varying partial pressure of H_2S. In the mixture case the total pressure of system was kept at 1 atm. Quantum simulations were done in order to obtain partial charges and optimized structures of the adsorbates. Following, adsorption equilibrium capacities, isosteric heat of adsorption and binary selectivities were determined for the studied adsorbates via the molecular simulations.

In all cases, H_2S adsorption was found to be favored over hydrophilic zeolites. LTA and FAU zeolites exhibited the highest loadings over the studied range of H_2S partial pressure. The same trends were observed in the mixture case but with significantly lower capacities. Over all the studied zeolites, CO_2 strongly competes with H_2S over adsorption sites.

Furthermore, CO_2 adsorption was found to be unaffected by increasing H_2S partial pressures within the range 0 to 1 kPa. Reported isosteric adsorption enthalpies of H_2S were highest over Na-Y and Na-X with values of 17.9 and 15.6 kcal.mol^{-1} respectively. Isosteric adsorption enthalpies for CO_2 were lower in the case of Na-Y and Na-X with values of 11.4 and 12.3 kcal.mol^{-1} respectively. H_2S selectivities were found to be highest over both zeolites with Na-Y exhibiting the highest selectivities towards H_2S. Interestingly, the computed selectivities exhibited a decreasing trend with increasing H_2S partial pressures.

In another study by Cosoli et al., molecular dynamic simulations were conducted as to study H_2S selective adsorption pathways over Na-Y if the adsorption sites are initially occupied by CO_2 and CH_4 [127]. In addition, adsorption binding energies were computed as a function of time. System equilibration was found to occur well below 500 ps. Furthermore, CO_2 adsorption was not affected by introduction of H_2S thus confirming Monte Carlo simulation results. In contrary, methane molecules initially placed within the system were completely exchanged with H_2S at time of equilibration. Binding energies determined at the equilibration point showed weak dependency on the loading retaining a stable value of -15 kcal.mol^{-1} for H_2S at an H_2S partial pressure of 10 Pa. Same values were observed at a 50 Pa H_2S partial pressure.

The nature of H_2S adsorption being dissociative or molecular was studied by Karge and co-workers using spectroscopic based methods [128, 129]. In the first study, Karge and co-workers investigated via Infra-red spectroscopy the species formed during adsorption of H_2S over the surface of sodium form FAU zeolites with varying Si/Al ranging between 1.05 and 3.24 [129]. At low H_2S partial pressures, dissociative adsorption is observed for samples with Si/Al < 2.5. This was characterized by the formation of SH^- species and acidic

OH^- species as confirmed by the increased intensity of IR peak at 3650 cm^{-1} corresponding to OH^- and 2560 cm^{-1} corresponding to SH^-. For higher Si/Al values and higher H_2S partial pressures, molecular adsorption was observed. The reported results suggest that dissociative adsorption correlates with the number of sodium ions. Sodium ions act as anchors for the SH^- segment of H_2S. The remaining proton migrates to a nearby framework oxygen thus forming a Brønsted acid site. The acidity was confirmed by standard pyridine treatment.

In another study by Karge et al., early adsorption stage of H_2S over Na-X was investigated by UV and visible range spectroscopy [128]. Early adsorbed H_2S molecules dissociate completely to S^{2-} indicated by the appearance of 250 nm band in the UV range. With progressive increase in H_2S partial pressure, the adsorption evolves from being complete dissociative to partial dissociation and ending with molecular adsorption. Garcia and Lercher investigated via infra-red spectroscopy, temperature programmed desorption, and gravimetric methods H_2S adsorption over H-MFI and Na-MFI [130]. Their Na-MFI results confirms earlier reported results by Karge et al. Over H-MFI, H_2S adsorbs coordinatively with the Brønsted hydrogen. The cumulative evidences of all the aforementioned studies confirms that H_2S adsorption affinity is proportional to the degree of acidity and that it proceeds firstly via dissociative adsorption of H_2S followed by molecular adsorption. Furthermore, FAU zeolite structure is the most suitable for H_2S adsorption. There is disagreement whether the Y form or the X form leads to higher adsorption loadings of H_2S.

Moving the focus to the role of the metal, Kumar et al. studied H_2S pure and competitive adsorption via breakthrough tests over silver and copper exchanged FAU zeolites and benchmarked the results to Na-X [15]. Competing species included N_2, CO_2, CO and H_2O.

The role of the copper coordination number was also studied. Finally Density Functional Theory (DFT) simulations were conducted were their results are correlated to experimental observations. With a concentration of 100 ppmw H_2S in N_2 at room temperatures, the reported capacities in decreasing order were AgX>AgY>CuX>CuY. The same order is retained at 150^oC but higher capacities are observed for copper exchanged zeolites. Kumar et al. attributed the unexpected increase in capacity to activation of adsorption sites with increasing temperature.

Studies on competitive adsorption suggested strong competition by CO on copper exchanged zeolites unlike silver exchanged ones which did not experience significant reduction in their adsorption capacity towards H_2S. Competition by water was observed over Na-X and Cu(II)-Y. Water competition was not observed in the other studied materials. Adsorption energies computed via DFT studies followed the observed trends on competitive adsorption studies. Cases where strong competition is observed correlated with higher adsorption energy of the competing adsorbate compared to H_2S. Sung et al. followed up Kumar and co-workers in the assessment of the adsorption of H_2S and adsorbate competition over alkali exchanged FAU-Y zeolites in addition to copper and silver via DFT studies [131]. The study focused in its entirety on Site II in the FAU crystal structure (see Figure 5.1).

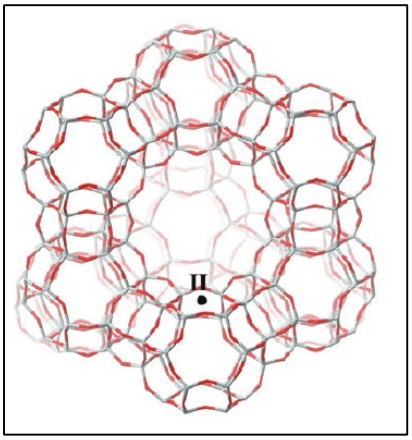

Figure 5.1/P-123 Depiction of FAU zeolite crystal structure with site II marked (Reprinted (adapted) with permission from [131]. Copyright 2012 American Chemical Society

A representative cluster model is taken in which a single aluminum atom is introduced into cluster as to disrupt the charge balance. Following, the metal of interest is introduced at the center of the cluster and is allowed to relax to its lowest energy configuration. Four levels of DFT simulation were conducted. In the first level simplified energetic computations were initially performed on the adsorbate and the bare cation and then on the cation situated within the zeolite structure. This approach allowed decoupling the zeolite cluster effect from the metal. In the second level orbital analysis was conducted in order to compute the charges distribution of the adsorbate, metal and the zeolite cluster. In the third level, Absolutely Localized Molecular Orbital Energy Decomposition Analysis (ALMO EDA) was conducted. This analysis decomposes the interaction energetics to its elements which includes: geometry distortion, charge transfer, and polarization in addition to others. Finally, Complementary Occupied-Virtual Orbitals Pairs (COVPs) analysis was performed as to determine the charge transfer events.

Computed adsorption energies of metal cations towards the studied adsorbates within the zeolite clusters exhibited substantially lower values when compared to bare cations. In

addition the order changed substantially. In bare cations, the order of computed energies in decreasing trend was $H_2S>H_2O>CO>CO_2\approx N_2$ over both copper and silver. The order changed dramatically when situating the metal within the zeolite cluster with CO adsorption energy becoming substantially higher compared to H_2S in the case of copper.

ALMO EDA analysis showed that the charge transfer component of the interaction energy is the major contributor in copper and silver exchanged zeolites. In alkali metal exchanged zeolites non-charge transfer components contributes the most. The COVPs analysis showed that H_2S and CO adsorb via forward donation from the copper filled d-orbital to the anti-bonding π^* orbital and backward donation from the adsorbate molecule to the valence shell of the metal. The filling of the anti-bonding orbital leads to the dissociation of the H_2S. In the case of H_2S, the coordination occurs between the sulfur atom and the metal and between the hydrogen atom and the oxygen in the zeolite framework. In the CO, the donation to the metal occurs via the carbon atom. The zeolite framework acts as an electrons reservoir which saturates the unfilled s and p orbitals in the metal cation, thus decreasing its ability to receive electrons from the adsorbate. This effect apparently is more substantial in H_2S over CuY compared to CO. In silver the effect is less pronounced probably due to the higher energy of the s and p orbitals of silver requiring higher energy electrons supply form the zeolite framework. Finally, the zeolite framework influence on the adsorption phenomenon occurs mainly via affecting the charge transfer component i.e. the energetics of adsorption not via geometric stabilization of the adsorbate-metal complex.

I end this review on H_2S adsorption with the notable work of Crespo et al. who was the first in introducing the use of vapor exchanged CuY zeolite as a potential adsorbent for H_2S [14]. Crespo and coworkers studied the adsorption of H_2S over several supports

including zeolite Y, MCM-41 and SBA-15 loaded with Copper or silver. Preparation methods included copper exchanged zeolite Y prepared via the vapor ionic exchange method CuY and Cu(II)-Y, silver exchanged zeolite Y prepared via liquid exchange method Ag(I)-Y and CuCl loaded via monolayer dispersion method over the siliceous supports (MCM-41, SBA-15). Adsorption isotherms of H_2S were collected for various adsorbate mole fractions at two temperatures 25^oC and 60^oC using the thermal gravimetric method. Following, the resulting isotherms were fitted using Langmuir-Freundlich isotherm. Reported results showed that CuY prepared via the vapor exchanged method achieved the highest saturation capacity of 7.15 $mmol \cdot g^{-1}$ at 25^oC and 2.36 $mmol \cdot g^{-1}$ at 60^oC. Notably, Kumar et al. observed an increase in capacity at the same concentration with increasing temperature for the case of CuY [15]. Furthermore, Kumar et al. reported lower equilibrium capacities over the same material CuY under the same concentration [15]. This suggests that both groups (Crespo et al. and Kumar et al.) tested dissimilar CuY although the parent zeolite and the exchanging process used were the same. Crespo et al. reported full regenerability of the sorbent under air at 350^oC.

Similar to H_2S, SO_2 adsorption was found to be proportional to the degree of hydrophilicity of the adsorbent measured by the Si/Al value. Tantet and coworkers studied the adsorption of SO_2 over MOR and MFI zeolites with varying Si/Al ranging between 22 and 700 [132]. Adsorption isotherms were determined via the gravimetric methods, while kinetic analysis was performed via the breakthrough method. The adsorption properties of SO_2 were benchmarked with H_2O. Langmuir-Freundlich isotherm was selected as the thermodynamic model while the linear driving force model was selected for breakthrough curves fitting. Adsorption experiments were conducted at 50 to 55^oC using a either a pure

feed containing 2000 ppmv SO_2, 3.2 to 5 vol% H_2O or a mixture thereof with the balance being nitrogen. The reported results for the pure feed cases show that both SO_2 and H_2O adsorption loadings over MOR and MFI decreases with increasing Si/Al value. The results suggest inverse proportionality with the Si/Al. The hydrophobic index defined as the ratio between the adsorption capacities of SO_2 to H_2O was found to decrease with increasing Si/Al value up to 100. At the maximum Si/Al value studied (700 for MFI), the hydrophobic index is substantially higher. This suggests that Van der Waals interactions favors SO_2 adsorption over water in the limit of high Si/Al ratio. The results of the hydrophobic index also suggests that SO_2 adsorption is favored at lower Si/Al values and is higher over MFI when compared to MOR. Pure component isotherm parameters based on the Langmuir-Freundlich model were incorporated into the extended form of the isotherm model. The resulting extended model was then compiled with the breakthrough linear driving force model and thus used to fit breakthrough experimental data. Good fit was realized using the extended Langmuir-Freundlich isotherm.

To investigate SO_2 adsorption over hydrophobic zeolites, Deng and Lin measured the SO_2 uptake by dealuminated zeolite Y and silicalite at SO_2 partial pressures ranging between 0.5 and 5 kPa at three test temperatures: 25^{o}C, 50^{o}C, and 100^{o}C [133]. The resulting isotherms were fitted using the single component Langmuir model and Freundlich model. The reported results suggested substantially higher capacities of SO_2 over silicalite. The saturation capacities predicted by the Langmuir model were 2.762 mmol·g^{-1} and 0.293 mmol·g^{-1} over silicalite and dealuminated zeolite Y respectively. Reported heat of adsorptions were 14.1 and 21.3 kJ.mol^{-1} over silicalite and dealuminated zeolite Y respectively. Similar heat of adsorptions were computed via the Freundlich model.

Thermodynamics and kinetics of the adsorption of SO_2 and competitive adsorption over zeolite 13X and 5A were also studied by Deng et al. using the volumetric dosing method [134]. The studied species included CO_2, NO, and N_2 with the studied partial pressure range extending between 0 to 100 kPa at three temperatures: 323 K, 348, and 363 K. Adsorption enthalpies, entropies and Gibbs free energies were computed as a function of partial pressure. In general, SO_2 adsorption was favored over all the studied species in both zeolites with higher capacities being reported over zeolite 5A. Furthermore, computed heats of adsorption of SO_2 exhibited a linearly decreasing trend with partial pressure starting at 5 $kJ.mol^{-1}$ at the lowest pressure and reaching 15 $kJ.mol^{-1}$ at the highest pressure. This decrease is synonymous to attractive adsorbate-adsorbate interactions [135]. The adsorption entropies also exhibited a similar trend over the studied range of pressures. The authors attributed the decrease in entropies to the decrease in available space for adsorption with increasing coverages thus leading to smaller free space for motion for the adsorbate and hence lower number of possible configurations.

Adsorption mechanisms of SO_2 over zeolite Y and X were studied via spectroscopic techniques including UV, Vis and IR methods [136] . Unlike H_2S, SO_2 was shown to adsorb as a single species over Na-Y exhibiting an IR band at 1320 cm^{-1}. Two bands were observed at 1240 cm^{-1} and 1305 cm^{-1} when considering adsorption over Na-X [136]. Nasluzov et al. conducted a DFT study in order to explain the nature of SO_2 adsorption on the protonated zeolites using a Si-O-Al-O-Si segment as a mean of representing the zeolite [137]. IR vibrational bands were computed and compared to experimentally reported results. Qualitatively the results agree with experimental findings which suggests that SO_2 interacts with the proton to form the adsorbed complex. The complex is stabilized via

donor-acceptor interactions with nearby oxygen atoms in the structure. The deficiency in the study conducted by Nasluzov et al. lay in not considering the whole cluster form of the zeolite under study. Hence, the discrepancy in their estimated IR vibrational frequencies against experimental results might be caused by the disregard of the zeolite structure.

Role of the metal cation on SO_2 adsorption was investigated by Teraoka et al. for a multitude of zeolite structures and Si/Al values [138]. Protonated zeolite Y was compared with alkali and alkali earth as the exchanging metals in zeolite Y and MFI. The tests were conducted using the volumetric dosing technique at 298 K over a range of pressures extending between 0 to 0.9 atm. Following adsorption, the samples were evacuated at the same temperature under vacuum (0.01 torr). The evacuated SO_2 is then considered weakly bonded while the retained SO_2 is considered strongly bonded. Total adsorbed capacities were highest in alkali exchange zeolites with Na-Y having the highest value of 6.04 $mmol.g^{-1}$. Most of the adsorption capacity in tested samples of H-Y zeolite was attributed to weakly bonded SO_2. The amount of strongly bonded SO_2 was found to increase with increasing ionic radius of the exchanging metal. To the best of the author's knowledge, none of the studies reported in literature considered SO_2 adsorption at temperatures relevant to the Claus process.

In summary, H_2S adsorption over metal exchanged zeolites was studied at temperatures relevant to the Claus process. IR studies suggested full dissociation of the molecule during early adsorption, followed by partial dissociation in intermediate coverages, and molecular adsorption at higher coverages. Reported DFT studies suggested that the enhanced selectivity of copper and silver exchanged zeolites is attributed to the charge transfer action that occurs between the metal d-orbital as a donor of electrons and s or p orbitals as the

acceptors while the anti-bonding π* molecular orbital in H_2S. This result explains the dissociative nature of early adsorption of H_2S.

SO_2 adsorption was primarily studied at temperatures below 100°C. No study was found for adsorption under Claus relevant conditions. Several studies reported highest capacities obtained with Na-Y. IR studies coupled with DFT suggested that SO_2 adsorb as a single species and that its adsorption occurs via electrostatic interaction with acidic proton thus forming a complex which is further stabilized by nearby oxygen atoms.

5.2.2 MIXED METAL OXIDES

Metal oxide adsorption behavior towards H_2S have been studied extensively in literature for high temperature purposes such as coal gas desulfurization [124]. Unlike conventional sorbents, metal oxide based sorbents chemically bind with H_2S by exchanging the sulfur atom in H_2S with an oxygen atom thus transforming the metal oxide into a metal sulfide. Several studies were conducted on mixed oxide sorbents for the removal of H_2S [124]. Table 5.1 summarizes the findings of a sample of those studies, which managed to achieve H_2S removal below 50 ppm.

Reference	Material	System Temperature range (°C)	Capacity [mmol·g^{-1}]
Polychronopoulou et al. [16]	Zn-Mn-Ti-O	25-100	1.2-4.6
Polychronopoulou et al. [17]	Zn-Fe-Mn-Ti-O	25-100	0.5-8
Li et al. [139]	Cu-Cr-O	350-850	0.94-3.8
Li et al. [139]	Cu-Ce-O	350-850	0.84-5.5
Yasyerli et al. [18]	Cu-V-O	300-600	4.5-5.3
Yasyerli et al. [44]	Cu-Mo-O	300-600	3.4-6.9
Karayilan et al. [19]	Cu-Mn-O	627	4.7
Karayilan et al. [19]	Cu-Mn-V-O	627	3.4

Table 5.1/P-130 A sample of mixed oxide sorbents reported in literature

SO_2 removal via mixed oxide sorbents has achieved commercial application in the MOST process by Mobile. The MOST process involve complete oxidation of all sulfur species to SO_x and subsequent adsorption on a solid sorbent at 650^oC [65]. Regeneration of the sorbent is realized by introducing a reducing gas of H_2 to recover the oxide form. The study conducted by Stern et al. identified a promoted $Mg_2Al_2O_5$ with cerium and vanadium to possess the highest capacity towards SO_x adsorption (> 50 wt%) based on breakthrough studies utilizing a gas containing 1% SO_2, 4% O_2, 10% H_2O, and balance nitrogen [65]. Successful SO_2 removal from a simulated coal feed gas was also achieved by a CuO supported on γ-Al_2O_3 [140].

Utilization of mixed metal oxides for H_2S removal has been done for a variety of purposes including, stability enhancement by prolonging activity [141], surface area enhancement [142, 143], and kinetics enhancement [144]. The research work conducted on the field of H_2S sorbents identifies the following attributes for a successful sorbent: i) favorable kinetics and thermodynamics, ii) high external surface area iii) retention of stability and activity upon tens of successive cycles iv) selective removal of desired species among competing species, and v) high mechanical strength.

Favorable kinetics and thermodynamics are governed primarily by the energetics of the chemical reaction between the H_2S and the metal oxide [145]. Formation of mixed metal phases affects the energetics of the reaction [18] in addition to the oxidation state of the primary metal [146], which in turn may lead to synergistic effects that are not realized by physical mixing. Activity deterioration upon successive regeneration cycles was attributed to metal reduction and evaporation [147], formation of hard to regenerate phases [148],

and the formation of inactive phases due to mixed metal oxide decomposition upon regeneration [141]. Addition of stabilizing species assists in making metal reduction and subsequent evaporation difficult [149]. Furthermore, employment of short adsorption cycles was shown to cause retention of the activity of sorbent by preventing decomposition of the sorbent phase [17, 150]. The upcoming paragraphs present a literature review of metal oxide adsorption behavior towards H_2S and SO_2, including the thermodynamics of H_2S adsorption on mixed oxides, the mechanism of adsorption reaction and general kinetic findings. In addition, literature studies on the role of sorbent morphology are presented. Finally, literature on sorbent deactivation is also reviewed.

Thermodynamics of H_2S adsorption on single metal oxides was comprehensively studied for high temperature applications. Westmoreland and Harrison conducted thermodynamic screening of the equilibrium conversion of 28 metal oxides towards metal sulfides [145]. Those metals were chosen after reviewing the periodic table and rejecting radioactive metals and prohibitively expensive ones. The temperature range studied was between 350^{o}C to 1200^{o}C at a pressure of 20 atm, which is considered the range of choice for low Btu gases desulfurization. Two gas compositions were considered in the study representative of a US high sulfur fuel gas and for a gasifier effluent gas. Free energy minimization techniques were used for the elements system Metal-C-H-S-O-N in order to identify the thermodynamic stable composition. A fractional conversion beyond 95% was considered the benchmark for a potential candidate.

Among the studied metal oxides, aluminum, cerium, chromium, magnesium, potassium, lithium, sodium, titanium, and zirconium formed stable oxides or carbonates unreactive with H_2S. In addition, silver, lanthanum, nickel, and antimony could not meet the

benchmark conversion of 95% over the temperature interest although their potential at lower temperatures remain unidentified. Among the candidates, zinc had the widest temperature range of 350 to 1150^{o}C. Iron, copper, and manganese exceeded the benchmark of 95% conversion in lower ranges of temperatures. Calcium on the hand performed well above 750^{o}C.

The study conducted by Westmoreland et al. did not consider sorbent regenerability. Hepworth et al. studied the temperature ranges where H_2S adsorption is favorable and where subsequent sorbent regeneration via oxidation is favorable from a thermodynamic perspective [151]. The study was achieved by considering a number of the high potential candidates identified in the Westmorland et al. study [145]. Hepworth et al. considered five reactions, which are: i) the oxidation of the metal, ii) sulfidation of metal, iii) sulfidation of the metal oxide, iv) formation of metal sulfate from the metal sulfide and from v) the metal oxide. Temperature-free energy diagrams were presented for the studied reactions to determine the relative stability of the studied species. Among the studied metals, copper sulfide was shown to be the only stable metal sulfide beyond 750^{o}C. The Hepworth study appears to have been deficient since it only considered the relative stability of the reactions rather than determining the equilibrium extent of each reaction upon coupling them. Moreover, other possible metal compounds such as carbonates and carbides were not considered in the analysis.

Moving the attention towards mixed oxides thermodynamics, the literature is deficient in such studies most probably because the impossibility of covering plausible mixtures. A clear advantage is foreseen for the utilization of free-energy minimization techniques in assessing the relative potential of a mixed oxide phase over a constrained system of phases

in order to identify and target specific phases that are active towards H_2S adsorption. Moreover, the minimum H_2S concentration achievable with any sorbent is governed by thermodynamics hence; performing thermodynamic screening of sorbents is vital to assure its potential in Claus Tail gas clean up. Thermodynamics of SO_2 adsorption over metal oxides have not received adequate attention in literature. In zeolites, SO_2 adsorption behavior was found to be accurately captured by a linear isotherm [113].

Quantifying the kinetics of the adsorption for sulfur species allow for successful development of realistic models for the purpose of adsorption system scale up. A number of kinetic studies performed on H_2S adsorption over multiple metal oxides observed first order dependency of the reaction rate on H_2S concentration [124]. Moreover, adsorption experiments of H_2S over several metal oxides indicate that H_2S interacts with the metal center in the sorbent [152, 153]. SO_2 adsorption occurs by reacting with the oxygen center forming SO_3 and SO_4 [154, 155]. In addition, some studies observed strong correlation between H_2S adsorption kinetics and the band-gap of the sorbent [156]. This section presents a literature review on the adsorption kinetics of H_2S and SO_2.

Rodriguez et al. have conducted several DFT studies on H_2S adsorption over a number of metal oxides surfaces [153, 156-158]. In one of their studies, the nature of H_2S adsorption on multiple metal oxides (Al_2O_3, Cr_2O_3, Cr_3O_4, Cu_2O, and ZnO) was assessed using molecular simulations and synchrotron-high resolution photoemission [156]. At temperatures beyond 300 K, H_2S undergoes complete dissociation over all the studied oxides. The rate of H_2S dissociation was found to be lowest over Al_2O_3 and increases with decreasing band-gap of the studied metal oxides [156]. In another study Rodriguez et al. observed molecular H_2S adsorption on the surface of MgO at temperatures around 80 K

[158]. Beyond 300 K H_2S dissociates to H and HS. Further dissociation is observed with increasing temperatures. In ZnO, H_2S dissociative adsorption is observed at much lower temperatures [158]. In addition, Rodriguez et al. estimated the adsorption energy of H_2S, HS, and H over MgO [100] surface, Ni doped MgO [100] surface, and ZnO [0001] surface [158]. The adsorption energy of H_2S, HS, and S were found to be the highest over ZnO indicating higher chemical activity and hence faster kinetics over ZnO. Furthermore, the adsorption energies over any of the studied material was found to be in the following order: H_2S<HS<S. Higher adsorption energies are indicative of higher energy release upon adsorption. From those experimental observations, it can be concluded that the mechanism of H_2S adsorption is the following:

$H_2S + M\text{-}O \rightarrow H_2S\text{---}M\text{---}O$ (Step-1)

$H_2S\text{---}M\text{---}O \rightarrow HS\text{-}M + H\text{-}O$ (Step-2)

$HS\text{-}M + H\text{-}O \rightarrow S\text{-}M + H_2O$ (Step-3)

Since the adsorption energy of H_2S was found to be the lowest over many metal oxides when compared to HS and S, it can be concluded that Step-1 is the rate-limiting step. This conclusion is also supported by the observed first order dependencies of the rate on H_2S concentration [42].

Similar studies were done on SO_2 adsorption over several metal oxides [159, 160]. Rodriquez et al. studied SO_2 adsorption over Cr_2O_3 [0001], MgO [100]], and $Cr_xMg_{1-x}O$ [100] surfaces [157]. The S-O bond breakage was found to increase in the following order and $Cr_xMg_{1-x}O > Cr_2O_3$>MgO. The enhanced activity of the mixed oxide was attributed to

the lower oxidation state experienced by Cr and the lower stability of its 3d orbital, which favor interactions that promote S-O anti-bonding. In another study, Rodriguez et al. observed that the SO_2 adsorption proceeded over flat MgO (100) surface by formation of sulfite species which is the dominant at temperatures around 100 K [160]. Decomposition of the adsorbed species SO_3 to SO_2 is observed only at temperatures higher than 450 K at which the SO_2 is released in the gas phase. Over Cu/MgO surface the decomposition of SO_3 species leads to the formation of SO_4 species adsorbed to Cu [160]. Casarin et al. investigated effect of surface morphology on the adsorption enthalpy of SO_2 over TiO_2 (110) and $(10\bar{1}2)$ surfaces [161]. Casarin et al. concluded that SO_2 adsorption is favored over $(10\bar{1}2)$ surfaces since the higher Lewis acidity promotes S-O anti-bonding. Moreover, higher adsorption enthalpies are observed as a consequence of favorable adsorption. Based on the reported studies, it can be concluded that SO_2 adsorption proceeds in the following steps:

$SO_2 + M\text{-}O \rightarrow SO_3\text{---}M$ (Step-1)

$SO_3\text{---}M \rightarrow M\text{-}O + SO_2$ (Step-2a) Or $SO_3\text{---}M + O \rightarrow SO_4\text{-}M$ (Step-2b)

Depending on the sorbent used any of steps 2a or 2b can occur. Over MgO Step-2a is favored while over Cu/MgO Step-2b is favored [160].

Gibson, Harrison and Westmoreland studied the kinetics of H_2S adsorption over four metal oxides: CaO, MnO, ZnO and V_2O_3 over the temperature range 300-800^oC using the gravimetric approach using H_2S-H_2-N_2 mixture [162]. In the gravimetric approach the weight change of sorbent with time is measured at a specific temperature. Then, if mass

transfer effects are negligible the initial slope of the weight curve can be correlated with the intrinsic reaction rate as follows (slightly modified from Westmoreland et al. [162]):

$$rate = \frac{\left(b_{H_2S} / b_{MO}\right) \cdot \left(\frac{dW}{dt}\right)_o}{m_o a_o \left[MW_{MO} + \frac{b_{MS}}{b_{MO}} MW_{MS} \right]} \qquad (5.1)$$

Applicable for the generic reaction:

$b_{H2S}\ H_2S + b_{MO}\ MO \rightarrow b_{H2O}\ H_2O + b_{MS}\ MS$

where, b is the stoichiometric coefficient, W is the weight, t is the time, m_o is the initial weight of the sample, a_o is the specific surface area, MW is the molecular weight, MO is the metal oxide, MS is the resulting metal sulfide. Gibson et al. considered two elements of mass transfer; external mass transfer effects, and pore diffusion [162]. The latter can be neglected if initial reaction rates are considered since the reaction initially occurs at the exterior surface of the sorbent particle. Absence of external mass transfer effects was confirmed by absence of dependency between the apparent first order rate constant and the volumetric flow rate of the adsorbate gas. Results of the experiments concluded that the reaction intrinsic rate has a first order dependency on H_2S for all the studied oxides. Reaction rates were observed in the following order MnO > > CaO ≈ ZnO > V_2O_3. The Arrhenius parameters for MnO were found to be 0.386 $cm^4 \cdot min^{-1} \cdot mg^{-1} \cdot mol^{-1}$ for the pre-exponential and an activation energy of 5.69 $kcal \cdot mol^{-1}$. Pre-exponential terms in the oxides were an order magnitude lower than MnO, however the activation energy ranged within the same order of magnitude; 5-9 $kcal \cdot mol^{-1}$. Li et al. studied the kinetics of Cu-Cr_2O_3 and Cu-CeO_2 sulfidation following the gravimetric approach over the temperature range 650-

850ºC [139]. Their results indicated that the sulfidation of Cu-Cr_2O_3 proceeds first by initial reduction of CuO to Cu_2O followed by sulfidation to Cu_2S. Assuming a rate law of the form rate = k C_{H2S}^n , observed reaction orders on H_2S were 0.7 for CuO-Cr_2O_3 and 0.83 for CuO-CeO_2 with activation energies of the order 4 kcal·mol^{-1}[162]. The latter number is in same order of magnitude with the results obtained by Gibson et al although the reaction order obtained did not agree. Disagreement in the reaction order may be attributed to the rate expression used by Li et al. since it did not consider the solid material activity effect. Yasyerli et al studied the breakthrough kinetics of Cu-V-O and Cu-Mo-O sulfidation over the temperature range 300-700ºC using the breakthrough approach [18]. In the breakthrough approach, the adsorbate gas is passed through a bed of sorbent and the outlet concentration of the adsorbate is measured in time. Yasyerli et al. obtained an excellent fit for the their breakthrough curves while considering first order dependencies on the activity of the solid and on the H_2S concentration while neglecting all mass transfer effects.

SO_2 adsorption on CuO supported on γ-Al_2O_3 was studied by Centi et al. over the temperature range 250-400ºC [163, 164]. The reaction was found to proceed on the following sequence of steps: i) SO_2 chemisorb on oxygen center within the framework to form SO_3 ii) following, the SO_3 reacts with a neighboring Al center to form aluminum sulfate and at a slower rate with a Cu center to form copper sulfate in agreement with the previously stated DFT studies. Regeneration of sorbent requires a reducing reagent such as CO or H_2. Observed activation energies for SO_2 reaction were in the order of 4 kcal·mol^{-1}.

According to Cheah et al. factors that affect sorbent retention of activity in hot gas desulfurization are not well understood due to conflicting reports regarding the influence

of surface area retention and pore volume retention [124]. Over zinc-based sorbents, multiple reports attribute their loss of activity to losses of zinc at temperatures exceeding 500^{o}C [165]. At temperatures lower than 500^{o}C, deterioration of activity is also observed despite the difficulty of zinc evaporation at such temperatures [165]. This loss of activity was attributed to ZnO sintering, formation of un-regenerable phase of $ZnSO_4$, and zinc migration to the surface of the sorbent.

Ryu et al. have conducted a series of studies in order to identify causes of activity deterioration over zinc titanate and assess the effect of introducing other metal oxides [165-167]. Introduction of cobalt to zinc titanate resulted into a slight decrease in sorbent activity as compared to pure zinc titanate while performing the sulfidation reaction at 480^{o}C & 650^{o}C and the regeneration at 800^{o}C at atmospheric pressure after 10 cycles [165]. Furthermore, the native zinc titanate sorbent experienced a substantial decrease in pore volume (0.3 $cm^3 \cdot g^{-1}$ to 0.16 $cm^3 \cdot g^{-1}$) after 10 cycles which was not observed in the modified sorbent. In addition, higher surface concentration of zinc was observed as confirmed by XPS measurements in the zinc titanate sorbent (from 9.4 % to 13.5 %). An interesting finding of this study is that the surface area of zinc titanate increased after 10 cycles (from 3.2 $m^2 \cdot g^{-1}$ to 8.9 $m^2 \cdot g^{-1}$). Minimal morphological changes were observed in the cobalt modified sorbent. The observed enhanced stability of the cobalt modified sorbent was attributed to the formation of a mixed $ZnCoTiO_4$ phase which hindered Zn surface migration. Deterioration of the activity of the cobalt modified sorbent was attributed to the formation of sulfate species at low temperatures (480^{o}C), which are difficult to regenerate. Tamhankar et al. studied the activity deterioration of zinc ferrite, copper aluminate, copper ferrite and copper iron aluminates [141]. Sulfidation experiments were conducted at 538^{o}C

and 650°C at atmospheric pressure and sorbent regeneration were performed at 700°C. After several cycles, surface area of the sorbents were found to decrease; for instance in copper aluminates the surface area decreased from 12 $m^2 \cdot g^{-1}$ to 7.0 $m^2 \cdot g^{-1}$ after four cycles at 538°C. Similarly in copper iron aluminates the area decreased from 26 $m^2 \cdot g^{-1}$ to 4.2 $m^2 \cdot g^{-1}$ after 14 cycles at 650°C. Moreover, chemical changes were observed in the studied sorbents. For instance, part of the zinc ferrite transformed to Fe_2O_3 after 6 cycles of regeneration. Fresh copper-iron aluminates sorbent contained CuO, $CuFe_2O_4$ and $FeAl_2O_4$. After 14 adsorption and regeneration cycles, several phases formed including $CuAlO_2$ and α-Al_2O_3. The enhanced stability of copper mixed sorbents was attributed to the stabilization of Cu^{+2} and Cu^{+1} oxidation states. Both oxidation states are highly active towards removal of H_2S as concluded from the their high equilibrium constants ($6.3x10^{17}$ for Cu^{+2} (CuO) and $8.9x10^{8}$ for Cu^{+1} (Cu_2O)) [139]. The reported literature qualitatively identifies causes of activity deterioration. Still, quantified assessment is lacking.

The importance of metal oxide surface area has been confirmed in several reports as in as in the study of Polychronopoulou et al. and Stephanopoulos et al. on which higher capacities were observed in sorbents with higher surface areas [17, 150]. Gibson et al. observed a 20% utilization of ZnO total mass, and attributed that to pore closure via the formation of dense sulfide layer during the adsorption phase [148]. In what seems to be a contradiction to those findings, Ryu et al. observed an increase in the $ZnTiO_2$ surface area with subsequent regenerations coupled with loss of activity [165]. In this case, Ryu et al. attributed the deterioration of activity to factors other than loss of surface area. To affirm the role of surface morphology on the sorbent activity, several studies done on this specific matter are presented.

In the study by Polychronopoulou et al., several mixed oxides sorbents of the metal mix Zn-Fe-Ti-Mn were tested for H_2S adsorption capacity [17]. By varying the molar content of iron in the mix going from 5 to 20 mole %, the surface area decreased from 107 $m^2 \cdot g^{-1}$ to 1.7 $m^2 \cdot g^{-1}$. The decrease in surface area was accompanied with a decrease in the sorbent adsorption capacity towards H_2S going from 2.5 $mmol \cdot g^{-1}$ to 0.5 $mmol \cdot g^{-1}$ when measured at a reaction temperature of 25°C. The variation of the iron content was also accompanied with a variation in the crystalline phases, which can also lead to a variation in the adsorption capacity. In another study by Carnes et al., the activity of nanocrystalline sorbents was benchmarked against conventional sorbents among several metal oxides [168]. The surface area of nanocrystalline Al_2O_3 sorbent was found to be 8 times larger than its conventional counterpart (800 $m^2 \cdot g^{-1}$ vs. 100 $m^2 \cdot g^{-1}$). Similarly, the adsorption capacity of the nanocrystalline sorbent was almost 10 times larger than the conventional sorbent (0.029 vs. 0.003). Similar results were obtained for ZnO, a surface area increase by 6.5 times was accompanied with a capacity increase by 2.5 times. The latter results clearly show a strong correlation between the sorbent surface area and its capacity. From a fundamental perspective, the initial reaction rate is expected to have a direct proportionality relation with surface area of the sorbent.

5.2.3 SELECTION OF THE POTENTIAL ADSORBENT

The review presented in sections 5.2.1 and 5.2.2 elucidates the pros and cons of metal exchanged zeolites and mixed metal oxides towards the adsorption of H_2S and SO_2. Both classes offer decent capacities and complete (sub ppm) removal of H_2S at temperatures relevant to the Claus process. Metal oxides and mixtures thereof offers the highest removal capacity towards both H_2S and SO_2. However, during the adsorption of SO_2 or the

regeneration of the metal oxides after adsorbing H_2S, metal sulfates are formed. The destruction of the metal sulfates necessitate the use of a reducing gas or exposure to temperatures in excess of 873 K in order to achieve complete destruction. Such temperatures enforces of high alloys in the construction of the housing vessels. Metal exchanged zeolites on the other hand offers full regenerability upon adsorbing H_2S at temperatures as low as 623 K thus allowing use of Carbon steel alloys. Still, they suffer from lower capacities (<2.5 $mmol \cdot g^{-1}$) and their adsorption capacity towards SO_2 at Claus tail gas temperatures is unknown. Table 5.2 summarizes the pros and cons of both classes.

Adsorbent Class	Pros	Cons
Metal Exchanged Zeolites	Fully regenerable	Lower capacities SO_2 adsorption is unknown
Mixed Metal oxides	Very high capacities reported Active towards both H_2S and SO_2	Regeneration requires use of reducing gas and/or excessive thermal treatment

Table 5.2/P-142 Comparison between metal exchanged zeolites and mixed metal oxides

I have chosen metal exchanged zeolites as the basis adsorbent for the proposed TGTU for the following reasons:

1) Metal exchanged zeolites can be fully regenerable at relatively low temperatures thus eliminating the need for high thermal resistance alloys which tends to be substantially more expensive than conventional carbon steel.
2) Furthermore, the need for using a reducing gas is eliminated.

Since the adsorption affinity of metal exchanged zeolites towards SO_2 is not known, I suggest the implementation of process concept 2 (TSA+hydrogenation) as opposed to process concept 1 (TSA only). In addition to sulfur species hydrogenation, the catalyst in

the hydrogenation reactor can also catalyze the water-gas shift reaction which leads to significant reduction in the concentration of carbon monoxide (Refer to Chapter 6 for further details). This permits the use of the cheaper adsorbent CuY instead of Ag(I)-Y. Hence, CuY is chosen as the basis for the proposed TGTU unit. While, CuY adsorption equilibrium has been studied extensively, many ambiguity lies in its adsorption and regeneration kinetics and in its material structure. The upcoming section presents the experimental studies conducted on CuY in attempt to elucidate the unresolved ambiguities.

5.3 EXPERIMENTAL ASSESSMENT OF COPPER(I)-Y

This section presents the experimental studies conducted on CuY. The adsorbent was kindly prepared by Dr. Balasubramanian Veerapan whom also performed argon adsorption analysis as to elucidate the porous structure of the material. X-ray Diffraction (XRD) patterns were kindly collected by Mrs. Anjana Tharalaksemy while High Resolution-Transmission Electron Microscopy (HR-TEM), Electron Energy Loss Spectroscopy (EELS), Scanning Electron Microscopy imaging (SEM) and Electron Dispersion Spectroscopy (EDS) and were kindly performed by Dr. Marios S. Katsiotis.

5.3.1 EXPERIMENTAL METHODS

CuY zeolite was prepared by Vapor Phase Ion Exchange method (VPIE) as reported by Crespo et al. [14]. As for parent materials sources, CuCl was purchased from Sigma-Aldrich, USA and used as received without any further purification. Zeolite HY (Zeolyst-CBV 400,Si/Al=2.55) was obtained from Zeolyst International. In a typical synthesis, a U-shaped quartz reactor is loaded with two beds of Copper Chloride and zeolite HY separated

by a thin quartz wool layer. Following, the quartz reactor is placed vertically inside a cylindrical furnace and subjected to thermal treatment under continuous flow of an inert gas. The reactor temperature is increased from room temperature to 200 °C at a rate 1 °C $\cdot min^{-1}$. Then, the temperature is maintained at 200 °C for 5 hours. Following, the temperature is increased at the same rate to 700 °C and maintained for 10 hours. Finally, light green colored Cu exchanged zeolite Y (CuY) is formed. Afterwards, the resulting material is exposed to a continuous flow of air at 350°C. Finally, the adsorbent is sieved to a size range extending between 125 μm and 250 μm as to be utilized for H_2S breakthrough experiments.

The parent material HY and synthesized CuY samples were characterized by XRD, argon adsorption-desorption measurements, SEM, HR-TEM, EDS and EELS techniques. The powder X-ray diffraction (XRD) patterns were collected using a PANAlytical diffractometer (X'Pert PRO) equipped with a Cu-Kα radiation source (θ = 0.15406 nm) for a 2θ range extending between 10 and 70° at an angular rate of $0.02° \cdot s^{-1}$. The argon sorption analysis was carried out in Autosorb-iQ manufactured by Quantachrome Instruments at the liquid Ar temperature of 87 K. The adsorbent was outgassed at 250 °C for 6 h prior to analysis.

Specimens for SEM analysis were prepared by depositing approximately 3mg of specimen powder loaded on standard aluminum stabs using conductive carbon tape. SEM analysis was conducted on an FEI Quanta 250 (FEG) at 20kV, coupled with EDAX Energy Dispersion X-ray Spectrometer (EDS). Specimens for TEM characterization were prepared by depositing approximately 3mg of powder on a standard Ni grid covered with thin layer

of amorphous carbon (lacey carbon). TEM analysis was performed with an FEI Tecnai G20 (200kV) equipped with the following: an EDAX EDS unit; a Gatan GIF 963 post-column energy filtered camera (0.9 eV energy resolution full width at half maximum at zero loss peak); and an FEI High Angle Annular Dark Field Scanning TEM detector (HAADF-STEM). For a typical experiment the sample would be inserted immediately following preparation in order to avoid contamination. The morphology of the specimen was identified by STEM imaging; initially the grid surface was scanned at low magnification followed by image acquisition at higher magnifications. It should be noted that owning to low beam intensity at STEM mode ($<100e^{-}/nm^{2}$), no specimen damage was observed due to beam degradation. EDS spectra and elemental maps were collected in addition to EELS spectra at selected locations.

The schematic of breakthrough rig is depicted in Figure 5.2. The breakthrough rig was constructed using ¼ inch SS-316 tubing, fittings and valves from Swagelok™. Gases flow-rates were controlled by Mass Flow Controllers (MFCs) supplied by Brooks™. Calibration of the MFCs was conducted prior to every breakthrough and regeneration experiment using bubble flow meter measurements as the benchmark.

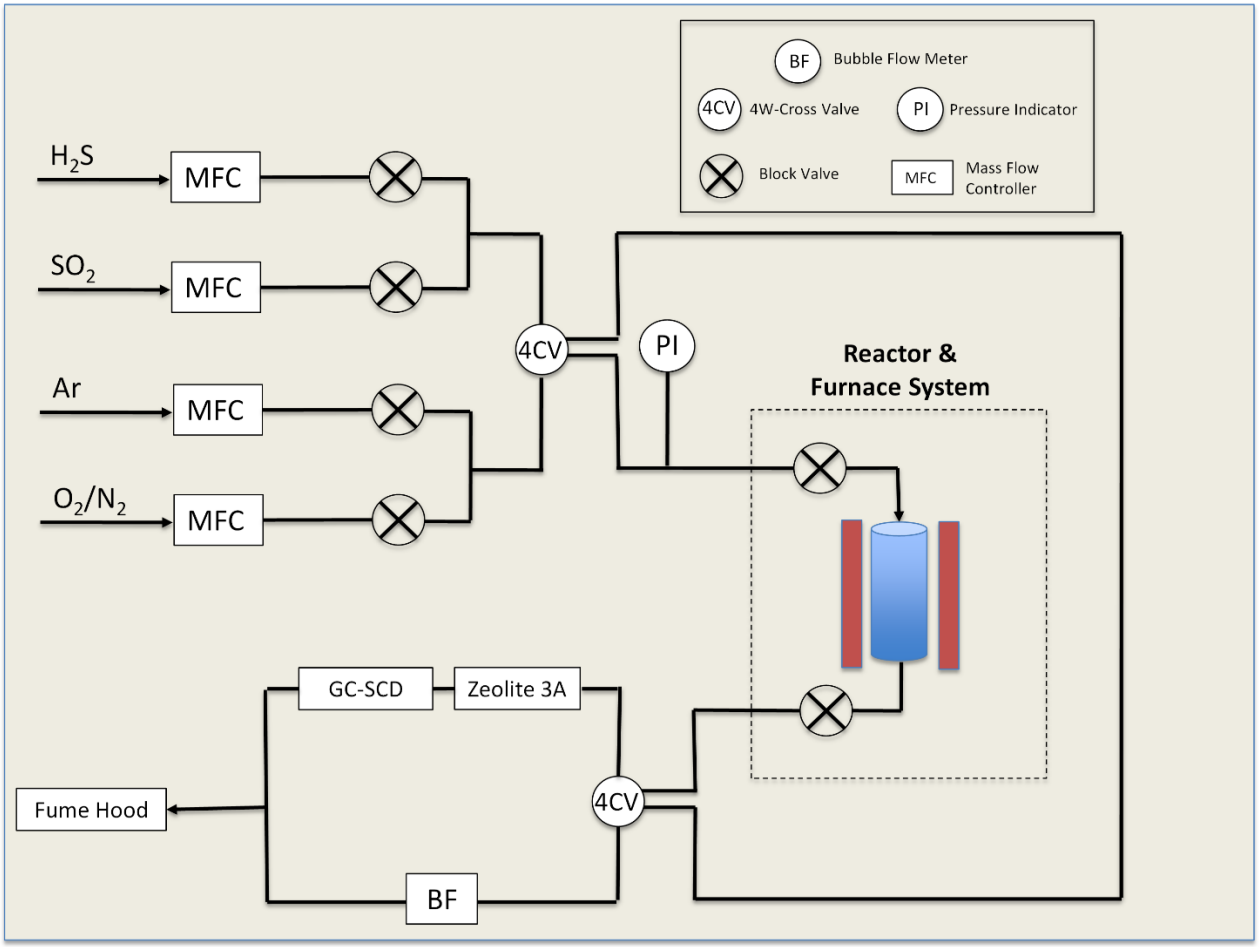

Figure 5.2/P-146 Schematic of the Breakthrough System

The H_2S adsorption experiments were carried out in a fixed bed U-shaped quartz reactor having 4 mm internal diameter. The test bed was made by mixing 15 mgs of adsorbent with 300 mgs of quartz particles as diluent both sieved to sizes extending between 125 and 250 μm. The mixture was then loaded inside the reactor while being sandwiched between two layers of quartz wool. It was confirmed that the quartz particles and the quartz wool do not adsorb H_2S under the experimental conditions of interest. The sample (sorbent+diluent mix) received was already pre-packed and undergone four cycles of adsorption and regeneration using the conditions stated below but at an adsorption temperature of 150ºC. Adsorbent pre-treatment was done prior to every experiment in order to remove adsorbed water and organics. The test bed was kept at 300°C for 12 hours under 50 $ml \cdot min^{-1}$ flow of Argon (supplied by Arabian Industrial Gases, 99.9992% purity). Following, the bed was exposed to an H_2S bearing gas stream containing 102 ppm H_2S with the balance being helium (Supplied by Air products™) at 150°C and at atmospheric pressure kept at a flow rate of 42 $ml \cdot min^{-1}$.

Effluents from the reactor were passed first through 150 mg zeolite 3A bed in order to remove water prior to being analyzed using a PerkinElmer Clarus 580 GC - Model Arnel 4025PPC and Model Arnel 4016PPC Sulfur Chemiluminescence Detector (SCD). The zeolite 3A bed was confirmed experimentally to be sterile towards H_2S adsorption. After confirmation of the occurrence of breakthrough and complete cleaning of the GC line from H_2S, the sample was exposed to a regeneration stream composed of 5% O_2 in a balance of N_2 at a rate of 50 $ml \cdot min^{-1}$. The temperature was retained at the adsorption temperature for 40 minutes. Following, the temperature was raised in 50ºC increments up to 400ºC. At

each increment increase the sample was retained for a period of 40 minutes. Effluents during regeneration were continuously analyzed via the same GC-SCD instrument.

After passage of 20 hours of exposure to the regeneration stream, the temperature of the sample was reduced down to the next adsorption while still being exposed to the regeneration gas. Once the sample temperature reached target temperature, a stream of argon was introduced at a rate of 50 $ml \cdot min^{-1}$ in order to evacuate all remaining traces of the regeneration gas. Meanwhile, the water adsorbing zeolite 3A bed is replaced with a fresh one. The process detailed above was repeated for four additional target temperatures (180ºC, 210ºC, 240ºC, 150ºC); hence reaching a total of five adsorption-regeneration cycles. In another breakthrough/regeneration experiment, a fresh bed underwent the same procedure described above for a single adsorption temperature of 150ºC. Following, the bed was regenerated using argon only.

5.3.2 EXPERIMENTAL RESULTS & DISCUSSION

The XRD patterns of HY and CuY are depicted in Figure 5.3. All the patterns in both samples are attributable to the zeolite HY structure, indicating the structure is intact in CuY even after ion-exchange. In addition, no change in the peak intensity and position was observed for CuY which further confirm that the crystallinity and structure are retained after VPIE. Figure 5.4 displays the argon adsorption isotherm for HY and CuY and the corresponding $NLDFT_{ads}$ pore size distribution plots are exhibited in Figure 5.5. Both HY and CuY adsorption isotherms are of Type I, which is the characteristic for microporous materials demonstrating that both the adsorbents are microporous zeolites and no mesoporosity exists in the adsorbents. Brunauer–Emmett–Teller (BET) surface area is

deduced from the adsorption branch of the isotherms and the values are 748 and 577 $m^2 \cdot g^{-1}$ for HY and CuY respectively. The pore diameter (7.55 Å) remains intact after ionic exchange as evidenced by the NLDFT analysis. However, minor decrease in pore volume is observed in the case of CuY which can be attributed to filling of the pore volume with the larger Copper atom.

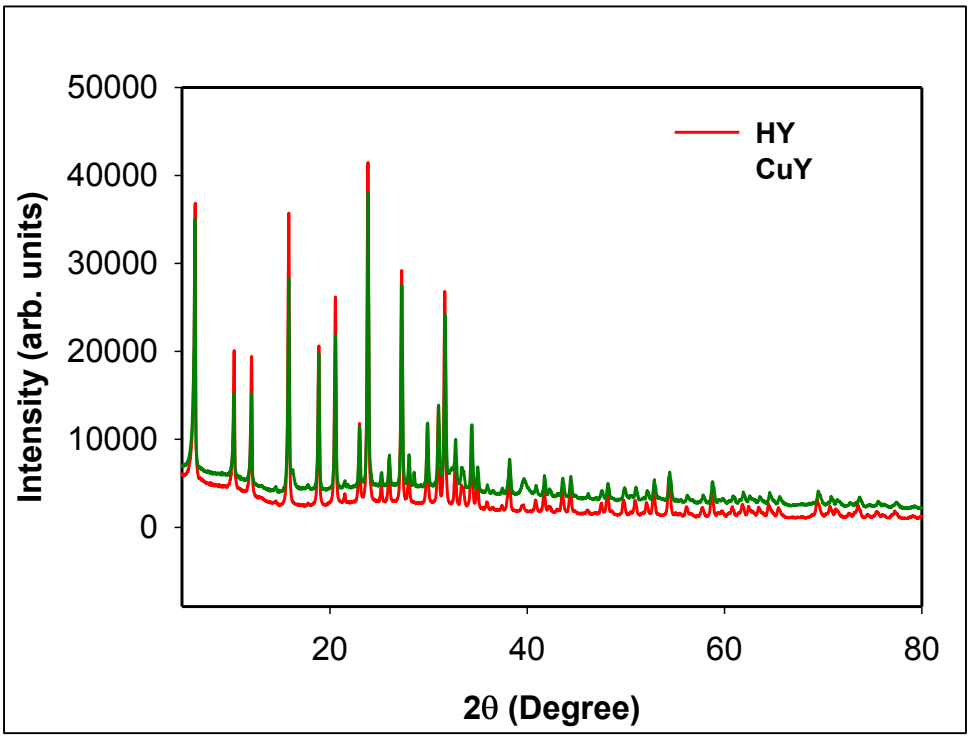

Figure 5.3/P-149 XRD patterns of HY and CuY

Figure 5.6 displays the SEM images of HY and CuY adsorbents. The prominent morphology observed is the standard octahedral attributed to zeolite Y particles. Both HY and CuY possesses the same morphology thus providing further evidence to the retention of the zeolite Y structure upon vapor phase ionic exchange.

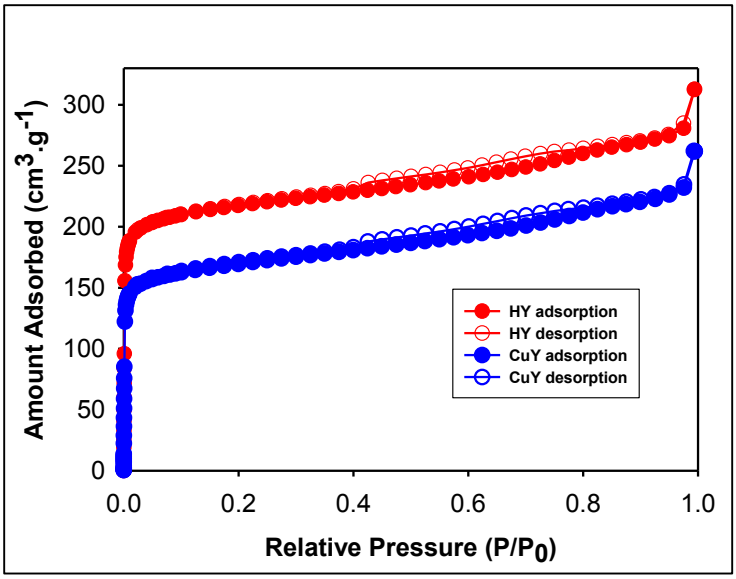

Figure 5.4/P-150 Ar adsorption-desorption isotherms of HY and CuY

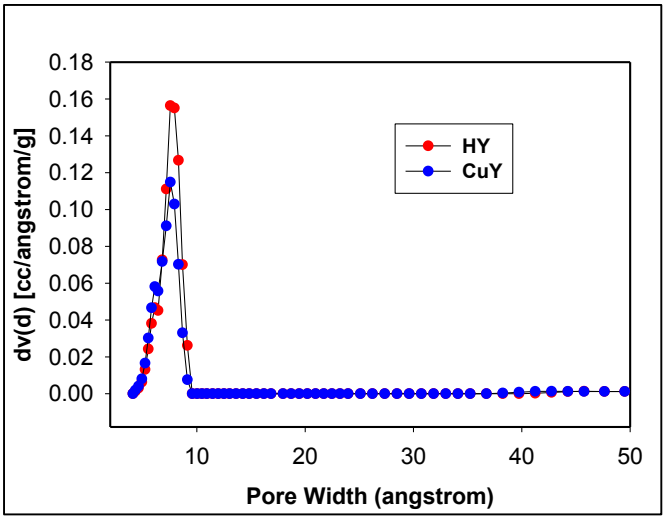

Figure 5.5/P-150 NLDFT$_{ads}$ pore size distribution plots for HY and CuY adsorbents

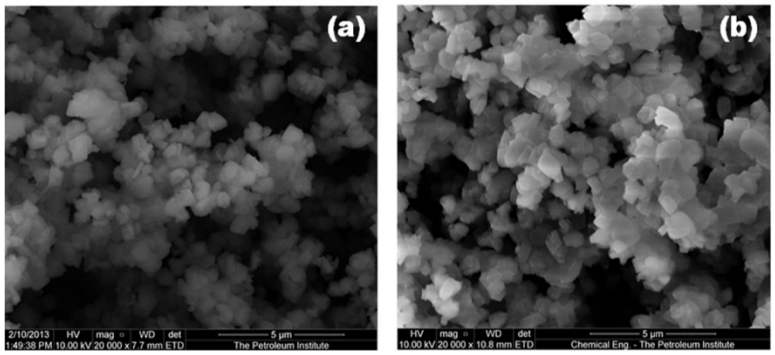

Figure 5.6/P-151 SEM images of (a) HY and (b) CuY

STEM imaging results (Figure 5.7) further confirms that the zeolite particles are uniform in shape and size. The content of copper is found to average at 9.0% weight with SEM-EDS and TEM-EDS. The majority of Copper appears to form agglomerated nanoparticles, dispersed over the surface of the zeolite Y particles, as confirmed with EDS elemental mapping (see Figure 5.8).

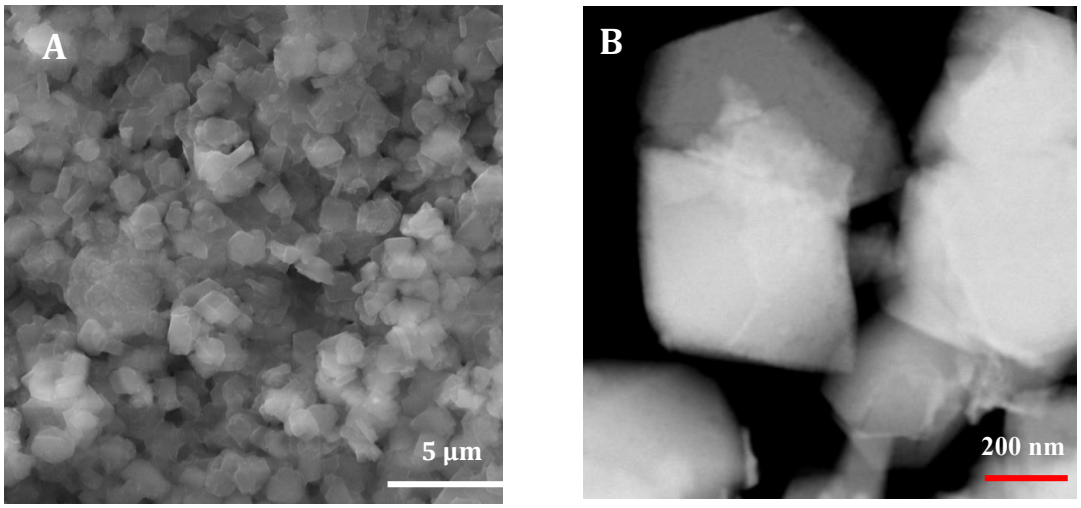

Figure 5.7/P-151 SEM (A) and STEM (B) images of CuY

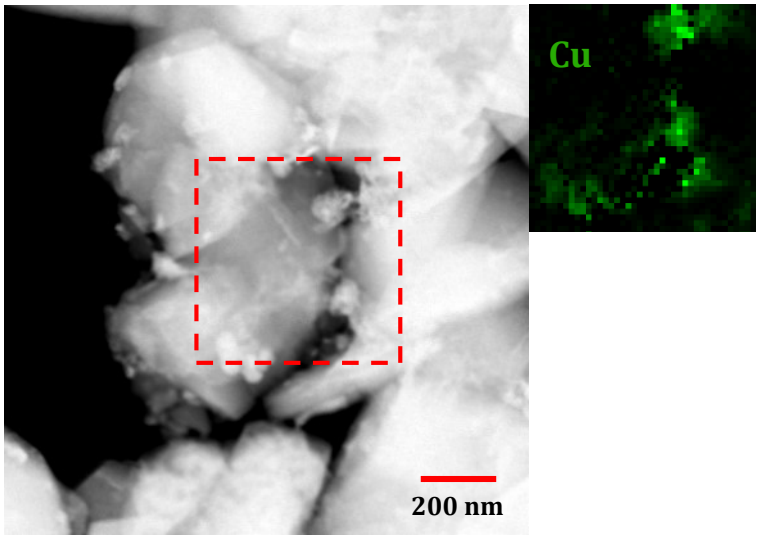

Figure 5.8/P-152 CuO nanoparticles on zeolite Y surface; inset: STEM EDS mapping of Cu on the selected area (red rectangle)

In addition, HR-TEM and EELS confirm the nature of the particles to be copper oxide (CuO). Specifically, EELS spectra collected in STEM mode by targeting copper agglomerations deposited on zeolite particles, exhibit the characteristic transitions associated with CuO. The typical structure for CuO is shown in Figure 5.10, where the oxygen K edge is seen at ~539eV, along with the copper L2 and L3 edges at 951 and 931 eV respectively [169, 170]. The insets at Figure 5.10 contain the background corrected and deconvoluted (at zero loss) spectra for O and Cu edges. HRTEM imaging from the same locations reveals d-spacings associated with CuO. The Fast Fourier Transform of Figure 5.9 presents strong diffraction from the [-1 1 0] plane.

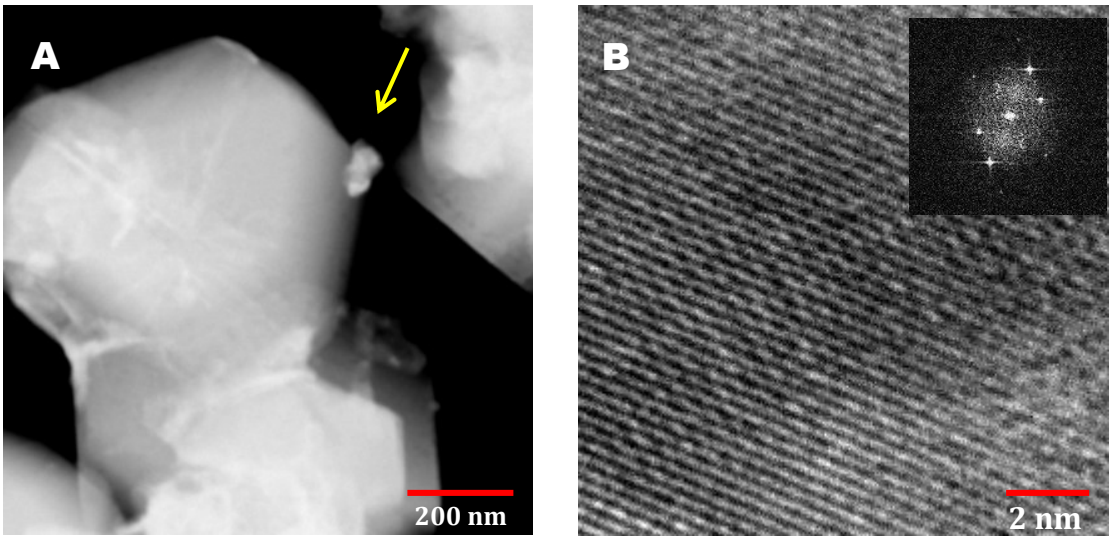

Figure 5.9/P-153 STEM image of CuO nanoparticles on zeolite Y (depicted with yellow arrow), B: HRTEM image of CuO nanoparticle deposited on zeolite Y (inset: Fast Fourier Transform)

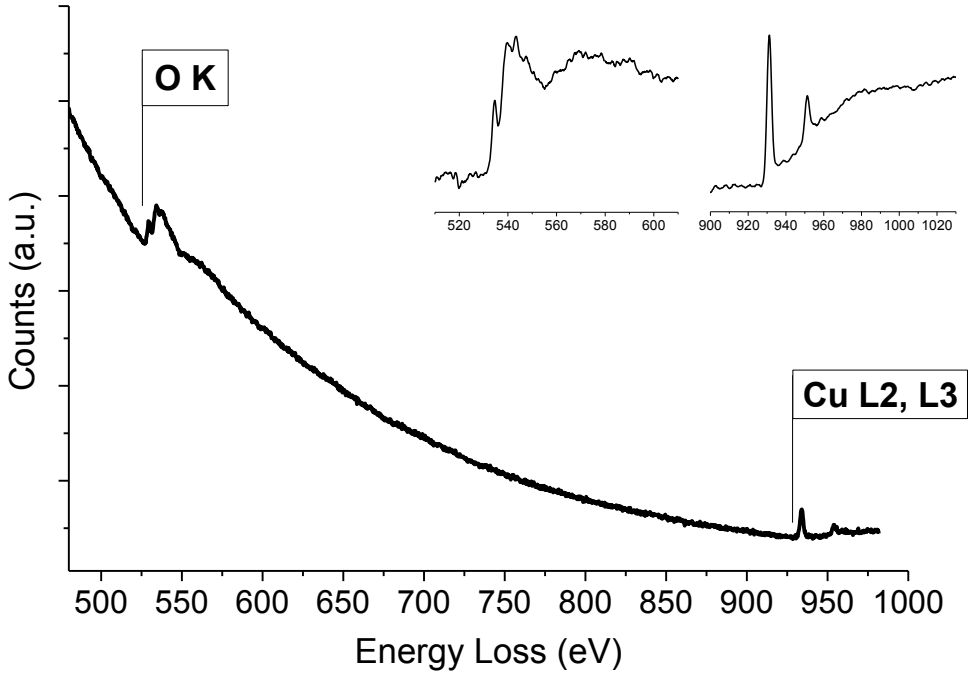

Figure 5.10/P-153 EELS spectrum of CuO nanoparticle (left inset: oxygen K edge – right inset Cu L2 & L3 edges)

The initial H_2S breakthrough experiments for CuY were carried out by Dr. Balasubramanian at University of Minnesota by loading 15 mg of adsorbent diluted with

300 mg quartz in a U-shaped quartz reactor. The H_2S adsorption study was carried out using 102 ppm H_2S in Helium at 150 °C and the regeneration of the adsorbent was carried out at 400 °C using 5% O_2 in N_2. The resulting H_2S breakthrough curves are presented in Figure 5.11. CuY adsorbent demonstrates stable sulfur capacity of ~ 1 $mmol \cdot g^{-1}$ after two adsorption/regeneration cycles.

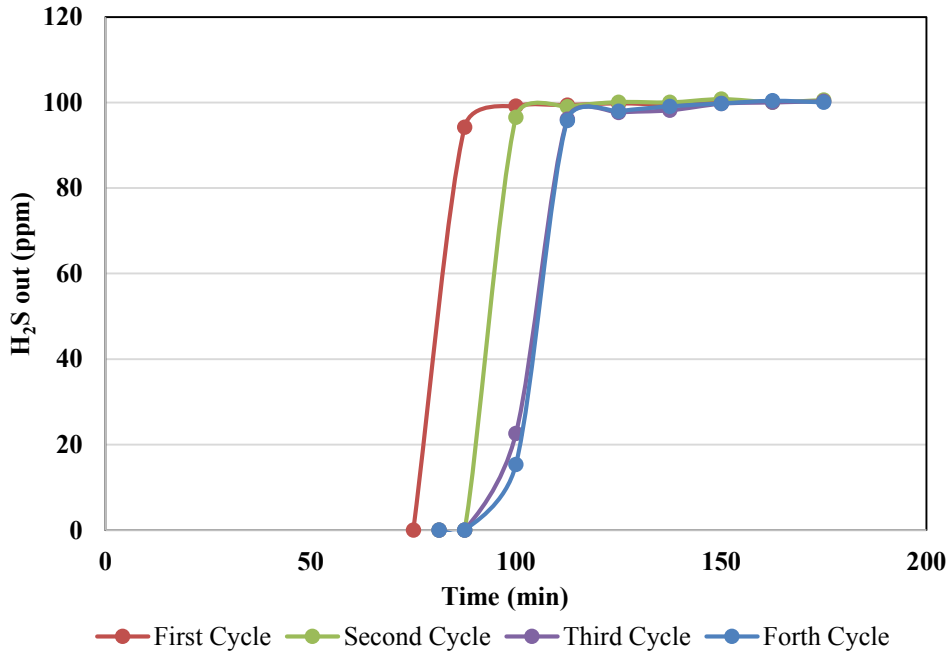

Figure 5.11/P-154 Initial Breakthrough curves of CuY

Results of the adsorption/regeneration cycling performed at various temperatures are presented in Figure 5.12. During regeneration, SO_2 is released most probably formed due to the combustion of H_2S released during regeneration. Clearly the adsorbent is fully regenerable as evidenced by the retention of the adsorbent capacity upon cycling. Furthermore, the capacity increases with increasing temperature. This result is in agreement with the one reported by Kumar et al. [15]. The explaining hypothesis is that during the vapor exchange process, a substantial segment of the copper accumulates thus forming agglomerates of copper nanoparticles dispersed over the zeolite surface. Upon

calcination the particles are oxidized thus forming copper oxide. The reaction of H_2S with copper oxide is kinetically limited hence increasing the temperature leads to an increase in the observed capacity up to the point after which the copper oxide is completely transformed to copper sulfide during adsorption at which capacity ceases from increasing. Evidences from TEM-EDS mapping and EELS spectra presented earlier supports that hypothesis.

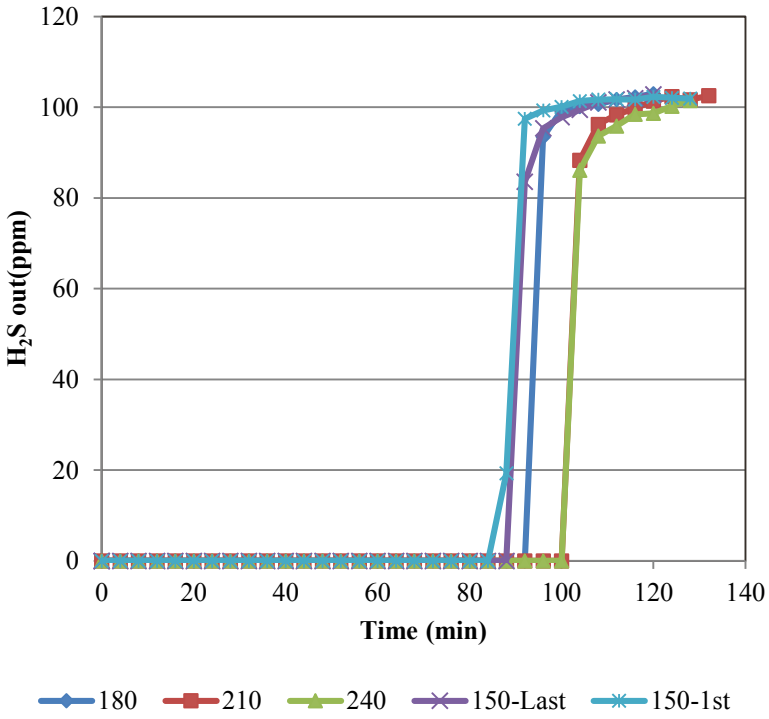

Figure 5.12/P-155 Breakthrough curves for each cycle

Cycle	T (°C)	Capacity	SO_2 out during ads
5	150	1.03	0.000
6	180	1.12	0.059
7	210	1.20	0.368
8	240	1.20	0.795
9	150	1.03	0.002

Table 5.3/P-155 Capacity and SO_2 released for cycles conducted all in $mmol \cdot g^{-1}$

Eluding species time profile during regeneration for the cases of 150°C is shown in Figures 5.13. Data collected during regeneration was not found to be adequate for the cases of 210°C and 240°C adsorption due to the relatively long GC-SCD injection time (4 minutes). In other words, the regeneration kinetics are faster than the resolution of the GC-SCD system thus preventing it from accurately capturing the regeneration curves. SO_2 is the only eluding species during adsorbent regeneration. This can be attributed to the combustion of H_2S once released from the adsorbed state and the re-oxidation of the copper sulfide to copper oxide thus releasing SO_2.

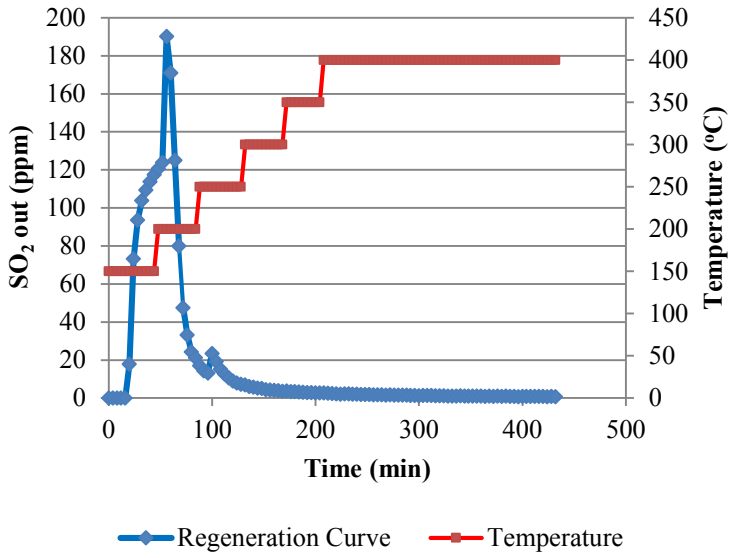

Figure 5.13/P-156 Regeneration Curve of CuY for the 150°C adsorption temperature case

At temperatures higher than 150°C, SO_2 is released during adsorption as presented in Figure 5.14. This can be attributed to the re-adsorption of SO_2 during regeneration and subsequent release upon displacement with H_2S. Apparently this process is favored at higher temperatures. Table 5.3 presents the computed capacities and released SO_2 for each case.

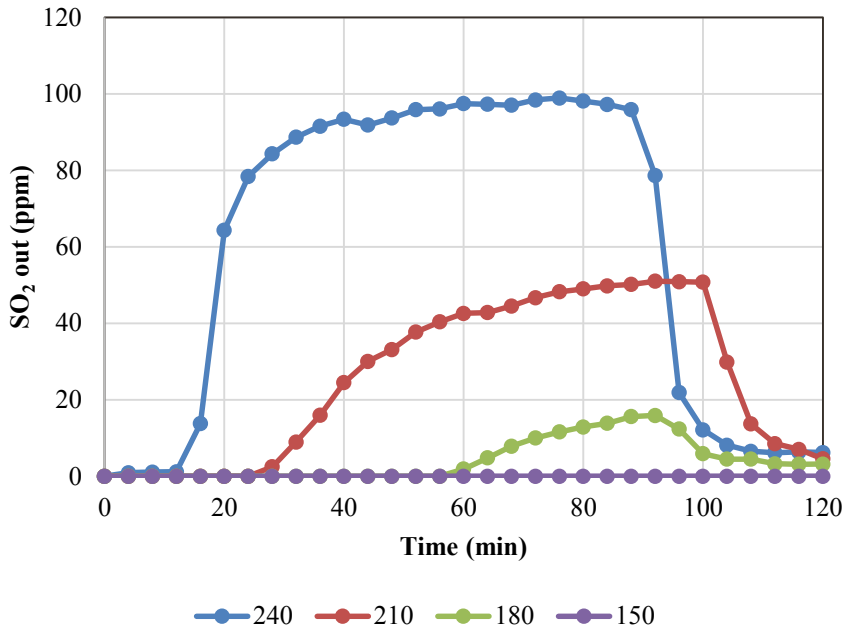

Figure 5.14/P-157 SO_2 released during adsorption cycles

A question arises on whether the copper oxide nanoparticles are the only contributor to the adsorption capacity. To resolve this issue, a fresh adsorbent bed mix underwent the same adsorption procedure at 150°C. The regeneration was performed using high purity argon instead of the typical oxidizing stream used (5% O_2 in N_2) following the same protocol detailed above. It is expected that the regeneration of copper sulfide can only be accomplished via an oxidizing stream and hence will lead to the formation of SO_2 during regeneration. If H_2S is released during regeneration, then this accounts as a compelling evidence for the existence of extra-framework copper ions which exchanged the original protons in the extra-framework positions. These ions do contribute to the overall capacity of the adsorbent. Figure 5.15 presents the regeneration profiles for the argon regenerated adsorbent. Clearly, H_2S is released during the early stages of the regeneration hence confirming the contribution of the extra-framework copper ions to the adsorption capacity. Astonishingly, SO_2 is also released but at later stages of the regeneration. Expected sources

for the release of SO_2 is reaction of H_2S with adsorbed oxygenated species which can either form during the calcination preparation step of the adsorbent or form via the dissociative adsorption of water during the adsorption since water is released upon the reaction of H_2S with CuO.

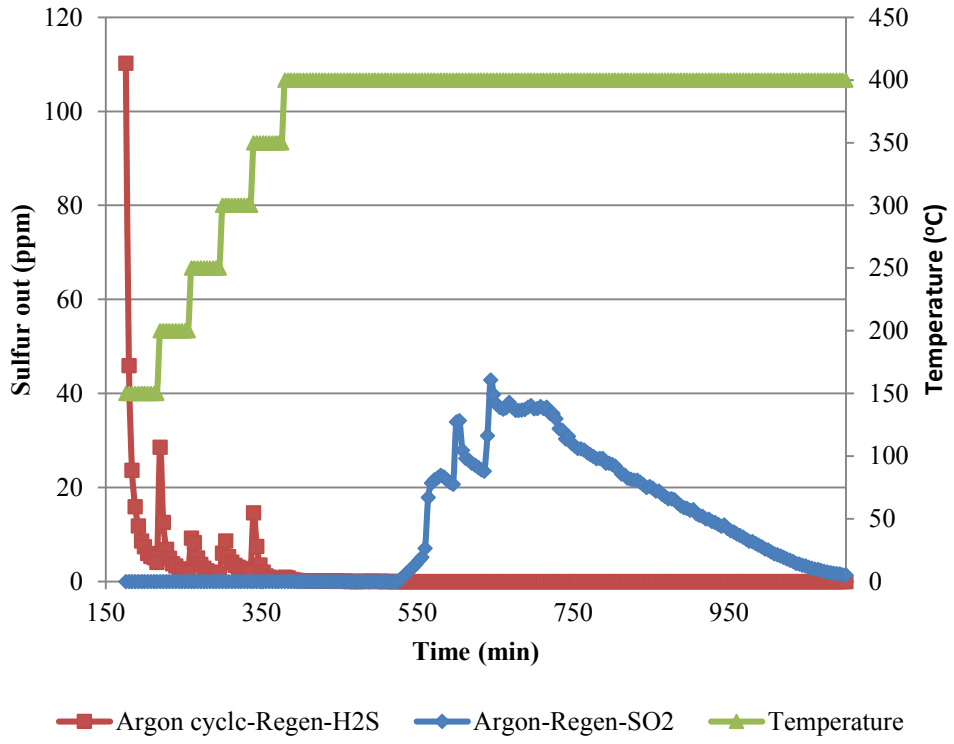

Figure 5.15/P-158 H_2S and SO_2 released during regeneration with Argon

In conclusion, the preferred operating conditions for the adsorbent are 150°C adsorption temperature since it eliminates the release of SO_2 during adsorption; a detrimental factor to the targeted TGTU recovery. Furthermore, the adsorbent is capable of achieving practically 100% recovery as evidenced by absence of any detectable sulfur species released during adsorption considering the SCD detector sensitivity limit of 50 ppb.

5.3.3 KINETIC MODELING

This section presents the results of fitting the regeneration experimental data for the 150oC adsorption case. A Partial Differential (PDE) model is presented herein targeting the modeling of the adsorption-regeneration experiments. The model utilizes Langmuir adsorption isotherm as the basis for modeling the adsorption thermodynamics. Mass transfer effects are introduced to the model via the generally accepted linear driving force. The following assumptions are invoked:

1) No accumulation of gas phase species.
2) Isothermal adsorption and regeneration. The regeneration temperature in the model is changed in a step like approach thus replicating the experimental conditions. During each step the regeneration is assumed isothermal.
3) Temperature dependency of the equilibrium constant for regeneration K_{reg} (since SO_2 is released not H_2S, a different equilibrium constant has to be used) is Arrhenius like i.e. (K_{reg} (T) = K_{reg} * exp (-1*ΔH_{ads} /RT)).
4) The saturation capacity is assumed to be independent from temperature.
5) The gas phase diffusion coefficient, particle radius and internal diffusion coefficient for regeneration are different from those of adsorption.

The governing equations of the models are as follows:

- Species Mass Balance in the bulk phase:

$$u\frac{\partial(C_i)}{\partial z}+\frac{1-\varepsilon_b}{\varepsilon_b}\frac{\partial q_i^*}{\partial t}=0$$

where *u* is the Interstitial velocity of the fluid, C_i is species i gas phase concentration, q_i^* is the concentration of species as an adsorbed phase in mole·m^{-3} solid, ε_b is the bed porosity, z is the axial dimension and t is the time. The initial and boundary conditions are:

$$C_i(t=0,z)=C_{i,ini} \quad C_i(t,z=0)=C_i^{BC} \quad \text{(5.2 a,b)}$$

where C_i^{BC} is the H_2S concentration at the inlet of the bed. The bed is assumed to be initially free of H_2S.

- Linear Driving Force formulation:

$$\frac{\partial q_i^*}{\partial t}=k_{mass,i}\left(q_i-q_i^*\right) \quad \text{(5.3)}$$

where q_i is the equilibrium concentration of the adsorbed phase in mole·m^{-3} solid, $k_{mass,i}$ is the overall mass transfer coefficient.

- Overall mass transfer coefficient given by [26]**:**

$$\frac{1}{k_{mass,i}}=\frac{q_i}{k_{fi}\rho_g a_P y_i}+\frac{R_P}{5D_{ei}a_P\left(\frac{T}{423}\right)^{1.7}} \quad \text{(5.4)}$$

Where k_{fi} is the film mass transfer coefficient, ρ_g is the gas density, a_P is the outer surface area of sorbent pellets per unit volume of bed, D_{ei} is the species i diffusion coefficient within the pellet, T is the temperature in Kelvin, R_p is the radius of the pellet. The temperature correction herein assumes that the diffusion coefficient dependency on temperatrue imitate that of gas phase diffusion coefifient.

- Film mass transfer coefficient is [74]:

$$k_{fi}=\frac{0.357}{\varepsilon_b}\mathrm{Re}^{0.64}\,Sc_i^{033}\,\frac{D_{m,i}\left(\frac{T}{423}\right)^{1.7}}{2R_P} \quad \text{(5.6)}$$

where, Re is the Reynolds number, Sc_i is the Schmidt number of species I, $D_{m,i}$ is the molecular diffusion coefficient of species i.

- Adsorption isotherm given by the extended Langmuir adsorption isotherm:

$$q_i = \frac{K_{i,ads} \exp\left(\frac{\Delta H_i}{R}\left(\frac{1}{T} - \frac{1}{423}\right)\right) q_i^s C_i}{1 + \sum_{i=1}^{Nu} K_{i,ads} \exp\left(\frac{\Delta H_i}{R}\left(\frac{1}{T} - \frac{1}{423}\right)\right) C_i} \quad \text{(5.7 a) for adsorption}$$

$$q_i = \frac{K_{i,reg} \exp\left(\frac{\Delta H_i}{R}\left(\frac{1}{T} - \frac{1}{423}\right)\right) q_i^s C_i}{1 + \sum_{i=1}^{Nu} K_{i,reg} \exp\left(\frac{\Delta H_i}{R}\left(\frac{1}{T} - \frac{1}{423}\right)\right) C_i} \quad \text{(5.7 b) for regeneration}$$

During adsorption only H_2S is the relevant species while during regeneration SO_2 is the relevant species. Breakthrough curves obtained through studied the temperatrue range are fitted via the model described previously. The observed sharpness of the breakthrough curves suggests absence of mass transfer limitations during adsorption. If mass transfer limitations are assumed to be absent, the single component Langmuir adsorption model has a direct analytical solution given by: $t = \frac{L}{u}(1 + \frac{1-e}{e}\frac{K_{ads}Q_{ads}}{1+K_{ads}C_i})$ [30]. Table 5.4 presents the results of adsorption curve fits from the model and the analytical solution. Clearly, a close agreement is found between both models thus suggesting absence of mass transfer limitations during the adsorption step. Once again we observe that the equilibirum constant and the saturation capacity appears to be increasing with temperature which was explained earlier.

	PDE Model		Analytical Solution	
Temperature (°C)	**K_{ads}** ($m^3 \cdot mol^{-1}$)	**$Q_{s,ads}$** ($mol \cdot kg^{-1}$)	**K_{ads}** ($m^3 \cdot mol^{-1}$)	**$Q_{s,ads}$** ($mol \cdot kg^{-1}$)

150	1636	2168	1516	2040
180	3252	2045	3234	2040
210	15803	2040	15802	2040

Table 5.4/P-162 K_{ads} and $Q_{s,ads}$ determined via the PDE model and the Analytical solution

Table 5.4 presents best fits for the adsorption constant and saturation capacities for the adsorption step. The regeneration experiments results conducted at 150ºC were fitted with the same PDE model via gPROMS 3.7 parameter fitting module. Fitting parameters that achieve the best fit for the conducted experiment are listed in Table 5.5. Figure 5.16 presents the model vs. experimental data time profiles.

Parameter	Avg
$D_{ei,reg}$ **(m^2/s)**	1.15E-10±7.6E-11
H_{ads} **(kJ/mole)**	31.5982 ± 2.0
$K_{reg,o}$ **(m^3/mole)**	19.60835 ±1.8
Q_s **(mole/m^3 solid)**	2168 ± 17
Q_{sreg} **(mole/m^3 solid)**	2020 ± 389
R_{preg} **(m)**	6.25E-04 ± 2.35E-05

Table 5.5/P-162 Best fit parameters generated

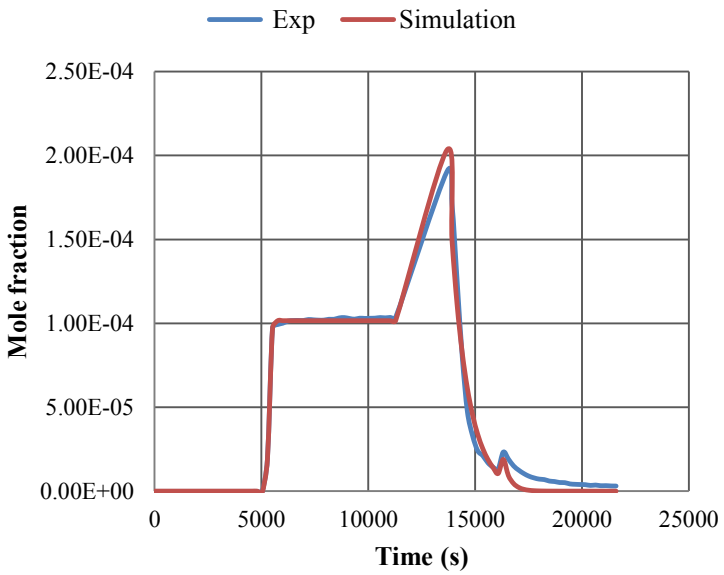

Figure 5.16/P-163 Experimental data vs. simulation results of the best fit for the 150°C adsorption /regeneration cycle

5.4 CONCLUSIONS

This chapter presented a review of adsorbents which have the potential to be used in the proposed TGTU. The adsorbent of choice CuY displayed satisfactory capacities at the target adsorption temperature of 150°C and outstanding regenerability proven over 9 adsorption/regeneration cycles. The cycle results were fitted using a PDE based upon the linear driving force assumption. Once compiled with the optimization protocol presented in chapter 4, the algorithm is now ready to assess the proposed TGTU technology in a real industrial case. This is the topic of the upcoming chapter.

CHAPTER 6: IMPLEMENTATION ON AN INDUSTRIAL CASE[7]

6.1 INTRODUCTION

The chapters presented thus far aimed at laying down the foundation for the utilization of the optimization protocol in the economic assessment of the adsorption based TGTU technology based on an industrial case. The modeling tools have been presented in Chapter 3, while optimization protocol and properties of selected adsorbent have been presented in Chapters 4 & 5 respectively; thus, all of the jigsaw pieces have been put together herein. The case study presented in this thesis pertains to the GASCO plant which employs a CBA unit for secondary recovery of sulfur. Due to the sensitivity of the hydrogenation catalyst towards presence of oxygen in the feed stream (a condition that can be easily produced in a Super Claus unit), ADGAS case was not considered. Furthermore, only process concept 1 is considered herein due to the inability of identifying a regenerable adsorbent active towards both H_2S and SO_2. I begin by stating the case study inputs. Following, the results of the case study are shown and are discussed within the context of economic feasibility. Finally I end the chapter with a detailed analysis of simulations conducted on the optimal solutions identified.

[7] Significant segments of this chapter are published in (Al Wahedi et al., Chem Eng. Sci., 2014). License for reproduction in thesis was obtained under the number 3550021329985.

6.2 CASE STUDY INPUTS & RESULTS

6.2.1 CASE STUDY INPUTS

The model described in Chapter 4 is implemented on GASCO SRU which relies on the conventional Claus process coupled with Cold Bed Adsorption technology (CBA) for a targeted SC of 99.5% .The TGTU unit is proposed to be situated downstream the CBA unit. Table 6.1 summarizes feed streams composition, flows and conditions. The TSA feed gas, i.e. the effluent gas from the hydrogenation system, is computed using standard Gibbs minimization algorithms. As for the adsorbent, three species are of interest. Carbon monoxide is known to compete with H_2S on adsorption sites over Cu(I)-Y [15]. Hence, it has to be considered in the model. Furthermore, H_2S combustion due to the presence of oxygen during regeneration leads to the formation of SO_2. Herein we assume the combustion reaction to be instantaneous and complete. As a result, SO_2 and CO are the relevant species to be considered in regeneration modeling. Table 6.2 presents the adsorption properties of Cu(I)-Y towards H_2S, CO and SO_2. Adsorption properties towards CO were computed based on data reported by Yun et al. [172], while the adsorption properties of H_2S and SO_2 over Cu(I)-Y were determined experimentally as shown in Chapter 5. Lumped diffusion coefficient of CO was computed using the value obtained experimentally for SO_2 assuming that the diffusion coefficient is inversely proportional to the square root of the molecular weight. Several simulations conducted have shown that the adsorption step can be assumed to occur isothermally due to the dilute content of the H_2S in the feed stream. Hence, the value of the heat of adsorption for H_2S is not required. Other model inputs are as per the ones stated in Chapter 4.

Category	TGTU Feed Gas	TSA Feed Gas
Temperature (°C)	127	240
Pressure (kPa)	130	120
Molar Flow (kmol·h^{-1})	3451	3451
Hydrogen (kmol·h^{-1})	52.39	78.69
Water (kmol·h^{-1})	1094.56	1065.99
CO (kmol·h^{-1})	30.12	0.43
N_2 (kmol·h^{-1})	1689.39	1689.8
CO_2 (kmol·h^{-1})	580.6	611.26
H_2S (kmol·h^{-1})	2.27	4.83
SO_2 (kmol·h^{-1})	1.14	0
COS (kmol·h^{-1})	0.2	0
CS_2 (kmol·h^{-1})	0.61	0

Table 6.1/P-166 Processed feeds specifications

Category	H_2S	CO	SO_2
Capacity (mol·m^{-3} solid)	2168	1683	2019
Adsorption Equilibrium Constant at 150°C (m^3· mol^{-1})	1534	3.73	19.6
Heat of adsorption (kJ·mol^{-1})	-	60.0	31.6
Lumped Diffusion Coefficient $D_{e,i}$ at 150°C (m^2·s^{-1})	1.58E-10	1.74E-10	1.15E-10

Table 6.2/P-166 Adsorption properties of Cu(I)-Y towards H_2S, SO_2 and CO

6.2.2 OPTIMIZATION PROTOCOL

In this study, the source of the NPW discontinuities stems from the bed replacement element, which introduces cost cash flows at distinct points in the NPW function. The time instants at which bed replacement is ensued are strongly dependent on the total cycle time. The exact timing at which bed replacement is due is given by the bed replacement period f :

$$f = \text{int}\left(\frac{N_R \cdot t_{ads}}{4380}\right) \quad (4.27)$$

where the function **int** rounds the result of the expression within the brackets to the nearest integer. Clearly, slight changes in the adsorption time cycle t_{ads} can lead to significant changes in the value of f, which in turn significantly affect the NPW function as suggested

by expression (1). To overcome these difficulties, we propose a dual step approach for arriving at the optimal solution. In the first step, the governing model is recast from its PDE form into a set of nonlinear algebraic equations and a first approximation of the optimal solution is found, through the following protocol:

1) The adsorption step is assumed to be isothermal hence eliminating the need for simultaneous solution of the energy balances.
2) To avoid finding the breakthrough time by solving the set of PDEs described earlier at each step of the optimization algorithm, this set is substituted by the equilibrium based analytical solution for the breakthrough time as described in [30]. An efficiency factor is introduced in order to account for mass transfer effects.

In order to obtain the workable form of the efficiency factors, breakthrough times were computed for bed lengths from varying from 3 to 10 m, for bed diameters from 1 to 5 m and for a total number of vessels ranging from 2 to 8. Regeneration times were obtained for the same length and diameter ranges, however for regeneration gas flows ranging from 275 to 1100 kmol·h^{-1} per vessel. Those ranges were found to encompass the space of optimum decisions variables for the cases under study. The total number of data points regressed were 193 for adsorption cycle and 80 for regeneration cycles. The following empirical form was found to provide good fit of the obtained data for adsorption and regeneration cases:

$$\zeta_h = \frac{X_1 \cdot X_2 \cdot \left(\frac{L}{U_f / \varepsilon_b} - X_3 \right)^{X_4} \cdot L^{X_5}}{1 + X_2 \cdot \left(\frac{L}{U_f / \varepsilon_b} - X_3 \right)^{X_4}} \qquad (6.1)$$

where X_1 to X_5 are fitting parameters, Table 6.3 presents the fitting parameters values. Overall, average correlation deviations from simulated times fall below 15%.

Parameter	Adsorption	Regeneration
X1	0.628	0.877
X2	0.395	1.398
X3	-0.775	0
X4	1.16	1.145
X5	0.436	0.123
Mean Error	13.6%	2.0%

Table 6.3/P-168 Fitting parameters for mass transfer efficiency factors

Other steps are described in Chapter 4.

6.2.3 IMPLEMENTATION OF THE OPTIMIZATION APPROACH - MAXIMUM ALLOWABLE PRESSURE DROP

Here, we probe the variation of the calculated optimal value of NPW and its elements for three different maximum allowed values of pressure drop, 10, 15, and 20 kPa, and a fixed maximum footprint of 250 m^2. The optimal solutions obtained via the first step of the optimization approach are compared to those obtained from the final solution. Table 6.4 shows the results for both approaches while Figure 6.1 presents the corresponding values of NPW and its elements. The computational time in Case 1 for the first step is 1944 s while for the second step is 252s performed over Intel™ Xeon™ CPU E5-2609 clocked at 2.40 GHz. Similar times are obtained for the rest of the cases. Clearly, both approaches lead to similar values of NPW. This signifies the accuracy of the first step protocol in arriving to an order of magnitude estimate of the optimal design. Furthermore, the pressure-drop constraint shows minimal effect on the final value of NPW. The NPW trends downward with increasing allowable pressure drop, which is in line with expectations. In what follows, we investigate the variation of the objective function NPW and its elements,

as depicted in Figure 6.1 The total capital investment comprises >65% of the total NPW value, while the bed replacement contribution is the lowest (~5%). One third of the total capital investment is allocated to hydrogenation costs (i.e. feed heating, hydrogenation, and cooling). Notably, approximately 65% of the total ensued OPEX is allocated to hydrogenation costs. Moreover, NPW increases with increasing pressure drop, primarily driven by an increase in the total capital investment. Solutions obtained via the full dual step approach lead to slightly lower costs primarily driven by reduction in OPEX. The total capital investment estimated here is in the order of $20M. For a similar size unit, the SCOT technology ensues a total capital investment of ~$50M. This drastic difference brings attention to the commercial appeal of adsorption technology. Furthermore, the TSA approach is theoretically capable of attaining higher recoveries since the H_2S concentration of its effluent stream is in the sub-ppm levels, hence addressing any changes in SO_x emissions' regulations. Based on the sulfur processing capacity of 400 tons·day^{-1} for both plants, the operating cost estimated in this work falls within the range of $2.0 to $2.2 per ton of processed sulfur. In the economic study reported by Koscielnuk et al. [7], the operating cost for the SCOT technology was determined to be in the order of $20 ton^{-1}. After rescaling the TGTU operating costs using utility costs reported in [7], the updated figures range between $3.0 and 3.6 ton^{-1}. The significantly lower operating cost of the TSA based TGTU process suggests high potential for this technology. Moreover, benchmarking the presented results with their counterparts reported by the Gas Technology Institute [9] shows that the capital investment of the proposed TGTU comprises ~20% of the total SRU TCI. The major advantage is attained in the operating costs which lie significantly below any of the commercially implemented TGTUs.

	Case 1		Case 2		Case 3	
Parameter	**First**	**Second**	**First**	**Second**	**First**	**Second**
P. drop (kPa)	10	10	15	15	20	20
F. print (m^2)	250	250	250	250	250	250
L (m)	6.72	6.47	7.56	7.18	8.22	7.81
D (m)	4.32	4.35	4.01	4.05	3.80	3.85
N_1 ($kmol \cdot h^{-1}$)	728.46	585.67	703.80	650.00	688.43	640.00
T_{reg} (^oC)	550.00	550.00	550.00	522.23	550.00	529.30
f (yr)	6	6	6	6	6	6
t_{ads} (h)	26.28	26.28	26.28	26.28	26.28	26.28
N	4	4	4	4	4	4
NPW ($)	3.57E+07	3.45E+07	3.50E+07	3.43E+07	3.46E+07	3.40E+07

Table 6.4/P-170 Results of the TSA based TGTU optimization (First refers to results of first step of optimization, while second refers to the final results of the entire optimization approach)

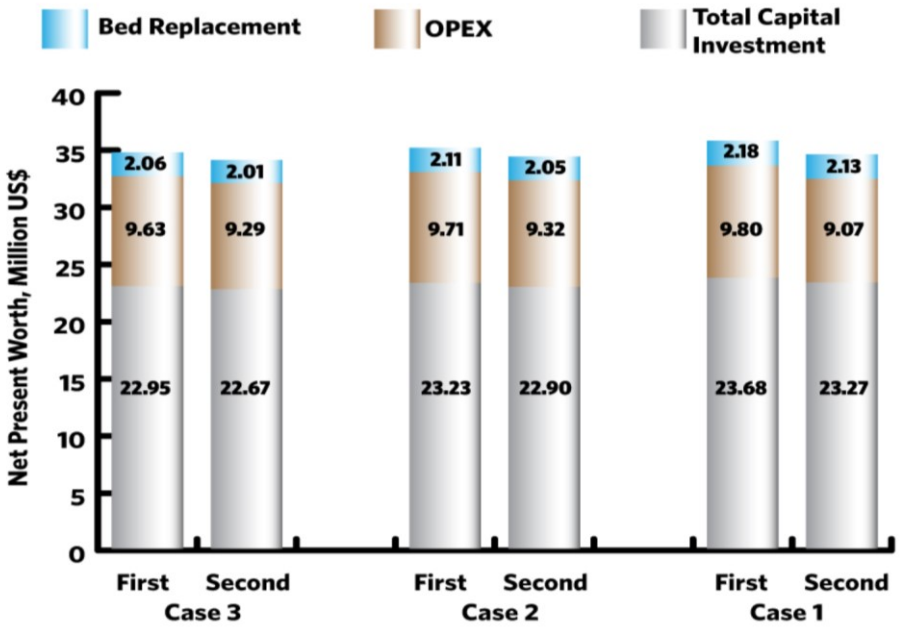

Figure 6.1/P-170 Contribution of NPW elements for the studied cases (see table above)

The temperature, H_2S mole-fraction, adsorbed phase concentration, and vessel steel temperature profiles for the optimal solution for the 10 KPa case computed by gPROMS 3.7.1 are presented in Figures 6.2 (a-d), while Figures 6.3 (a-d) presents the time profiles of the same variables at the exit of the regeneration gas (i.e. L=0). The concentration profile

exhibits an overshoot at time 27.8 h (~100000s) at which the concentration exceeds 8%. This overshoot occurs after 1.6 hours from the start of the regeneration and extends to 7 hours. Furthermore, the bed temperature profiles exhibit a fairly fast increase during regeneration and subsequent sharp decrease during cooling. Thus, the adsorbent pellets are expected to experience substantial thermal stresses during regeneration and cooling. In addition, the temperatures profiles suggest that the majority of the regeneration step timing is occupied by heating and bed regeneration. Cooling times are quite short in comparison. Interestingly, the vessel steel temperature does not cool down completely to the target feed temperature (Steel ~340^{o}C vs. Feed 150^{o}C). The protocol described in chapter 4 enforces complete cooling of the vessel steel and the bed down to the feed temperature. Hence, the reduction in OPEX for the final solution can be attributed to the latter observation. Furthermore, the changes in vessel temperature are less pronounced when compared to the bed.

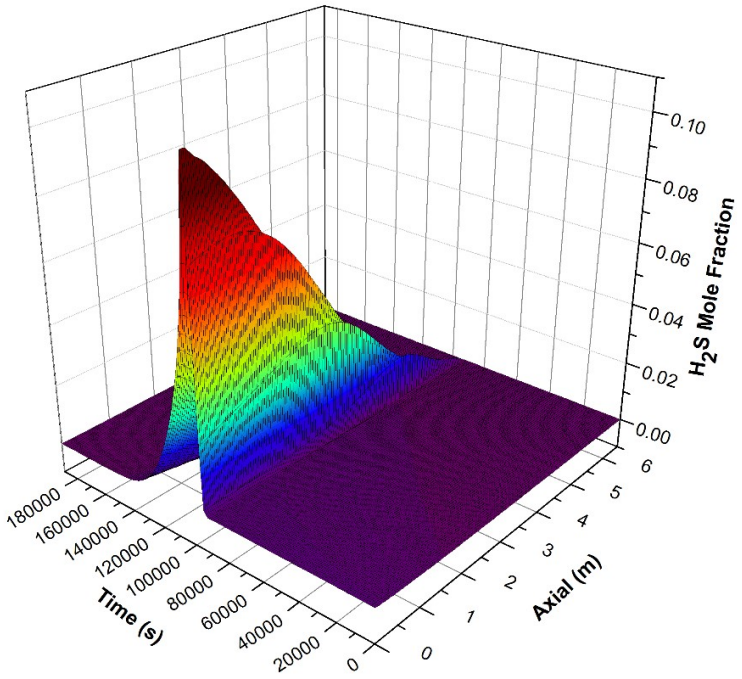
0.10
0.08
0.06
0.04
0.02
0.00
H2S Mole Fraction
180000
160000
140000
120000
100000
80000
60000
40000
20000
0
Time (s)
0
1
2
3
4
5
6
Axial (m)

(a)

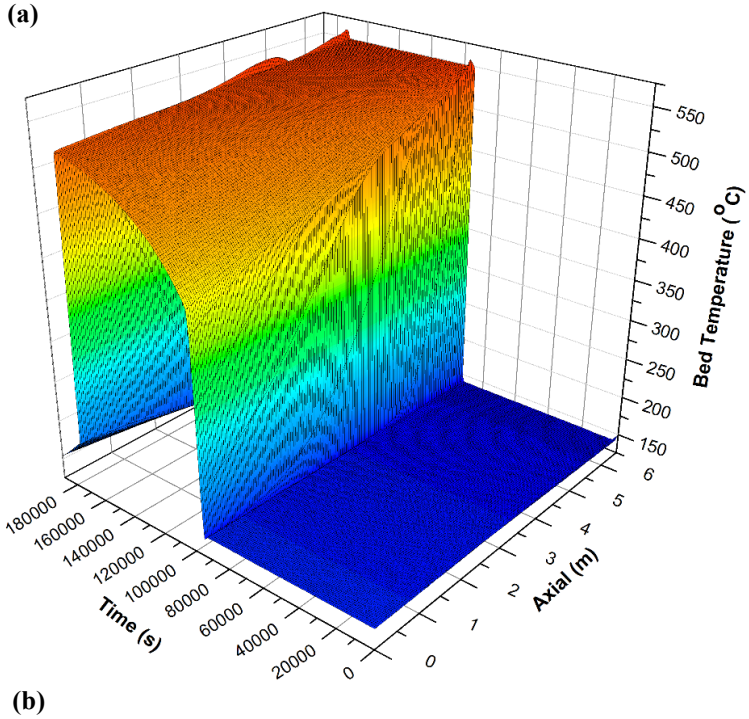
550
500
450
400
350
300
250
200
150
Bed Temperature (°C)
180000
160000
140000
120000
100000
80000
60000
40000
20000
0
Time (s)
0
1
2
3
4
5
6
Axial (m)

(b)

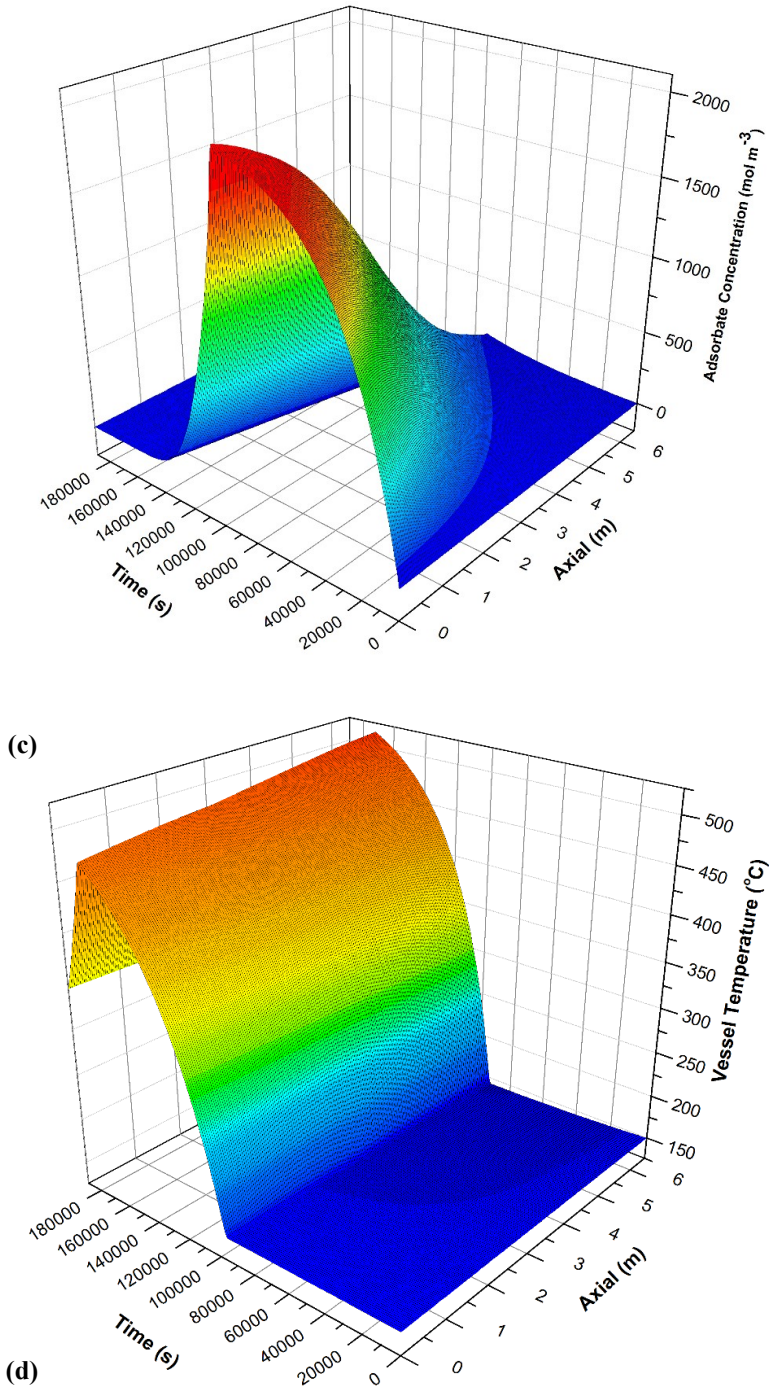

Figure 6.2/P-173 Space-time profiles of (a) H_2S mole-fraction, (b)) bed temperature, (c) H_2S adsorbed phase concentration, and (d) vessel temperature

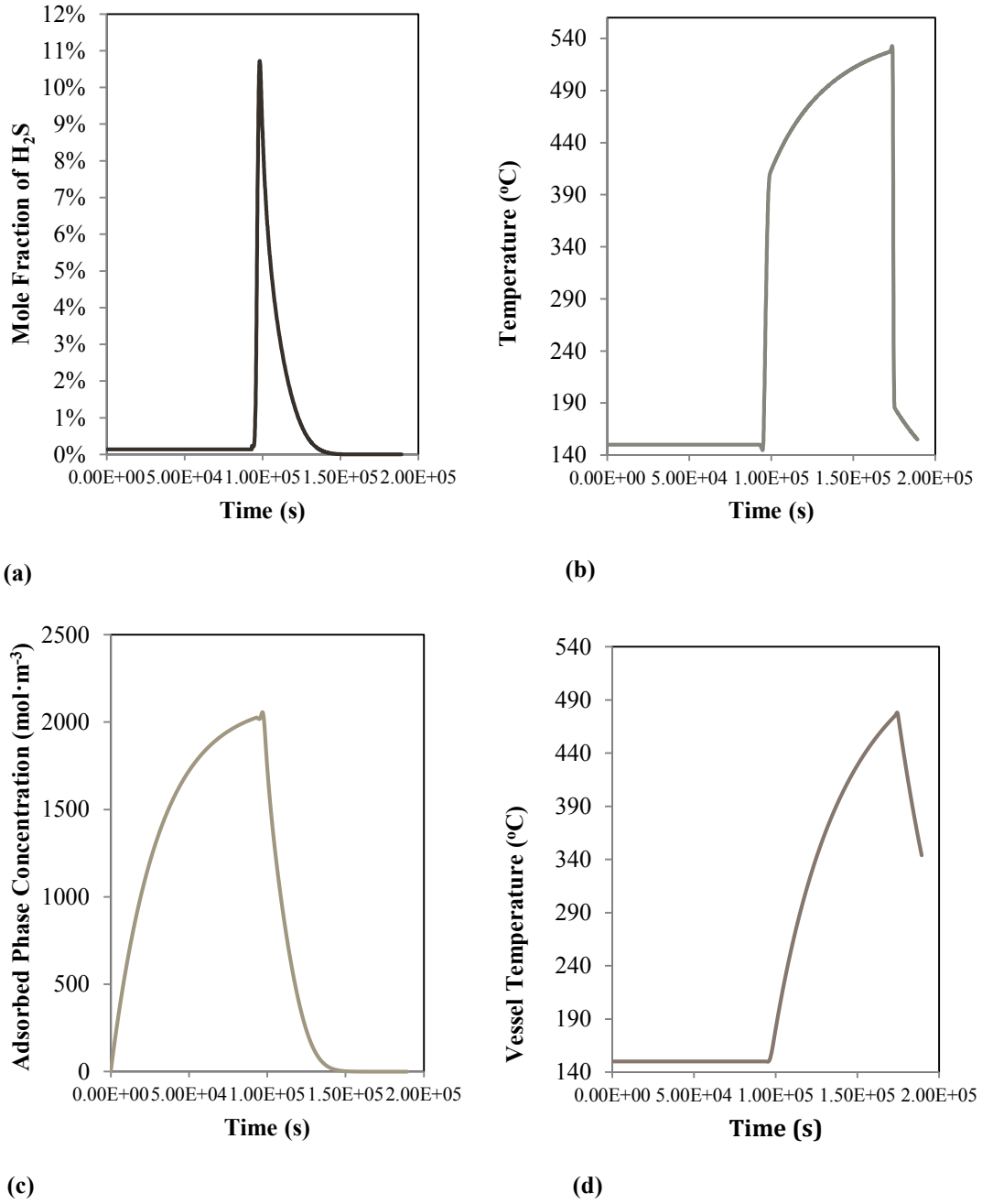

Figure 6.3/P-174 Time profiles of (a) H_2S mole-fraction, (b)) bed temperature, (c) H_2S adsorbed phase concentration, and (d) vessel temperature at L=0

The results presented thus far suggest a high potential for the proposed TGTU system in competing with current applied technologies, especially in operating costs. In the analysis laid previously a crucial assumption was made regarding the long term stability of the sorbent (stable for 1000 regeneration cycles). Such stability has not been confirmed yet.

Furthermore, while adsorbent capacity towards H_2S was shown to be sustained in presence of single competing adsorbates [15], the behavior of the adsorbent when exposed to the full mixture is still not studied. Accurate modeling requires all of these factors to be thoroughly studied.

6.3 CONCLUSIONS

The economic analysis of the TSA based TGTU system has shown its significant potential in competing with commercial alternatives. The total capital investment of a TSA Claus Tail Gas Clean Up system based on Cu(I)-Y is estimated to be around $20M compared to $50M for the SCOT process, a leading currently implemented technology. Operating costs are expected to be in the range of $3.0 and 3.6 ton^{-1} of sulfur compared to $20 ton^{-1} for the SCOT option considering equivalent utility costs. The reported cost figures suggest that the TSA option has high potential and justifies further evaluation and development.

CHAPTER 7: CONCLUSIONS AND FUTURE WORK

7.1 CONCLUSIONS

Current international regulations regarding SO_x emissions require achievement of +99.9% conversion in Sulfur Recovery Units [3]. The available commercially applied options to achieve the required recovery suffer from high capital investment, high operating costs and large expansion of the SRU plant footprint [63]. Utilization of Temperature Swing Adsorption (TSA) systems as a viable option for Claus tail gas clean-up has been explored in the ELSE process and the Z-sorb process [9,5]; commercial application was not achieved though, most probably due to the absence of a regenerable sorbent with high selectivity towards sulfur containing species. However, in recent years new classes of sorbents were discovered holding significant potential [15-17, 171].

In light of the newly discovered adsorbents, the premise of this thesis is to reassess the potential of TSA system from an economic perspective and benchmark it with existing commercial technologies. The objectives pursued were:

- To propose a process concept of an adsorption based system that utilizes resources available within the sulfur recovery unit.
- To screen reported adsorbents and identify the most promising ones.
- To generate the necessary kinetic and thermodynamic properties of a selected adsorbent in case such properties are not reported.
- To provide an efficient algorithm for the fast design and optimization of adsorbent-based technologies.

- To implement the developed framework on the selected adsorbent given an industrial feed as to arrive at an economical assessment of the technology.

It is important for the economic assessment to use a cost probe that reflects all the ensued costs during the life time of the plant. For that, I have chosen the net present worth of all costs ensued during a 30 years life plant using the (NPW) function. The selected function consists of the total capital investment, the net present worth of operating costs and the net present worth of costs due to bed replacement. The function was then integrated into a non-linear based model which incorporates the governing physics reflected by the differential mass and energy balances, a pressure drop correlation, spatial constraints and the cost correlations. The selected design variables encompassed both integer and continuous variable.

Optimization of swing systems is not an easy feat as reflected by the reported literature. The complexity arises from the need of optimizing a system which is non-steady by its nature and governed by PDEs that rarely have an analytical solution. Coupling to that the discontinuous nonlinear nature of the selected objective function, the mixed nature of the design/decision variables and the need for employing an optimization technique that can conduct "wide" search of the solution space while assuring local optimality, it is clear that the problem becomes extremely complex. The problem was tackled by employing a two-step optimization approach. In the first step, the governing PDE model is reformulated into an analytical nonlinear model which uses the equilibrium case solution of Rhee et al. [30] and account for mass transfer effects via an efficiency factor. The efficiency factor correlations were obtained via regressing kinetic simulation data generated using the

governing isothermal PDE as the basis which was solved via the Kaczmarski approach [92]. The adopted cycle design in the first step followed the one proposed by Wunder et al. for the design of temperature swing adsorption systems [73]. While, adsorption is envisaged to occur isothermally, regeneration is envisaged to simulate a phase change on which the adsorbed species transforms to the gas phase isothermally at an experimentally determined regeneration temperature. Hence, the cycle is envisaged to occur via the following steps:

- Adsorption Step: Isothermal adsorption of sulfur species from a uniform flow of Claus tail gas stream.
- Heating Step: Heating the sorbent bed and vessel to an experimentally determined temperature via passage of hot regeneration gas and supplying the adsorption heat required to remove the adsorbed phases.
- Regeneration Step: Regeneration by passing hot regeneration gas across the bed until complete bed regeneration to fresh conditions is achieved. This step is assumed to occur isothermally.
- Cooling Step: Cooling down of bed back to operating temperature using the cold purge stream.

The newly developed model was then integrated with the rest of the constraints and objective function cost correlations thus forming an MINLP problem. To allow use of techniques which assures local optimality, the problem was broken down into multiple NLPs via enumerating all possible combinations of integer variables. Subsequently, the set of NLPs were solved using an SQP approach that assures local optimality combined with

a multi-start sub-routine which randomly generates initial guesses. The protocol was coded in Matlab™ language and the *fmincon* function was used for the optimization of the NLPs. The final resulting solution was then used as an initial guess in the second step of the optimization approach. In the second step, the resulting solution was used as an initial guess in solving a higher complexity model of the TSA system which is non-isothermal and accounts for mass transfer effects via the generally accepted linear driving force model. The system was optimized using gPROMs, CVP_SS optimization routine for a single initial guess test. The final obtained solution was considered an optimal estimate of the cost of the TSA technology given the properties of a chosen adsorbent and the plant and economic related parameters as inputs.

The other side of the assessment pertained to the selection of the adsorbent and the experimental determination of its properties. The literature review led to the initial identification of metal oxides and metal exchanged zeolites as the most promising adsorbents for the TSA unit. While metal oxides enjoyed very high capacities, the severity of the regeneration conditions rendered them an expensive option for the TSA unit considering the need for using expensive construction materials to accommodate the severe regeneration conditions. Hence, metal exchanged zeolites were chosen as the basis adsorbent. Among metal exchanged zeolites, CuY held the most promise since its regenerability were proven and its thermodynamic adsorption properties were reported in literature [14, 15, 172]. Experimental assessment of the adsorbent has identified 150^{o}C as the most suitable temperature since it eliminates the release of SO_2 during adsorption while retaining a fully regenerable capacity of ~1 mmol·g^{-1}. The regeneration profiles of the adsorbent were fitted with a PDE based to obtain the required kinetic and thermodynamic

properties. Finally, the resulting properties, model and optimization protocol were implemented in the assessment of a real industrial case. In light of the work performed, the following conclusions are drawn:

1) Among the available options for achieving sulfur recovery of +99.9%, all the reported commercial technologies ensue a capital investment and an operating cost of approximately comprising 30 to more than 50% of the total SRU costs.
2) Among the investigated TGTU concepts, the hydrogenation plus TSA system appeared to be the closest to implementation considering the difficulty of identifying a regenerable adsorbent with suitable affinity towards H_2S and SO_2.
3) In kinetic modeling, the Kaczmarski scheme combined low computational cost and good accuracy as compared to orthogonal collocation methods. This rendered it a suitable solution approach for the 1st optimization step.
4) However, the scheme excludes surface diffusion as a mode of mass transfer and cannot be used in non-isothermal models.
5) Because of the above, the non-isothermal Linear driving force model is more adequate to be used as the governing model for the second stage of the optimization protocol.
6) CuY was identified as the most suitable adsorbent considering the proven regenerability over 9 cycles of tests.
7) At temperatures higher than 150^{o}C the sorbent releases SO_2 during the adsorption step most probably due to re-adsorption during the regeneration of the adsorbent. Still the capacity is retained.

8) CuY adsorption action towards H_2S was due to the action of copper exchanged sites within the framework of the zeolite and due to dispersed nano-crystallites of CuO.
9) Implementation of the optimization protocol on an industrial case led to the following economic conclusions:
    a. For a sulfur recovery unit having a capacity of 400 tons of sulfur per day, the proposed adsorption based TGTU is expected to incur $20 M in capital investment compared to $50M for the SCOT™ process.
    b. For the same size sulfur recovery unit, the proposed adsorption based TGTU is expected to incur $3.0 to $3.6 per ton of sulfur which compares favorably with the $20 per ton for the SCOT™ process.
10) The computational time for the whole optimization process excluding the time dedicated for the generation of the efficiency factor correlations was approximately 2200 s when performed over an Intel™ Xeon™ CPU E5-2609 clocked at 2.40 GHz.
11) The reported cost figures suggest that the TSA option has high potential and justifies further evaluation and development.

Still, there are several areas were possible improvements are envisaged. Those are discussed in the upcoming section.

7.2 FUTURE WORK

The optimization protocol proposed in this thesis forms a complete solution set for fast screening of sorbents. Still, the developed protocol requires generation of the efficiency factor correlations for every industrial case and adsorbent assessed in order to assure fast convergence. Moreover, the protocol pertains only to adsorbents were the adsorption

thermodynamics are modeled via a conventional isotherm model such as the extended Langmuir model. Improvements pertaining to those two issues are discussed herein.

7.2.1 IMPROVEMENTS ON THE EFFICIENCY FACTORS

The optimization approach proposed relied on analytical models for describing the adsorption phenomena corrected for mass transfer effects via an efficiency factor. The generation of efficiency factor correlation uses the adsorbent properties as an invariant input. Since the adsorption properties are strong functions of the adsorbent itself and the temperature, a new correlation has to be generated for each case. Clearly, developing a holistic correlation which takes into account the adsorbent properties and their dependency on temperature would greatly expand the viability of the approach. Errors as large as 30% can be tolerated since the solution obtained from the first step is only used as an initial guess. Finally, tests on systems which obey other thermodynamic adsorption models has to be conducted in order to verify the model range of applicability.

7.2.2 IMPROVEMENTS ON THE KINETIC MODEL

On the level of kinetic modeling we foresee a number of regions were significant improvements can be achieved. The first region lies in the adsorption model. The adsorption employed in this work is the extended Langmuir model. This model was employed because of its simplicity and the availability of experimental data for H_2S adsorption in the Langmuir form. Still, the extended Langmuir model suffers from thermodynamic inconsistency if the sorbent do not have the same saturation capacity towards the adsorbing species [98].

Other simple models can be implemented without sacrifices in the computational side while enhancing the accuracy of the adsorption model. For instance the generalized Langmuir-Freundlich model, enhance the accuracy of the extended Langmuir by expressing the adsorption isotherm for each species using 4 parameters instead of the Langmuir two parameters (equilibrium constant (K) and the saturation capacity (q_s)). The model is described by the following equation [98]:

$$q_i^* = q_{s,i} \frac{(b_i/\eta_i)P^{1/n_i}}{1+\sum_{j=1}^{N}(b_j/\eta_j)P^{1/n_j}} \quad (7.1)$$

Where qi* is the adsorbate equilibrium concentration, $q_{s,i}$ is the saturation capacity, b_i is the equilibrium constant, η_i fitting parameter taking care of same molecule interaction and n_i fitting parameter takes care of surface heterogeneity. Since the model is explicit, its integration into the Kaczmarski algorithm can be easily realized without any computational sacrifices. Other more complex model can be incorporated but at the level of the second step. For instance the Ideal Adsorption Solution model can be easily integrated with the linear driving force model without any substantial computational limitations.

Furthermore, all the models described above pertain to thermodynamically modelled adsorbents. Metal oxides and their mixtures involve a gas solid reaction in which the adsorbent morphology and other properties (such as the density and heat capacity) can change dramatically during adsorption. For those cases, models such as the unreacted shrinking core model [173], the modified grain model [174], the overlapping grain model and the deactivation model are better suited [175]. The deactivation model leads to an analytical solution to the breakthrough time which can be directly integrated to the

optimization algorithm and hence circumvent the need for generating the efficiency factors. Hence, it can be used as the basis for the first step optimization. Finally, the cycle model employed pertained to a purely TSA model. Application of vacuum assisted TSA model might reap cost benefits and hence can be a topic for further research.

7.3 FINAL REMARKS

Optimization of adsorption systems has been a complex problem requiring significant simplifications in order to attain a plausible solution. The framework that is proposed herein allows bypassing the need for significant simplifications hence expanding the scope of problems that can be tackled. Finally, the studies covered by this thesis suggest that the adsorption route can be a viable option for commercially competitive TGTU technology. Adsorption based systems might not only allow gains in the cost side but also provides a future-proof option in the face of any unforeseen changes in the regulations set by environmental agencies.

BIBLIOGRAPHY

1. Philip R. Weems , F.M. *A Surprising Reality: Middle East Naturarl Gas Crunch*. THE INTERNATIONAL WHO'S WHO OF OIL & GAS LAWYERS, 2009.
2. Larssen, T., et al., *Acid rain in China.* Environmental Science & Technology, 2006. **40**(2): p. 418-425.
3. EPA. http://www.epa.gov/air/sulfurdioxide [accessed 10-12-2011].
4. Hasenberg, L., *Sulfur Dioxide*, in *Corrosion Handbook: Sulfate Dioxide, Sodium Sulfate*, M.S. G. Kreysa, Editor. 2008.

5. Kohl, A. and R. Nielsen, *GAS PURIFICATION*. Fifth ed. Vol. 1. 1997, Houston: Gulf Publishing Company. 1397.

6. Parliament, E., *DIRECTIVE 2001/80/EC OF THE EUROPEAN PARLIAMNET AND OF THE COUNCIL of 23 October 2001-On the limitation of emissions of certain pollutants into air from large combustion plants*, E. UNION, Editor. 2001. p. 21.

7. Koscielnuk, D., et al. *Low Cost and Reliable Sulfur Recovery*. 2001.

8. Eow, J.S., *Recovery of sulfur from sour acid gas: A review of the technology.* Environmental Progress, 2002. **21**(3): p. 143-162.

9. J. F. Strickland, M.Q.D.V., D. Leppin and H. Meyer *TAIL GAS CLEAN-UP PROCESSES: CAPABILITIES AND RELATIVE COSTS*. 2000.

10. MCCABE, SMITH, and HARRIOT, *Unit Operations of Chemical Engineering* SIXTH ed. Vol. 1. 2001, SIngapore: McGRAW-HILL 1115.

11. John S. Buchanan, K.E.N., *Process for treating H.sub.2 S containing streams*. 2000, Mobil Oil Corporation: USA.

12. Buchanan, J.S., et al., *Regenerable Solid Sorbents for Claus Tailgas Cleanup: A Treatment Process for the Catalytic Removal of SO_2 and H_2S.* Industrial & Engineering Chemistry Research, 1996. **35**(8): p. 2495-2499.

13. Mohamadalizadeh, A., et al., *Modification of Carbon Nanotubes for H_2S Sorption.* Industrial & Engineering Chemistry Research, 2011. **50**(13): p. 8050-8057.

14. Crespo, D., et al., *Superior Sorbent for Natural Gas Desulfurization.* Industrial & Engineering Chemistry Research, 2008. **47**(4): p. 1238-1244.

15. Kumar, P., et al., *H_2S adsorption by Ag and Cu ion exchanged faujasites.* Microporous and Mesoporous Materials, 2011. **146**(1-3): p. 127-133.

16. Polychronopoulou, K., J.L.G. Fierro, and A.M. Efstathiou, *Novel Zn-Ti-based mixed metal oxides for low-temperature adsorption of H2S from industrial gas streams.* Applied Catalysis B: Environmental, 2005. **57**(2): p. 125-137.

17. Polychronopoulou, K., et al., *Novel Fe-Mn-Zn-Ti-O mixed-metal oxides for the low-temperature removal of H2S from gas streams in the presence of H_2, CO_2, and H_2O.* Journal of Catalysis, 2005. **236**(2): p. 205-220.

18. Yasyerli, S., et al., *Activities of Copper Oxide and Cu-V and Cu-Mo Mixed Oxides for H_2S Removal in the Presence and Absence of Hydrogen and Predictions of a Deactivation Model.* Industrial & Engineering Chemistry Research, 2001. **40**(23): p. 5206-5214.

19. Karayilan, D., et al., *Mn-Cu and Mn-Cu-V Mixed-Oxide Regenerable Sorbents for Hot Gas Desulfurization.* Industrial & Engineering Chemistry Research, 2005. **44**(14): p. 5221-5226.

20. Elyassi, B., et al., *A high-performance adsorbent for hydrogen sulfide removal.* Microporous and Mesoporous Materials, 2014. **190**(0): p. 152-155.

21. Agarwal, A., L.T. Biegler, and S.E. Zitney, *Simulation and Optimization of Pressure Swing Adsorption Systems Using Reduced-Order Modeling.* Industrial & Engineering Chemistry Research, 2008. **48**(5): p. 2327-2343.

22. Jiang, L., L.T. Biegler, and V.G. Fox, *Simulation and optimization of pressure-swing adsorption systems for air separation.* AIChE Journal, 2003. **49**(5): p. 1140-1157.

23. Cruz, P., F.D. Magalhães, and A. Mendes, *On the optimization of cyclic adsorption separation processes.* AIChE Journal, 2005. **51**(5): p. 1377-1395.

24. Cruz, P., et al., *Cyclic adsorption separation processes: analysis strategy and optimization procedure.* Chemical Engineering Science, 2003. **58**(14): p. 3143-3158.

25. Ding, Y., D. T. Croft, and M.D. LeVan, *Periodic states of adsorption cycles IV. Direct optimization.* Chemical Engineering Science, 2002. **57**(21): p. 4521-4531.

26. Ko, D., R. Siriwardane, and L.T. Biegler, *Optimization of a Pressure-Swing Adsorption Process Using Zeolite 13X for CO2 Sequestration.* Industrial & Engineering Chemistry Research, 2002. **42**(2): p. 339-348.

27. Jiang, L., V.G. Fox, and L.T. Biegler, *Simulation and optimal design of multiple-bed pressure swing adsorption systems.* AIChE Journal, 2004. **50**(11): p. 2904-2917.

28. Sankararao, B. and S.K. Gupta, *Multi-Objective Optimization of Pressure Swing Adsorbers for Air Separation.* Industrial & Engineering Chemistry Research, 2007. **46**(11): p. 3751-3765.

29. Smith IV, O.J. and A.W. Westerberg, *The optimal design of pressure swing adsorption systems.* Chemical engineering science, 1991. **46**(12): p. 2967-2976.

30. Rhee, H.-K., R. Aris, and N.R. Amundson, *On the Theory of Multicomponent Chromatography.* Philosophical Transactions of the Royal Society of London. Series A, Mathematical and Physical Sciences, 1970. **267**(1182): p. 419-455.

31. Wikipedia. http://en.wikipedia.org/wiki/Claus_process [accessed 11-14-2011].

32. Nelliott. http://www.nelliott.demon.co.uk/company/claus.html [accessed 10-20-2011].

33. Gray, M.R. and W.Y. Svrcek, *Oxygen use in Claus sulphur plants*. 1981. Medium: X; Size: Pages: B.1-B.30.

34. Anonymous, *Oxygen enrichment enhances plant performance.* Sulphur, 1995(241).

35. GPSA, G.P.S.A., *Sulfur Recovery*, in *GPSA Engineering Data Book*. GPSA.

36. Clark, P.D. in *SOGAT Proceedings-Workshop*. 2005. Abu Dhabi UAE.

37. Tesner, P., M. Nemirovskii, and D. Motyl, *Kinetics of the thermal decomposition of hydrogen sulfide at 600-1200oC.* Kinetics and catalysis, 1990. **31**(5): p. 1081-1083.

38. Kaloidas, V. and N. Papayannakos, *Kinetics of thermal, non-catalytic decomposition of hydrogen sulphide.* Chemical Engineering Science, 1989. **44**(11): p. 2493-2500.

39. Roth, P., R. Löhr, and U. Barner, *Thermal decomposition of hydrogen sulfide at low concentrations*. Combustion and Flame, 1982. **45**(0): p. 273-285.

40. Dowling, N.I., J.B. Hyne, and D.M. Brown, *Kinetics of the reaction between hydrogen and sulfur under high-temperature Claus furnace conditions.* Industrial & Engineering Chemistry Research, 1990. **29**(12): p. 2327-2332.

41. Hawboldt, K.A., W.D. Monnery, and W.Y. Svrcek, *New experimental data and kinetic rate expression for H_2S pyrolysis and re-association.* Chemical Engineering Science, 2000. **55**(5): p. 957-966.

42. Clark, P.D., et al., *Mechanisms of CO and COS Formation in the Claus Furnace.* Industrial & Engineering Chemistry Research, 2000. **40**(2): p. 497-508.

43. Karan, K., A.K. Mehrotra, and L.A. Behie, *COS-Forming Reaction between CO and Sulfur: A High-Temperature Intrinsic Kinetics Study*. Industrial & Engineering Chemistry Research, 1998. **37**(12): p. 4609-4616.

44. Karan, K. and L.A. Behie, *CS_2 Formation in the Claus Reaction Furnace: A Kinetic Study of Methane−Sulfur and Methane−Hydrogen Sulfide Reactions*. Industrial & Engineering Chemistry Research, 2004. **43**(13): p. 3304-3313.

45. LUINSTRA, E.A. and P.E. D'HAENE, *Catalyst added to Claus furnace reduces sulfur losses*. Vol. 68. 1989, Houston, TX, ETATS-UNIS: Gulf.

46. Nasato, L.V., et al., *Modeling reaction quench times in the waste heat boiler of a Claus plant.* Industrial & Engineering Chemistry Research, 1994. **33**(1): p. 7-13.

47. Clark, P.D., N.I. Dowling, and M. Huang, *Conversion of CS_2 and COS over alumina and titania under Claus process conditions: reaction with H_2O and SO_2.* Applied Catalysis B: Environmental, 2001. **31**(2): p. 107-112.

48. Mendioroz, S., et al., *Kinetic study of the Claus reaction at low temperature using γ-alumina as catalyst.* Applied Catalysis A: General, 1995. **132**(1): p. 111-126.

49. Elsner, M.P., et al., *The Claus process: teaching an old dog new tricks.* Catalysis Today, 2003. **79-80**: p. 487-494.

50. Chiyoda.*http://www.chiyodacorp.com/technology/en/upstream_gasprocessing/tail_gas_treating_tgt.html*. [accessed 11-14-2011].

51. Rameshni, M. *Selection Criteria for Claus Tail Gas Treating Processes*.

52. Clark, P.D. 2014.

53. Peterman, L.G. and E. Czyszczon, *Claus tail gas recovery*. 1979, Google Patents.

54. Groenendaal, W., H.G.A. Kock, and P. Loof, *Reduction to hydrogen sulfide*. 1976, Google Patents.

55. Williamson, A.E., *Sulfur dioxide, reduction with hydrogen*. 1978, Google Patents.

56. Jagannathan N. Iyengar, D.P., Robert B. Fedich, *Sulfur Recovery Plant Tail Gas Treatment Process*, E. Mobil, Editor. 2001: USA.

57. Swaim, D.C., *The Shell Claus Offgas Treating (SCOT) Process*, in *Sulfur Removal and Recovery*. 1975, AMERICAN CHEMICAL SOCIETY. p. 111-119.

58. Thompson, R.B., *Iron chelate catalysts*. 1980, Google Patents.

59. Thompson, R.B., *Composition for catalytic removal of hydrogen sulfide from gases*. 1980, Google Patents.

60. Dalrymple, D.A., T.W. Trofe, and J.M. Evans, *Liquid redox sulfur recovery options, costs, and environmental considerations.* Environmental Progress, 1989. **8**(4): p. 217-222.

61. Merichem. http://www.merichem.com/images/casestudies/Desulfurization.pdf [accessed 10-11-2014].

62. Koscielnk, D., et al. *Low Cost and Reliable Sulfur Recovery*. 2001.

63. Scheel, F., *INNOVATIVE APPROACH TO SULFUR RECOVERY UNIT EMISSION REDUCTIONS* in *SOGAT* 2001.

64. Min-Hsiun, L. and P.T. Pendergraft, *Sulfur Recovery Process Using Metal Oxide Absorbent*. 1989: USA.

65. Stern, D.L., et al., *The Mobil Oil SO_x Treatment Process (MOST). Catalytic removal of SO_x and H_2S from refinery tailgas.* Catalysis Today, 2000. **55**(3): p. 311-316.

66. Khare, G.P., et al., *Hot gas desulfurization with Phillips Z-Sorb sorbent in moving bed and fluidized bed reactors.* Environmental Progress, 1995. **14**(3): p. 146-150.

67. Personal Communication, B.P., *Commercialization of the ELSE process.* 2013.

68. Personal Communication, E.M., *Commercialization of the MOST process*. 2013.

69. Don W. Green, R.H.P., *Perry's Chemical Engineer's Handbook*. 8th Edition ed. 2007: Mc Graw Hill.

70. AlWahedi, A.M., *Ruwais Fertilizer Industries (FERTIL)*. 2011.

71. Gordon, F. *http://www.icispricing.com/il_shared/Samples/SubPage152.asp*. [accssed 11-14-2011].

72. Bryan-Resarch.*http://www.bre.com/promax/capabilities/sulfur-and-tgcu.aspx*. [accessed 04-04-2012].

73. Wunder, J., *How to design a natural gas drier.* Oil and Gas, 1962.

74. Yang, R.T., *GAS SEPARATION BY ADSORPTION PROCESSES*. Series on Chemical Engineering, ed. R.T. Yang. Vol. 1. 1997, London: Imperial College Press. 352.

75. Cussler, E.L., *Diffusion-Mass Transfer in Fluid Systems*. Third ed. 2009: CAMBRIDGE.

76. http://www.hpfmresearch.com/research/zeolite. *Fajuasite Crystal*. [accessed 01-15- 2015].

77. Rhee, H.-K., N.R. Amundson, and R.P. Lewis, *Shock layer analysis of adiabatic adsorption in fixed beds with axial dispersion.* The Chemical Engineering Journal, 1982. **23**(2): p. 167-176.

78. Mazzotti, M., G. Storti, and M. Morbidelli, *Shock layer analysis in multicomponent chromatography and countercurrent adsorption.* Chemical Engineering Science, 1994. **49**(9): p. 1337-1355.

79. Lin, B., et al., *Shock layer analysis for a single-component in preparative elution chromatography.* Journal of Chromatography A, 1995. **708**(1): p. 1-12.

80. Kaczmarski, K., et al., *Modeling fixed-bed adsorption columns through orthogonal collocations on moving finite elements.* Computers & Chemical Engineering, 1997. **21**(6): p. 641-660.

81. Wakao, N. and T. Funazkri, *Effect of fluid dispersion coefficients on particle-to-fluid mass transfer coefficients in packed beds: Correlation of sherwood numbers.* Chemical Engineering Science, 1978. **33**(10): p. 1375-1384.

82. Dubbeldam, D., et al., *Molecular simulation of loading-dependent diffusion in nanoporous materials using extended dynamically corrected transition state theory.* The Journal of Chemical Physics, 2005(122).

83. Garg, D.R. and D.M. Ruthven, *The performance of molecular sieve adsorption columns: systems with micropore diffusion control.* Chemical Engineering Science, 1974. **29**(2): p. 571-581.

84. Yucel, H. and D.M. Ruthven, *Diffusion in 4A zeolite. Study of the effect of crystal size.* Journal of the Chemical Society, Faraday Transactions 1: Physical Chemistry in Condensed Phases, 1980. **76**: p. 60-70.

85. Ko, D. and I. Moon, *Multiobjective Optimization of Cyclic Adsorption Processes.* Industrial & Engineering Chemistry Research, 2002. **41**(1): p. 93-104.

86. Cen, P.L. and R.T. Yang, *Analytic solution for adsorber breakthrough curves with bidisperse sorbents (zeolites).* AIChE Journal, 1986. **32**(10): p. 1635-1641.

87. Villadsen, J. and M.L. Michelsen, *SOLUTION OF DIFFERENTIAL EQUATION MODELS by POLYNOMIAL APPROXIMATION*. 1978: PRENTICE HALL.

88. K, K., *Use of orthogonal collocation on finite elements with moving boundaries in the simulation of non-linear multicomponent chromatography. Influence of fluid velocity variation on retention time in LC and HPLC.* Computers & Chemical Engineering, 1996. **20**(1): p. 49-64.

89. Yu, Q. and N.H.L. Wang, *Computer simulations of the dynamics of multicomponent ion exchange and adsorption in fixed beds,gradient-directed moving finite element method.* Computers & Chemical Engineering, 1989. **13**(8): p. 915-926.

90. Rouchon, P., et al., *Numerical Simulation of Band Propagation in Nonlinear Chromatography.* Separation Science and Technology, 1987. **22**(8-10): p. 1793-1833.

91. Czok, M. and G. Guiochon, *Comparison of the results obtained with different models for the simulation of preparative chromatography.* Computers & Chemical Engineering, 1990. **14**(12): p. 1435-1443.

92. Kaczmarski, K. and D. Antos, *Modified Rouchon and Rouchon-like algorithms for solving different models of multicomponent preparative chromatography.* Journal of Chromatography A, 1996. **756**(1,2): p. 73-87.

93. Kaczmarski, K. and D. Antos, *Fast finite difference method for solving multicomponent adsorption-chromatography models.* Computers & Chemical Engineering, 1996. **20**(11): p. 1271-1276.

94. Nilchan, S. and C.C. Pantelides, *On the Optimisation of Periodic Adsorption Processes.* Adsorption, 1998. **4**(2): p. 113-147.

95. Ding, Y., D.T. Croft, and M.D. LeVan, *Periodic states of adsorption cycles IV. Direct optimization.* Chemical Engineering Science, 2002. **57**(21): p. 4521-4531.

96. Biegler, L.T., L. Jiang, and V.G. Fox, *Recent Advances in Simulation and Optimal Design of Pressure Swing Adsorption Systems.* Separation & Purification Reviews, 2005. **33**(1): p. 1-39.

97. Kapoor, A. and R.T. Yang, *Optimization of a pressure swing adsorption cycle.* Industrial & Engineering Chemistry Research, 1988. **27**(1): p. 204-206.

98. Do, D.D., *Adsorption Analysis: Equilibria and Kinetics*. Series on Chemical Engineering, ed. R.T. Yang. Vol. 2. 1998: Imperial College Press. 892.

99. Kvamsdal, H.M. and T. Hertzberg, *Optimization of PSA systems,studies on cyclic steady state convergence.* Computers & Chemical Engineering, 1997. **21**(8): p. 819-832.

100. Croft, D.T. and M.D. LeVan, *Periodic states of adsorption cycles,Direct determination and stability.* Chemical Engineering Science, 1994. **49**(11): p. 1821-1829.

101. Smith, O.J. and A.W. Westerberg, *Acceleration of cyclic steady state convergence for pressure swing adsorption models.* Industrial & Engineering Chemistry Research, 1992. **31**(6): p. 1569-1573.

102. Ding, Y. and M.D. LeVan, *Periodic states of adsorption cycles III. Convergence acceleration for direct determination.* Chemical Engineering Science, 2001. **56**(17): p. 5217-5230.

103. Smith, I., J. Oliver, and A.W. Westerberg, *Mixed-integer programming for pressure swing adsorption cycle scheduling.* Chemical Engineering Science, 1990. **45**(9): p. 2833-2842.

104. Jiang, L., L.T. Biegler, and V.G. Fox, *Design and optimization of pressure swing adsorption systems with parallel implementation.* Computers & Chemical Engineering, 2005. **29**(2): p. 393-399.

105. Fiandaca, G., E.S. Fraga, and S. Brandani, *A multi-objective genetic algorithm for the design of pressure swing adsorption.* Engineering Optimization, 2009. **41**(9): p. 833-854.

106. www.matche.com/EquipCost/Vessel.htm. [accessed 07-11-2011].

107. Peters, M.S., K.D. Timmerhaus, and R.E. West, *Plant Design and Economics for Chemical Engineers*. 5 ed. 2003: Mc Graw Hill. 988.

108. Rameshni, M. *Selection Criteria for Claus Tail Gas Treating Processes*. accessed 2014. 31.

109. Ruthvan, D.M., *PRINCIPLES OF ADSORPTION & ADSORPTION PROCESSES*. 1 ed. 1984: Wiley Interscience. 435.

110. AlAmeri, A.O., *GASCO*. 2011.

111. AlAli, M., *ADGAS Das Plant* 2011.

112. AlHashimi, S. and M. Tsapatsis, *Solid Adsorbents for the Selective Removal of Dilute H2S in the Claus Process Tail Gas*, in *R&D OIL & GAS SUB COMMITTEES' ANNUAL WORKSHOP*. 2011.

113. Gupta, A., V. Gaur, and N. Verma, *Breakthrough analysis for adsorption of sulfur-dioxide over zeolites.* Chemical Engineering and Processing: Process Intensification, 2004. **43**(1): p. 9-22.

114. Vieillard, P., *A predictive model for the entropies and heat capacities of zeolites.* European Journal of Mineralogy. **22**(6): p. 823-836.

115. NIST. *http://webbook.nist.gov* [accessed 02-11-2012].

116. Felder, R.M. and R.W. Rousseau, *Elementary Principles of Chemical Processes*. Third Edition ed. 2000: John Wiley & Sons Inc.

117. Ashcraft, B. and J. Swinton, *Oxygen Production with Silver Zeolites.* Capstone Design Project, 2007.

118. *www.worldsteelprices.com* [accessed 02-11-2012].

119. Belmabkhout, Y., G. De Weireld, and A. Sayari, *Amine-Bearing Mesoporous Silica for CO2 and H2S Removal from Natural Gas and Biogas.* Langmuir, 2009. **25**(23): p. 13275-13278.

120. Huang, H.Y., et al., *Amine-Grafted MCM-48 and Silica Xerogel as Superior Sorbents for Acidic Gas Removal from Natural Gas.* Industrial & Engineering Chemistry Research, 2002. **42**(12): p. 2427-2433.

121. Hamon, L., et al., *Comparative Study of Hydrogen Sulfide Adsorption in the MIL-53(Al, Cr, Fe), MIL-47(V), MIL-100(Cr), and MIL-101(Cr) Metal−Organic Frameworks at Room Temperature.* Journal of the American Chemical Society, 2009. **131**(25): p. 8775-8777.

122. Heymans, N., S. Vaesen, and G. De Weireld, *A complete procedure for acidic gas separation by adsorption on MIL-53 (Al).* Microporous and Mesoporous Materials, 2012. **154**(0): p. 93-99.

123. Yang, Q., et al., *Probing the adsorption performance of the hybrid porous MIL-68 (Al): a synergic combination of experimental and modelling tools.* Journal of Materials Chemistry, 2012. **22**(20): p. 10210-10220.

124. Cheah, S., D.L. Carpenter, and K.A. Magrini-Bair, *Review of Mid- to High-Temperature Sulfur Sorbents for Desulfurization of Biomass- and Coal-derived Syngas.* Energy & Fuels, 2009. **23**(11): p. 5291-5307.

125. Xue, M., et al., *Screening of adsorbents for removal of H_2S at room temperature.* Green chemistry, 2003. **5**(5): p. 529-534.

126. Cosoli, P., et al., *Hydrogen sulphide removal from biogas by zeolite adsorption: Part I. GCMC molecular simulations.* Chemical Engineering Journal, 2008. **145**(1): p. 86-92.

127. Cosoli, P., et al., *Hydrogen sulfide removal from biogas by zeolite adsorption. Part II. MD simulations.* Chemical Engineering Journal, 2008. **145**(1): p. 93-99.

128. Karge, H., M. Ziołek, and M. Łaniecki, *Uv/vis and ir spectroscopic study of hydrogen sulphide adsorption on faujasite-type zeolites.* Zeolites, 1987. **7**(3): p. 197-202.

129. Karge, H.G. and J. Raskó, *Hydrogen sulfide adsorption on faujasite-type zeolites with systematically varied Si-Al ratios.* Journal of Colloid and Interface Science, 1978. **64**(3): p. 522-532.

130. Garcia, C.L. and J.A. Lercher, *Adsorption of hydrogen sulfide on ZSM 5 zeolites.* The Journal of Physical Chemistry, 1992. **96**(5): p. 2230-2235.

131. Sung, C.-Y., et al., *Density Functional Theory Study on the Adsorption of H_2S and Other Claus Process Tail Gas Components on Copper-and Silver-Exchanged Y Zeolites.* The Journal of Physical Chemistry C, 2012. **116**(5): p. 3561-3575.

132. Tantet, J., M. Eić, and R. Desai, *Breakthrough study of the adsorption and separation of sulfur dioxide from wet gas using hydrophobic zeolites.* Gas separation & purification, 1995. **9**(3): p. 213-220.

133. Deng, S. and Y. Lin, *Sulfur dioxide sorption properties and thermal stability of hydrophobic zeolites.* Industrial & engineering chemistry research, 1995. **34**(11): p. 4063-4070.

134. Deng, H., et al., *Adsorption equilibrium for sulfur dioxide, nitric oxide, carbon dioxide, nitrogen on 13X and 5A zeolites.* Chemical Engineering Journal, 2012. **188**: p. 77-85.

135. Do, D.D., *Adsorption analysis*. 1998: World Scientific.

136. Shor, A. and A. Rubaylo, *IR spectroscopic study of SO< sub> 2</sub> adsorption on modified Y zeolites.* Journal of molecular structure, 1997. **410**: p. 133-136.

137. Nasluzov, V.A., et al., *Density functional study of SO< sub> 2</sub> adsorption in HY zeolites.* Journal of Molecular Structure: THEOCHEM, 1999. **466**(1): p. 235-244.

138. Teraoka, Y., et al., *Adsorption of sulfur dioxide on Y-type zeolites.* Studies in Surface Science and Catalysis, 1997. **105**: p. 1787-1793.

139. Li, Z. and M. Flytzani-Stephanopoulos, *Cu-Cr-O and Cu-Ce-O Regenerable Oxide Sorbents for Hot Gas Desulfurization.* Industrial & Engineering Chemistry Research, 1997. **36**(1): p. 187-196.

140. Centi, G., et al., *Simultaneous removal of SO_2/NO_x from flue gases. Sorbent/catalyst design and performances.* Chemical Engineering Science, 1990. **45**(8): p. 2679-2686.

141. Tamhankar, S.S., et al., *Mixed-oxide sorbents for high-temperature removal of hydrogen sulfide.* Industrial & Engineering Chemistry Process Design and Development, 1986. **25**(2): p. 429-437.

142. Baird, T., et al., *Modified zinc oxide absorbents for low-temperature gas desulfurisation.* Journal of the Chemical Society, Faraday Transactions, 1992. **88**(22): p. 3375-3382.

143. Polychronopoulou, K., et al., *Novel Fe-Mn-Zn-Ti-O mixed-metal oxides for the low-temperature removal of H_2S from gas streams in the presence of H_2, CO_2, and H_2O.* Journal of Catalysis, 2005. **236**(2): p. 205-220.

144. Sasaoka, E., et al., *Stability of Zinc Oxide High-Temperature Desulfurization Sorbents for Reduction.* Energy & Fuels, 1994. **8**(3): p. 763-769.

145. Westmoreland, P.R. and D.P. Harrison, *Evaluation of candidate solids for high-temperature desulfurization of low-Btu gases.* Environmental Science & Technology, 1976. **10**(7): p. 659-661.

146. Siriwardane, R.V. and J.A. Poston, *Characterization of copper oxides, iron oxides, and zinc copper ferrite desulfurization sorbents by X-ray photoelectron spectroscopy and scanning electron microscopy.* Applied Surface Science, 1993. **68**(1): p. 65-80.

147. Swisher, J. and K. Schwerdtfeger, *Review of metals and binary oxides as sorbents for removing sulfur from coal-derived gases.* Journal of Materials Engineering and Performance, 1992. **1**(3): p. 399-407.

148. Gibson, J.B. and D.P. Harrison, *The Reaction between Hydrogen Sulfide and Spherical Pellets of Zinc Oxide.* Industrial & Engineering Chemistry Process Design and Development, 1980. **19**(2): p. 231-237.

149. Lew, S., A.F. Sarofim, and M. Flytzani-Stephanopoulos, *The reduction of zinc titanate and zinc oxide solids.* Chemical Engineering Science, 1992. **47**(6): p. 1421-1431.

150. Flytzani-Stephanopoulos, M., M. Sakbodin, and Z. Wang, *Regenerative Adsorption and Removal of H_2S from Hot Fuel Gas Streams by Rare Earth Oxides.* Science, 2006. **312**(5779): p. 1508-1510.

151. Hepworth, M.T., R. Ben-Slimane, and S. Zhong, *Thermodynamic comparison of several sorbent systems for hot coal-derived fuel-gas desulfurization.* Energy & Fuels, 1993. **7**(5): p. 602-609.

152. RODRIGUEZ, et al., *Interaction of Sulfur with Well-Defined Metal and Oxide surfaces: Unraveling The Mysteries Behind Catalyst Poisoning and Desulfurization* Vol. 32. 1999, Washington, DC, ETATS-UNIS: American Chemical Society. 10.

153. Rodriguez, J.A., J. Dvorak, and T. Jirsak, *Chemistry of SO_2, H_2S, and CH_3SH on Carbide-Modified Mo(110) and Mo_2C Powders: Photoemission and XANES Studies.* The Journal of Physical Chemistry B, 2000. **104**(48): p. 11515-11521.

154. Rodriguez, J.A., et al., *Importance of O vacancies in the behavior of oxide surfaces: Adsorption of sulfur on $TiO_2(110)$.* Physical Review B, 2002. **65**(23): p. 235414.

155. Pacchioni, G., A. Clotet, and J.M. Ricart, *A theoretical study of the adsorption and reaction of SO_2 at surface and step sites of the MgO (100) surface.* Surface Science, 1994. **315**(3): p. 337-350.

156. Rodriguez, J.A., et al., *Reaction of H_2S and S_2 with Metal/Oxide Surfaces:,Band-Gap Size and Chemical Reactivity.* The Journal of Physical Chemistry B, 1998. **102**(28): p. 5511-5519.

157. Rodriguez, J.A., et al., *Studies on the Behavior of Mixed-Metal Oxides and Desulfurization:, Reaction of H_2S and SO_2 with Cr_2O_3 (0001), MgO (100), and $Cr_xMg_{1-x}O$ (100).* Journal of the American Chemical Society, 2000. **122**(49): p. 12362-12370.

158. Rodriguez, J.A. and A. Maiti, *Adsorption and Decomposition of H_2S on MgO (100), NiMgO (100), and ZnO (0001) Surfaces:,A First-Principles Density Functional Study.* The Journal of Physical Chemistry B, 2000. **104**(15): p. 3630-3638.

159. Sasmaz, E. and J. Wilcox, *Mercury Species and SO_2 Adsorption on CaO(100).* The Journal of Physical Chemistry C, 2008. **112**(42): p. 16484-16490.

160. Rodriguez, J.A., et al., *Interaction of SO_2 with MgO (100) and Cu/MgO (100): Decomposition Reactions and the Formation of SO_3 and SO_4.* The Journal of Physical Chemistry B, 2000. **104**(31): p. 7439-7448.

161. Casarin, M., et al., *SO_2 on TiO_2 (110) and Ti_2O_3 (1012) Nonpolar Surfaces:,A DFT Study.* The Journal of Physical Chemistry B, 2005. **109**(25): p. 12596-12602.

162. Westmoreland, P.R., J.B. Gibson, and D.P. Harrison, *Comparative kinetics of high-temperature reaction between hydrogen sulfide and selected metal oxides.* Environmental Science & Technology, 1977. **11**(5): p. 488-491.

163. Centi, G., et al., *Combined $DeSO_x/DeNO_x$ reactions on a copper on alumina sorbent-catalyst. 2. Kinetics of the $DeSO_x$ reaction.* Industrial & Engineering Chemistry Research, 1992. **31**(8): p. 1956-1963.

164. Centi, G., et al., *Combined $DeSO_x/DeNO_x$ reactions on a copper on alumina sorbent-catalyst. 1. Mechanism of sulfur dioxide oxidation-adsorption.* Industrial & Engineering Chemistry Research, 1992. **31**(8): p. 1947-1955.

165. Jun, H.K., et al., *A Study of Zn-Ti-Based H_2S Removal Sorbents Promoted with Cobalt Oxides.* Industrial & Engineering Chemistry Research, 2001. **40**(16): p. 3547-3556.

166. Park, N.-K., T.J. Lee, and S.O. Ryu, *Study on Deactivation of Zinc-Based Sorbents for Hot Gas Desulfurization.* Industrial & Engineering Chemistry Research, 2010. **49**(10): p. 4694-4699.

167. Ryu, S.O., et al., *Multicyclic Study on Improved Zn/Ti-Based Desulfurization Sorbents in Mid-Temperature Conditions.* Industrial & Engineering Chemistry Research, 2004. **43**(6): p. 1466-1471.

168. Carnes, C.L. and K.J. Klabunde, *Unique Chemical Reactivities of Nanocrystalline Metal Oxides toward Hydrogen Sulfide.* Chemistry of Materials, 2002. **14**(4): p. 1806-1811.

169. Du, G. and G. Van Tendeloo, *Cu (OH)< sub> 2</sub> nanowires, CuO nanowires and CuO nanobelts.* Chemical Physics Letters, 2004. **393**(1): p. 64-69.

170. Heckl, O., F. Haider, and J. Gegner, *EELS analysis of internal metal–oxide interfaces.* International Journal of Materials Research, 2008. **99**(5): p. 496-501.

171. Su, F., C. Lu, and H.-S. Chen, *Adsorption, Desorption, and Thermodynamic Studies of CO_2 with High-Amine-Loaded Multiwalled Carbon Nanotubes.* Langmuir, 2011. **27**(13): p. 8090-8098.

172. Yun-Yang, H., *Selective adsorption of carbon monoxide and complex formation of cuprous-ammines in Cu(I)Y zeolites.* Journal of Catalysis, 1973. **30**(2): p. 187-194.

173. Froment, G.F., K.B. Bischoff, and J. De Wilde, *Chemical reactor analysis and design*. Vol. 2. 1990: Wiley New York.

174. Szekely, J. and J. Evans, *Studies in gas-solid reactions: Part I. A structural model for the reaction of porous oxides with a reducing gas.* Metallurgical Transactions, 1971. **2**(6): p. 1691-1698.

175. Yaşyerli, S., et al., *Removal of hydrogen sulfide by clinoptilolite in a fixed bed adsorber*. Chemical Engineering and Processing: Process Intensification, 2002. **41**(9): p. 785-792.